Real-Time Dosimetry for Prostate Brachytherapy Using TRUS and Fluoroscopy

Candidate: Danny G. French

Supervisor: Dr. S.E. Salcudean

A THESIS SUBMITTED IN PARTIAL FULFILLMENT OF
THE REQUIREMENTS FOR THE DEGREE OF
MASTER OF APPLIED SCIENCE

in

THE FACULTY OF GRADUATE STUDIES

Electrical and Computer Engineering

THE UNIVERSITY OF BRITISH COLUMBIA

December 2004

Abstract

A means of achieving real-time dosimetry for prostate brachytherapy using transrectal ultrasound (TRUS) and fluoroscopy has been developed. The approach is designed to fit into the current protocol used at the Vancouver Cancer Center (VCC) for prostate brachytherapy.

The TRUS and fluoroscopic images are fused using a single fluoroscopic image of the TRUS probe. The tip of each needle, used to implant the seeds, is identified in TRUS images. Using the needle tip location and the known entry point of the needle in the needle guide, a needle path is interpolated. The coronal plane coordinates of the seeds are determined from fluoroscopic images acquired at a fixed angle. The remaining coordinates of the seeds are determined from interpolated needle paths. Intraoperative seed motion is tracked using fluoroscopic images and TRUS. The dose distribution is computed and displayed in the TRUS image frame after each fluoroscopic image is acquired.

Our approach is validated on a phantom and compared to the seed distributions found in computed tomography (CT) images acquired three to four hours after the procedure.

Contents

List of Tables

List of Figures

Acknowledgements

I would like to thank my supervisor Dr. Tim Salcudean for his guidance and continuous support. I am very grateful for his extensive knowledge and excellent feedback throughout my thesis.

My project would not have been possible without the clinical collaboration provided by the people at the Vancouver Cancer Center (VCC). I would like to thank Dr. James Morris and Dr. Mira Keyes for their knowledge and feedback throughout my project. I thank Dr. Jonn Wu, Dr. Tom Pickles, Dr. Michael MacKenzie and Alexander Agranovich for their patience while I collected data in the operating room.

I am very appreciative of the efforts of the radiation therapists at the VCC, Alex Kurk, Suzie Gagnon and Petre Persch. They helped me collect data and coordinate experiments and answered my many questions.

I would like to thank Dr. Ingrid Spadinger for helping me understand the basic physics of prostate brachytherapy, and Bob Harrison for processing the post-operative CT data and showing me how to Variseed.

I thank all my labmates in the Robotics and Control Lab. Orcun Goksel helped extensively with collecting clinical data, including many visits to the operating room. Daniela Constantinescu discussed many mathematically questions with me. Julian Guerrero helped me understand the principles of ultrasound. Simon DiMaio provided updates on prostate brachytherapy. Simon Bachman for designed the phantoms used in my thesis. And, Xu Wen helped with the needle tip experiments.

I could not have completed my thesis without the continuous support from my family through emails and long distance phone calls.

And finally, I would like to thank Julia Brydon for her friendship and loving support through the emotional highs and lows of thesis work.

Chapter 1

Introduction

Prostate cancer is the abnormal growth and variable cellular differentiation of prostate tissue. In 2004, 20,100 new cases of prostate cancer are expected to be reported in Canada [41]. One treatment option is to expose the cancerous cells to ionizing radiation. This radiation causes a rapid break down in the cell's deoxyribonucleic acid (DNA) structures resulting in cell death. The prostate can be exposed to ionizing radiation either through external beams, referred to as external beam radiation therapy, or by implanting radioactive seeds into the prostate, referred to as brachytherapy.

Brachytherapy allows the radiation to be localized ensuring the cancerous cells are destroyed while minimizing damage to healthy tissue. Although the procedure varies between institutions, prostate brachytherapy involves the permanent implantation of between 80 and 150 small radioactive seeds into the prostate. The process begins several weeks prior to the actual implantation of the seeds, with a preoperative procedure where the prostate is imaged using transrectal ultrasound (TRUS). These TRUS images are used to define the prostate volume and plan the seed distributions required to kill all the cancerous cells. Several weeks after the preoperative visit, the patient is taken to an operating room to implant the seeds. Once the patient is anesthetized, the seeds are implanted using needles inserted through the perineum by a radiation oncologist. Throughout the procedure, TRUS is used to image the prostate and guide the needles, while fluoroscopy is used to image the seeds.

At the Vancouver Cancer Center (VCC) over 1000 cases of prostate cancer have been treated with brachytherapy. A more specific description of the protocol used at the VCC for prostate

brachytherapy is given in the next section.

1.1 The Protocol for Prostate Brachytherapy Practiced at the VCC

A flow chart summarizing the protocol used for prostate brachytherapy at the VCC is shown in Figure 1.1. Preparation for the procedure begins three to four weeks prior to the implantation of the seeds with a preoperative volume study of the patient's prostate. The preoperative volume study consists of imaging the entire prostate with nine to fourteen TRUS images at 5 mm spacing. To acquire these images, the TRUS probe is first mounted to the bed as shown in Figure 1.2. The probe is locked in a stepper, which constraints the probe to move in 5 mm increments along its longitudinal axis. The stepper is attached to a stage which allows the position and orientation of the stepper to be finely adjusted and locked. The stage is rigidly attached to the bed, which supports the patient, by two stabilizing links, which allow for coarse positioning of the stage.

The preoperative volume study is used to define the prostate volume and plan the seed distribution. A medical physicist designs the seed distribution based on the prostate volume to destroy all of the prostate tissue, while minimizing radiation exposure to surrounding healthy tissue. The planning software restricts the position of the seeds to lie on a 3D grid with 5 mm spacing. This planned seed distribution is referred to as the preoperative plan.

The intraoperative procedure begins with the radiation oncologist registering the preoperative TRUS images and the intraoperative TRUS images. The TRUS probe is mounted on the same set-up used for the volume study and the intraoperative TRUS images are manually aligned with the TRUS images from the volume study. This aligns the prostate volume determined from the preoperative images to the intraoperative prostate volume, thus allowing the preoperative plan to be registered to the intraoperative prostate volume.

Figure 1.3 is a diagram of the intraoperative set-up used to insert the needles. A needle guide (see Figure 1.3b) is mounted on the stepper shown in Figure 1.2. This needle guide is a metal plate with holes arranged on a 5 mm grid, which correspond to the transverse plane of the 3D grid used to plan the seed distribution. This needle guide is secured at a fixed distance from the longitudinal axis of the probe.

The third dimension of the 3D planning grid is implemented by the spacing of the seeds in each needle. There are two types of seeds used at the VCC, both of which are preloaded into the needles

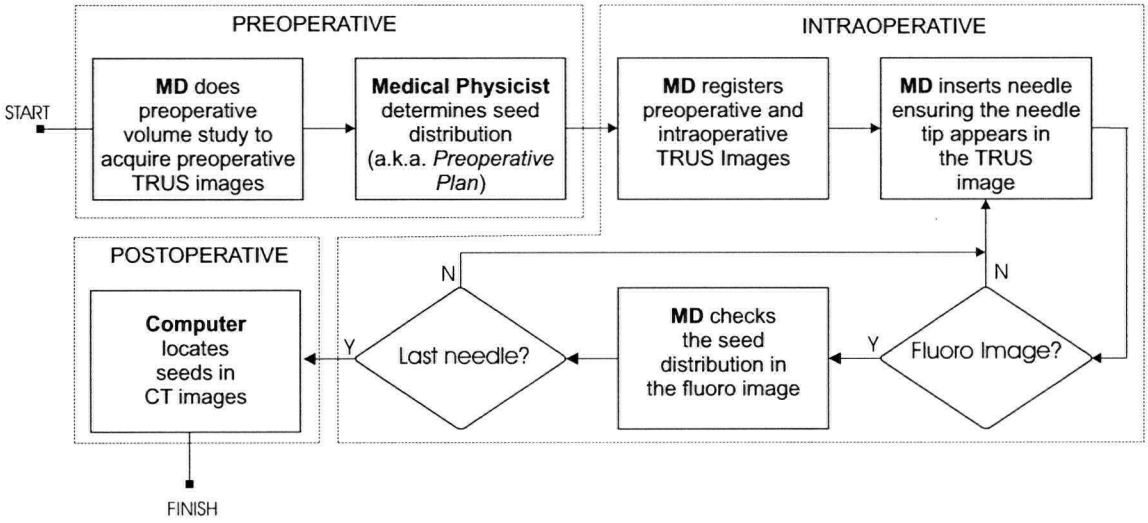

Figure 1.1: A flow chart of the procedure for prostate brachytherapy at the VCC.

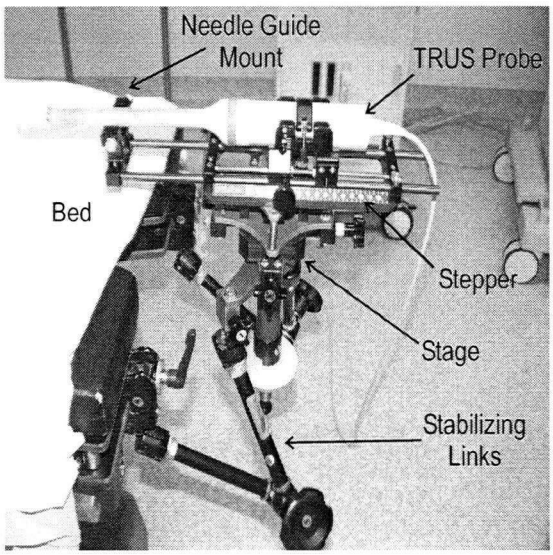

Figure 1.2: The setup used to hold the TRUS probe during the volume study and seed implant procedure.

prior to the procedure. At the VCC, the most commonly used seeds are referred to as *RAPID Strand*. RAPID Strand seeds are encased in a mesh, which prevents the seeds from jamming in the needle and ensures that they remain at a 5 mm spacing once implanted. At the VCC, RAPID Strand seeds are used when the preoperative plan requires 5 mm spacing. Occasionally, the plan will require seed spacing which is a multiple for 5 mm, such as 30 mm spacing. In these cases *loose seeds* are implanted. These seeds are individually loaded, with plastic spacers between seeds to ensure the correct spacing. These seeds tend to jam in the needle and move once implanted, therefore they are used much less frequently than RAPID Strand seeds.

Referring back to Figure 1.3, the TRUS probe is used to acquire 2D transverse images of the prostate and guide the needles as they are inserted. Figure 1.3a shows a sample TRUS image. Note that there is a grid overlaid on this image which corresponds to the grid of the needle guide. Each needle is inserted using the needle guide, force feedback from the needle, and visual feedback from the TRUS, until the needle tip artifact appears as a high intensity flash near the grid point indicated in the preoperative plan. A total of 20 to 30 needles are inserted in this manner, starting with the needles in the uppermost row of the needle guide, working down row-by-row.

Ideally, the stage is not adjusted throughout the procedure. However, intraoperative prostate shifting and deformation result from patient motion, forces from needle insertions, and intraoperative edema. To compensate for this motion, fine adjustments of the stage are occasionally done to realign the intraoperative TRUS images and TRUS images from the volume study.

Throughout the procedure coronal plane fluoroscopic images of the patient are acquired as requested by the radiation oncologist. These images show a 2D projection of the seed distribution (Figure 1.3c shows an example) to help the radiation oncologist visualize the seed distribution.

After the seeds prescribed by the preoperative plan have been implanted, the radiation oncologist has the option to implant five more loose seeds into any regions of the prostate judged to be under-dosed. The fluoroscopic image of the seed distribution, combined with TRUS and notes made throughout the procedure are used to judge potentially under-dosed regions of the prostate.

At the VCC, the postoperative procedure usually occurs thirty days after the implant. A computed tomography (CT) images of the patient is acquired to locate the implanted seeds. The radiation delivered to the tissues, referred to as *dosimetry*, is computed based on the seed distribution to ensure all the prostate tissue is destroyed.

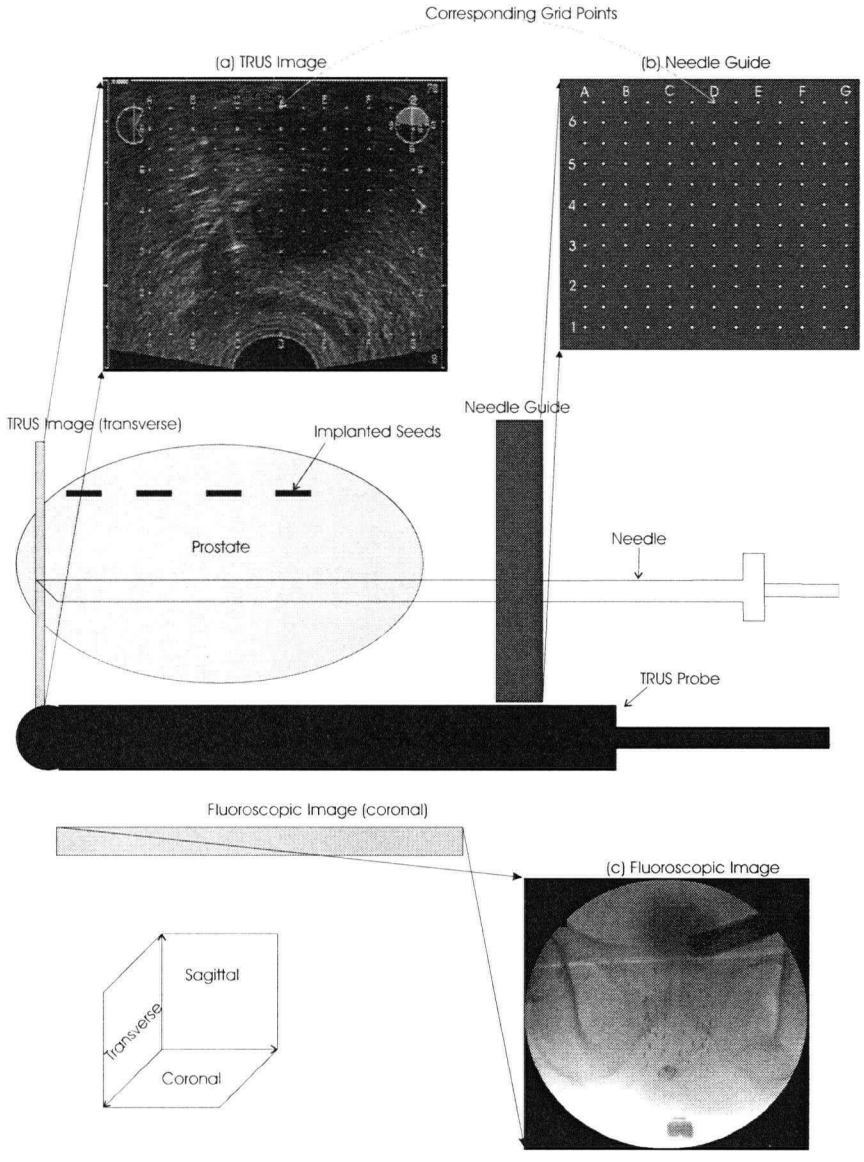

Figure 1.3: A diagram of the setup used to implant the seeds. (a) An example of a TRUS image (the needle tip artifact is shown at C3), (b) the needle guide, and (c) an example of fluoroscopic image of the seeds.

1.2 Thesis Motivation

Because of inaccuracies in needle placement, intraoperative seed motion, and intraoperative prostate shifting and deformation there is a need to provide accurate real-time dosimetric feedback to the radiation oncologist. This feedback will allow radiation oncologists to do interactive planning,

which is defined as intraoperatively modifying the preoperative plan to reflect the actual location of implanted seeds. Interactive planning ensures the prostate receives sufficient radiation to destroy cancerous cells [38] [42].

The potential for improved dose distribution through interactive planning has been expressed by the radiation oncologists at the VCC and is also strongly supported in [38], [42] and [44]. As indicated in [38] and demonstrated by the systems presented in the Literature Review (see Section 1.4), a means of achieving interactive planning has not been fully realized.

1.3 Thesis Objectives

The objective of this thesis is to develop a system to intraoperatively compute the location of seeds implanted for prostate brachytherapy at the VCC. The dosimetry resulting from the implanted seeds must be computed with respect to the intraoperative prostate volume and displayed to the radiation oncologist. To effectively meet the needs of the radiation oncologists at the VCC there are several constraints on the system:

- Only minimal changes can be made to the protocol for prostate brachytherapy currently practiced at the VCC (see Figure 1.1).
- Only the imaging equipment (TRUS and fluoroscopy) currently available at the VCC for prostate brachytherapy can be used.
- Dosimetric feedback must be provided throughout the procedure, as opposed to only at the end of the procedure. This will provide reassurance to the radiation oncologist and allow for more extensive corrections to the preoperative plan to reflect the actual location of the implanted seeds.
- Dosimetry must be displayed in a manner such that the radiation oncologist can easily do interactive planning.
- Intraoperative seed motion must be tracked to accurately compute dosimetry.

1.4 Literature Review of RTD for Prostate Brachytherapy

The need for real-time dosimetry (RTD) for prostate brachytherapy has resulted in several commercial systems which attempt to use TRUS to get the 3D coordinates of the implanted seeds. Early research used fluoroscopy to compute post-operative dosimetry offline. This work helped developed more advanced systems which fuse TRUS and fluoroscopic images. Currently, there is one institute that uses intraoperative magnetic resonance (MR) imaging to computed RTD. There have also been several attempts to localize the seeds in TRUS.

In this section an overview of RTD systems for prostate brachytherapy is presented. Since the components of our approach are solved in the following chapters, the some of the contributions of these RTD systems are left to be discussed in greater detail as each component is solved.

1.4.1 Commercial Systems

The VariSeed system (Varian Medical Systems, Palo Alto, CA) uses TRUS to identify the tip of each needle and assumes the needle's path is a straight. For a given needle all the seeds have the same coordinate in the transverse plan and the remaining coordinate of each seed is determined by assuming the seeds lie at their preplanned spacing [38]. This system does not account for intraoperative seed motion.

The Prostate Implant Planning Engine for Radiotherapy (PIPER) system (RTek, Pittsford, NY) uses live TRUS to identify needle tracks. A needle path is determined from the location of the needle tracks and the seed positions are assumed to lie at their preplanned spacing. [38] Using the estimated seed locations and manually identifying the contour of the prostate the system can adjust the preplan to prevent underdosing regions in the prostate and overdosing other healthily anatomy [34].

The Interplant System (CMS, Inc, Champaign, IL) uses an optical encoder to find the depth of the probe in the prostate volume and to register the probe to the needle guide. The dosimetry is calculated based on TRUS probe position, the location of needle tracks and assumed seed spacing [38] [28].

The Sonographic Planning of Oncology Treatment (SPOT) (Nucletron Corporation, Veenandaal, Netherlands) uses 3D US to locate needles and seeds as they are implanted. However, manual intervention is required to localize many of the seeds and needles. The resulting dosimetry is dis-

played with respect to the prostate volume [38] [13].

The Strata System (Rosses Medical Systems, Columbia, MD) uses TRUS and sagittal ultrasound (US) images to track the needle position. Once the needle position is known the seeds are assumed to be implanted at the preplanned seed spacing [38].

All of these commercial systems use ultrasound to locate needles or needle tracks (also known as blood trails) and assume the seeds lie at the preplanned seed spacing to compute dosimetry. Individual seeds are not located because seeds cannot be reliably located using B-mode ultrasound images [24]. Therefore, another modality must be used or combined with TRUS to accurately compute dosimetry. Furthermore, these systems cannot account for irregular seed spacing or intra-operative seed motion [8].

1.4.2 Research Systems

1.4.2.1 Fluoroscopy

In the early 1980's several techniques for computing the 3D coordinates of implanted seeds were developed to compute post-operative dosimetry. Although these systems are not real-time and in most cases do not report dosimetry with respect to the prostate volume, components of these systems are useful in developing more advanced RTD systems.

A three-film technique using two stereo and one anterior-posterior film is reported in [2] to localize seeds in 3D. Another three-film technique is presented in [45] which uses films obtained from a gantry rotation rather than a stereo shift. A similar method is presented in [5]. In [1] fiducial markers are used to match seeds in three non-coplanar projections and to account for patient motion. A two-film technique reported in [47] uses the endpoints of seeds to match the seeds in separate images rather than just the centroids of the seeds.

More recently, in [57] and [56] a simulated annealing algorithm is used to automatically match seed artifacts in three radiographic films or fluoroscopic images. The matched seed artifacts are back-projected to compute the 3D coordinate of each seed. In these works, no attempt is made to register the seed distribution to the prostate volume. However, in a later work presented in [4], the same authors fuse fluoroscopic and TRUS images using three gold markers to determine post-operative dosimetry with respect to the prostate.

In [39] a fast cross-projection algorithm is presented to reconstruct the seed distribution using

three fluoroscopic images, but the seed distribution is not registered to the prostate volume. The same authors present another method to compute the seed distribution from three x-ray projections in [40]. This work attempts to overcome the problems of identifying and matching clustered and overlapping seed artifacts using an algorithm based on epipolar imaging geometry and pseudo-matching of undetected seeds.

In [49] a statistical classifier algorithm is used to locate seeds from three fluoroscopic images. A three-film system for determining post-operative dosimetry is presented in [6] which uses multiscale geometric statistical pattern recognition (MGTPR) to identify the seeds in two film images. The seeds are labelled and back-projected to determine the 3D coordinates of each seed. A third film is used to verify the results.

All of these methods require seed artifacts in multiple images be matched. Matching the seed can be difficult because of seed clustering and image noise. To avoid matching every seed [32] defines a unique trajectory for each seeds using a Hough transform such that the trajectory can be known from multiple perspectives.

Although these systems were intended for post-operative dosimetry, rather than RTD, they do use fluoroscopy to accurately reconstruct the seed distribution. These works have led to more advanced RTD systems.

1.4.2.2 Fluoroscopic and TRUS Imaging

Fluoroscopy is commonly used, in addition to TRUS, for prostate brachytherapy because the seeds are clearly visible. As a result, several methods of fusing TRUS and fluoroscopic images to compute dosimetry have been reported.

In [23] TRUS and three fluoroscopic images are fused using four needle tips. The 3D coordinate of each needle tip is determined from the TRUS probe position and the location of the needle tip artifact in the TRUS image. This information is combined with the coordinates of the needle tip artifact in the three fluoroscopic images to register the fluoroscopic and TRUS images. TRUS is used to identify the prostate contour and fluoroscopic images taken from three or more perspectives are used to locate individual seeds and compute dosimetry.

A similar three-film approach is presented in [50]. This work focuses on registering the TRUS and fluoroscopic images using several of the implant seeds. This work reports that approximately 40 percent of the implanted seeds are visible in TRUS. The visible seeds are matched between the

two imaging modalities and a rigid transformation is defined. The seed distribution is constructed from multiple fluoroscopic images and the dosimetry displayed with respect to the prostate.

In [53] and [52] fluoroscopic images are registered to the TRUS image using five to seven noncoplanar reference points (i.e. lead fiducial markers) attached to the TRUS probe. The TRUS is used to identify the contour of the prostate. After each set of three or more fluoroscopic images the dosimetry plan is updated based on the location of the seeds with respect to the prostate and other anatomical structures (which are identified in the TRUS image manually). In these works the gantry angle of the C-arm must be measured with an accuracy better than 1 degree. In [62] a method of automatically determining the gantry angle using known geometry of the fiducial markers is presented.

Work is also being done at John Hopkins to compute real-time dosimetry using a multi-film approach. The TRUS and fluoroscopic images are registered using a sheath with embedded fiducial markers [30]. This sheath remains in the rectum at a fixed location throughout the procedure. A new approach for delineating and matching the seeds will be presented in [29].

These approaches use three or more fluoroscopic images to determine the seed distribution which avoids tracking intraoperative seed motion. And, by registering the TRUS and fluoroscopic images they are able to use advantages from both modalities. The seeds can clearly be delineated in fluoroscopic images, but poor soft tissue contrast makes it very difficult to delineate the prostate. TRUS cannot reliably image the seeds, but has superior soft tissue contrast so the prostate can be clearly delineated. Yet, interactive planning is limited because the C-arm must be rotated to three unique perspectives to update dosimetry, which is time-consuming, inconsistent with the current procedure used at the VCC, and susceptible to error if the patient moves while the C-arm is being rotated.

1.4.2.3 Intraoperative Magnetic Resonance Imaging

Intraoperative MR imaging has been used at the Brigham and Women's Hospital to intraoperatively calculate dosimetry for prostate brachytherapy [11], [12], [31], [14]. In this system the prostate and other significant anatomical structures are delineated manually. The needle artifact is tracked in the image and the seeds are assumed to lie at preplanned spacing along a linear needle path.

MR imaging offers superior soft-tissue contrast so radiation dose to the rectum, urethra, semi-vessel and bladder can be minimized, while maximizing dose to the prostate. In some cases, it is

possible to identify cancerous cells in MR images so it may be possible to target only a small region of the prostate which has these cells.

However, this approach requires a split-ring MR imaging machine and special MR compliant equipment making this approach too expensive for most institutions. Since the seeds do not generate a clear MR signal, it is not likely this system can be advanced from locating the needle to accurately locating the seeds [12].

1.4.2.4 Ultrasound

Because it would be ideal to image both the prostate and localize the seeds with TRUS, there are several attempts to make the seeds appear as clear artifacts in TRUS.

Trans-urethral ultrasound (TUUS) is introduced in [25], as an alternative to TRUS, to image the prostate and identify the seed artifacts. Because TUUS can image the prostate from the center of the gland, as opposed to TRUS which images the prostate from the far posterior boundary, a smaller field of view is required. This allows for increased resolution and minimizes the effects of seed artifacts shadowing each other, as observed in TRUS. In [25] a semi-automatic technique to segment the prostate boundary and seeds is presented. In one patient 82 percent of the seeds are identified and in a second patient 63 percent of seeds. This work is extended in [26] to include automatic seed delineation using a prior information of the seed locations and fuzzy inference rules. Eighty percent of the seeds are correctly identified. This approach has potential, but may be limited by the noise inherit in ultrasound and seeds shadowing each other.

In [33] a radioactive seed is modified to be ferromagnetic. Once implanted, the seed is vibrated using an external magnetic field and imaged using Power Doppler. This approach was tested on one seed in a phantom with some success. However, interference from multiple seeds is cited as a possible limiting factor for this approach.

In [36] and [35] two brass seeds of different lengths are implanted in a phantom and imaged by detecting the resonance frequencies using vibro-acoustography. Two slightly shifted ultrasound beams are focused on each seed which causes an oscillating force. Because the seeds are inhomogeneities inside the medium, a variation in the acoustic emission field is observed and is used to localized the seeds. This approach is still under development and it is unclear if it can be used for a large seed distribution.

A study reported in [46] suggests elastography may be a possible method of imaging brachyther-

apy seeds, but successful results are not reported.

Lastly, a new seed design is presented in [54]. Here, the casing housing the radioactive material is redesigned to better reflect ultrasound waves using a simulation model. Therefore, the seed artifacts should appear as a clear artifact in TRUS. This design is tested in simulation and in a canine prostate with promising results, however further studies are required to validate this approach.

1.4.3 Summary of Literature

Commercial systems, which use needle position to estimate the 3D location of seeds, most readily fit into the protocol for prostate brachytherapy. However, dosimetry can be more accurately determined from the actual seed locations. Fluoroscopy can be used to accurately reconstruct the seed distribution, but the seed distribution must be known with respect to the prostate to facilitate interactive planning. Yet, the two RTD approaches which fuse TRUS and fluoroscope to get the seed distribution with respect to the TRUS image require the C-arm to be rotated to three unique perspectives. This is both time-consuming and inconsistent with the current procedure at the VCC. Although intraoperative MR imaging is currently used, the expense of specialized equipment make such an approach infeasible for most institutions. And, attempts to use TRUS and TUUS to localize the seeds is still in the early stages of development.

Improvements in RTD are most easily achieved by accurately identifying seeds using fluoroscopy and using another modality, such as TRUS, to register the seed distribution with the prostate. Both the seed localization and registration steps must be done with minimal change to the protocol for prostate brachytherapy.

1.5 Approach

At the VCC, the procedure for prostate brachytherapy begins with a volume study of the prostate using TRUS. This volume study is used to plan the seed distribution required to destroy cancerous cells in the prostate. Once in the operating room, the intraoperative TRUS images are manually registered to the volume study TRUS images. To implement the preoperative plan, each needle, preloaded with seeds, is implanted using a needle guide until the needle tip appears as a high intensity artifact at the desired location in the TRUS. Fluoroscopic images of the patient's coronal plane are acquired, as needed, to check the implanted seed distribution matches the preoperative

plan. In summary, the expected location of the seeds and the entry point of each needle in the needle guide are known from the preoperative plan, the actual location of the tip is observed in TRUS and a 2D projection of the implanted seeds is shown in fluoroscopic images.

In accordance with the procedure practiced at the VCC, this thesis presents a new approach to achieve RTD in prostate brachytherapy. Figure 1.4 shows how this approach for RTD integrates into the current procedure for prostate brachytherapy at the VCC given in Figure 1.1. The coordinate systems are described in Figure 1.5. The system calibration requires the radiation oncologist to manually register the intraoperative TRUS to the volume study TRUS images (this step is already part of the current protocol for the procedure). The fluoroscopic and TRUS images are registered using a single fluoroscopic image of the TRUS probe. For each needle TRUS is used to locate the needle tip. Throughout the procedure, fluoroscopic images are used to determine (x,z)-coordinates of the seeds. Using these coordinates and an interpolated needle path from the needle tip to the entry point of the needle in the needle guide (known from the preoperative plan) the y-coordinates of the seeds can be determined and updated. Because the seeds move as the prostate shifts and swells, intraoperative seed motion in the vertical direction is tracked using TRUS. From the 3D coordinates of the seeds the dose distribution can be determined and displayed to the radiation oncologist. The radiation oncologist can also manually verify and adjust the needle tip and seed positions found by the system.

This approach integrates into the current procedure with minimal change and without additional imaging equipment. After each fluoroscopic image is acquired, the radiation oncologist will be able to interactive planning.

1.6 Thesis Overview

Figure 1.6 is a high-level overview of the technical components of the RTD approach proposed in this thesis. Each block is explained in Chapters Two through Five, by further defining the problem, surveying prior work, explaining the methods using a flow chart and text, and discussing test results.

Chapter 2, Calibrating the System: The calibration of the system is presented including the manual registration of the intraoperative TRUS images and volume study TRUS images, a method of removing image distortion in the fluoroscopic images, and the registration of the TRUS and

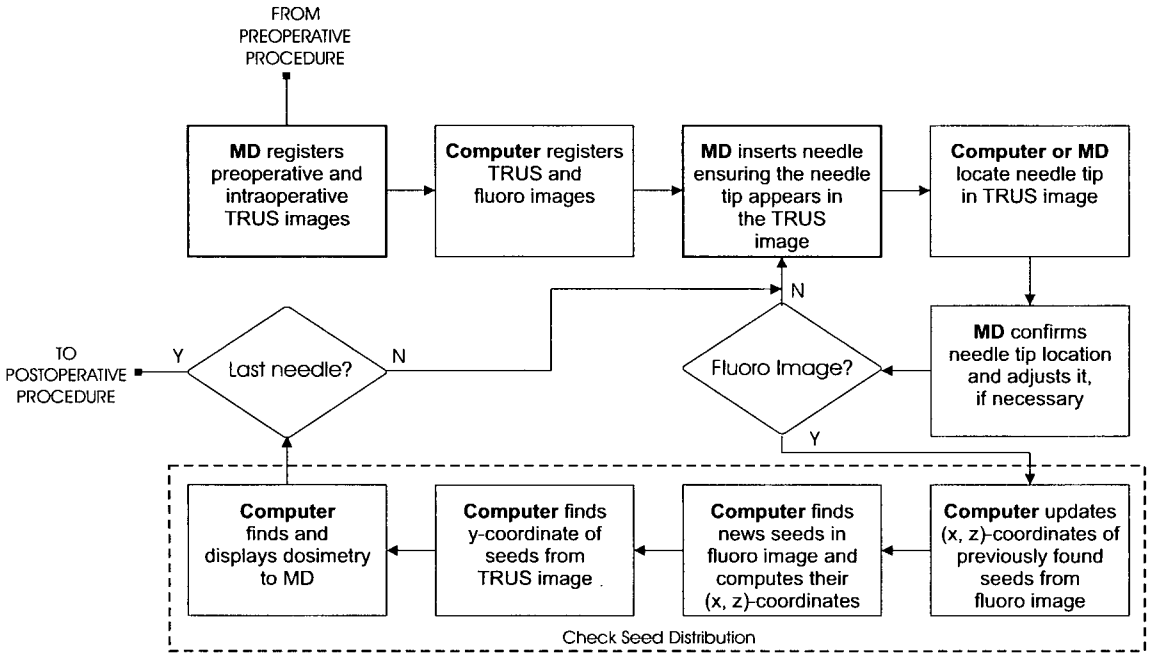

Figure 1.4: A flow chart to show how our RTD system integrates into the current procedure used at the VCC for prostate brachytherapy (shown in Figure 1.1).

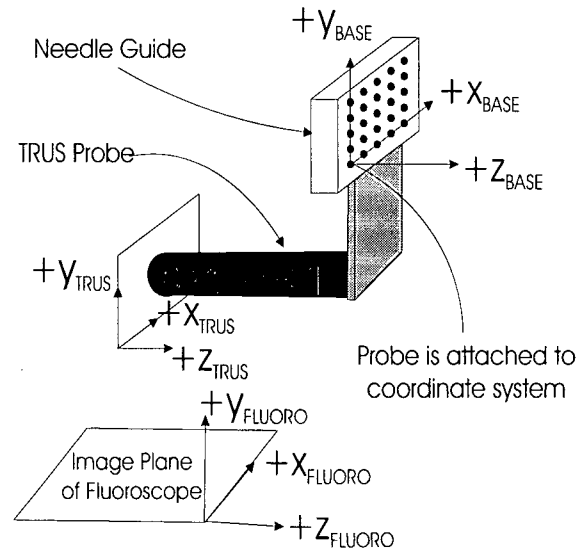

Figure 1.5: The coordinate systems used in our approach.

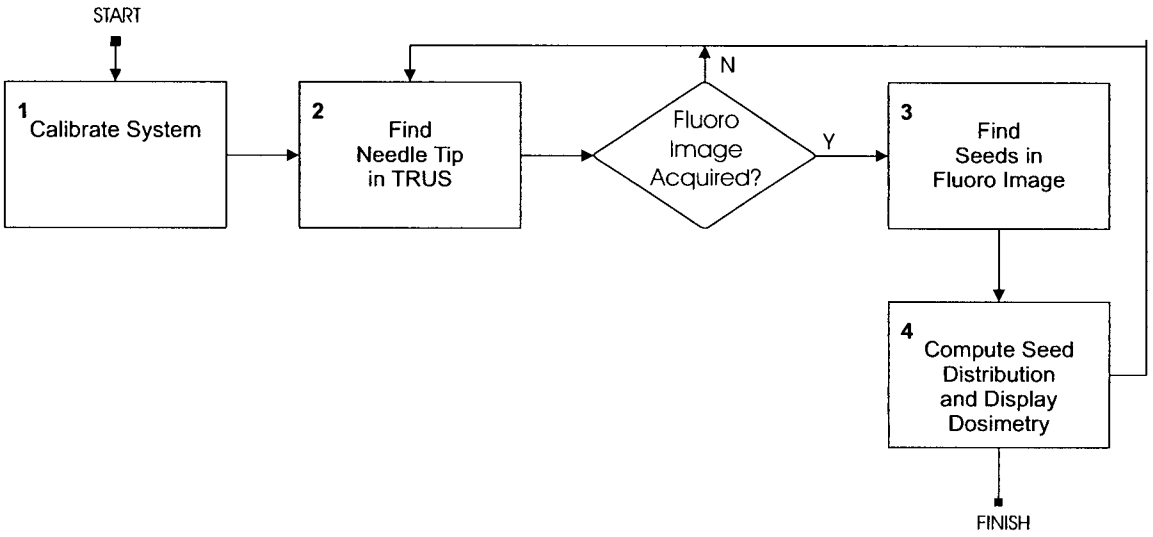

Figure 1.6: A high-level flow chart of the technical components of our approach for computing RTD

fluoroscopic images.

Chapter 3, Finding the Needle Tip Artifact in TRUS: A new method for identifying and localizing the needle tip artifact in TRUS video data is presented.

Chapter 4, Finding Seeds in Fluoroscopic Images: Throughout the procedure fluoroscopic images of the frontal plane of the patient are acquired using a C-arm fluoroscope. Knowing the expected location of the seeds, a method for identifying the seeds deposited by a given needle is presented. The localized seeds are back-projected to the TRUS frame to reconstruct the seed distribution. The same method is used to track the seed motion between fluoroscopic images.

Chapter 5, Computing Seed Distribution and Displaying Dosimetry: The y-coordinate for each seed is found by interpolating a path from the needle tip to the entry point of the needle in the needle guide. An approach for tracking seed motion in the vertical direction is presented. The method of calculating and displaying dosimetry is also presented.

Chapter 6, Results: Our approach is proven using a phantom. Dosimetry determined from Day-0 CT images acquired three to four hours after the implant is compared with dosimetry determined using our RTD system.

Chapter 7, Conclusions and Future Work: Research results, contributions and further work are summarized in this final chapter.

Chapter 2

Calibrating the System

The purpose of calibration is to determine the parameters which define the transformation of a point in one coordinate system (i.e. an image) to another coordinate system. For our system, the intraoperative TRUS images must be matched to the preoperative TRUS images so the seeds can be implanted according to the preoperative plan. Furthermore, the seeds found in the fluoroscopic image must be projected to the TRUS image frame. Then, the needle tips and seeds must be transformed to a fixed base frame. Figure 1.5 shows the origin of these three coordinate systems.

The calibration procedure has three components: manually positioning the TRUS probe so the intraoperative images are very similar to the preoperative TRUS images (effectively registering the intraoperative TRUS to the preplanned seed distribution), removing distortion in the fluoroscopic image and registering the fluoroscopic and TRUS images to the needle guide. Together these steps define a transformation from both the TRUS and fluoroscopic images to a base frame.

2.1 Methods

Figure 2.1 describes the calibration procedure for our RTD system. The radiation oncologist first registers the preoperative TRUS images from the volume study with the intraoperative TRUS images. With the TRUS probe imaging the base[1] plane of the prostate, a fluoroscopic image is acquired. The edge points of the probe in the fluoroscopic image are found using an intensity-based edge detector. The coordinates of the edge points are dewarped and a least squares fit applied to find several corners of the probe artifact. The TRUS and fluoroscopic images are registered using

[1]The base of the prostate is the most superior transverse slice of the prostate.

a single fluoroscopic image of the TRUS probe, the mechanical dimensions of the C-arm and the measured dimensions of the TRUS probe. Then, keeping with the current protocol for prostate brachytherapy, a needle is inserted to the base of the prostate to register the needle guide (i.e. the base frame of our system) to the prostate volume.

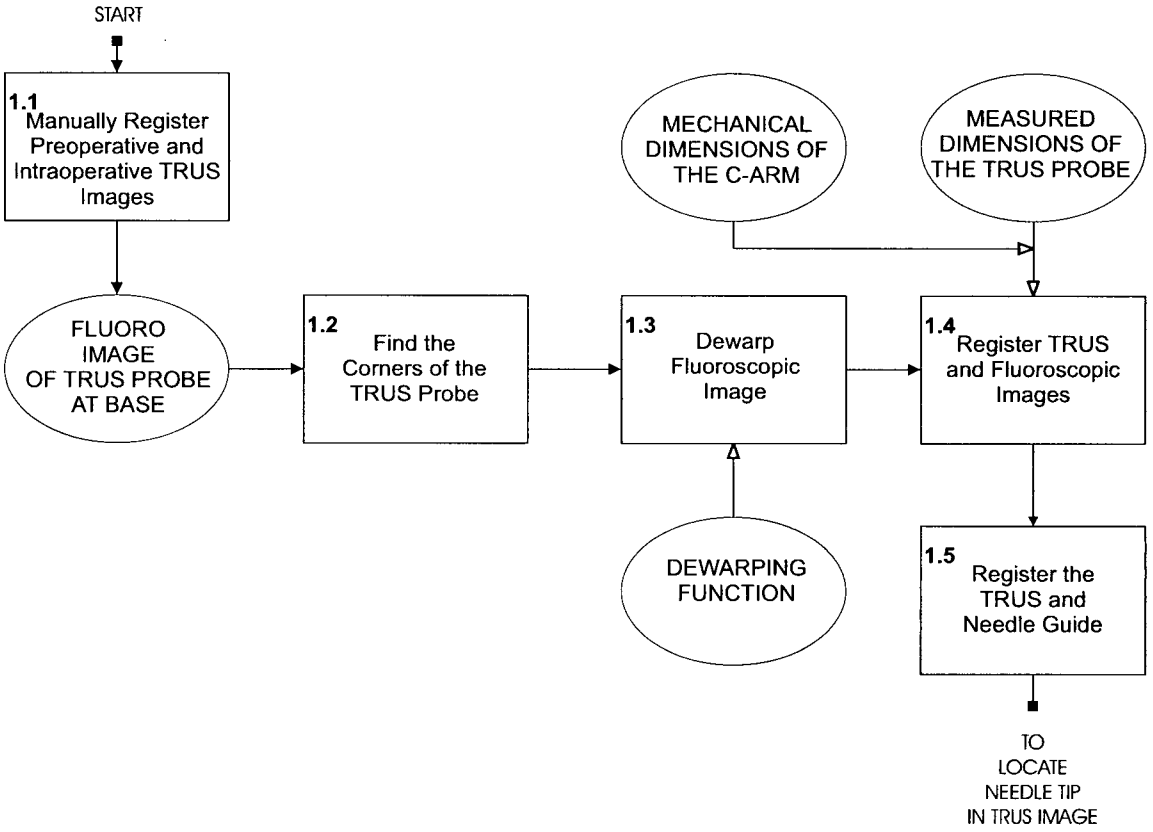

Figure 2.1: A flow chart of Block 1 of Figure 1.6 showing the calibration method employed in our RTD system

2.2 Registering the Preoperative and Intraoperative TRUS Images

Initially, as is the protocol for prostate brachytherapy at the VCC, the TRUS probe is mounted on the same stage used for the preoperative volume study (see Figure 1.2). The radiation oncologist manually registers the intraoperative TRUS images to the TRUS images from the volume study

(the volume study TRUS images are displayed in a hard copy format adjacent to the ultrasound machine). The stage and stabilizing links are manually adjusted to achieve this calibration step, which ensures the preplanned seed distribution can be accurately implemented.

Once the radiation oncologist is satisfied the preoperative and intraoperative images are registered the probe is inserted to the base of the prostate and a fluoroscopic image is acquired.

2.3 Finding the Corners of the TRUS Probe

2.3.1 Background on Fluoroscopy

Figure 2.2 is a simplified diagram of the C-arm of a fluoroscope. The C-arm consists an X-ray source and an image intensifier. The photons are emitted by the source and travel through the object being imaged to the image intensifier, where they first hit the photocathode. The photocathode converts the photons to electrons which are accelerated and focussed onto the output phosphor. The image of the output phosphor is captured with a camera.

The fluoroscope used for prostate brachytherapy at the VCC is the GE Series 9600 C-arm

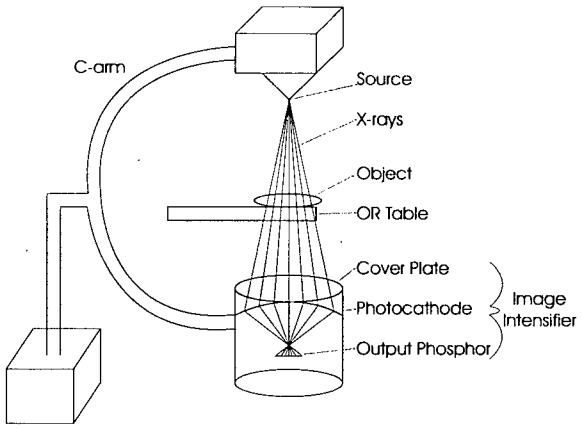

Figure 2.2: A simplified diagram of a C-arm fluoroscope

(General Healthcare). Images can be saved to the machine's hard drive and exported in a 256 gray-scale format through a 3.5-inch floppy drive.

The C-arm produces projection images. The X-rays travel in a conical path with the source modelled as a single point. Objects in the path of the X-rays attenuate the energy of the X-rays

according to the following equation:

$$N = N_o e^{-\mu t} \tag{2.1}$$

where N is the number of photons absorbed, N_o is the number of photons incident on the object, μ is the linear attenuation coefficient, which depends of the object's composition, and t is the thickness of the object. As an example, metals have a significantly higher attenuation coefficient then tissue, so they absorb more X-rays than the surrounding tissue of the same thickness, resulting in a dark artifact in the image.

2.3.2 Delineating the TRUS Probe Artifact

Because a fluoroscopic image of the TRUS probe and the physical dimensions of the probe are used to register the TRUS and fluoroscopic images, several dimensions of the TRUS probe artifact (see Figure 2.3a) in the fluoroscopic image must be determined. The probe artifact could be manually delineated from the image, but to save time and improve accuracy, the TRUS artifact is automatically delineated from the fluoroscopic image. The algorithm used to find the corners of the TRUS probe artifact in the fluoroscopic image, I_{org}, is given as Algorithm 1.

The corners of the probe are roughly selected by the user (for example, a radiation therapist). This input is used to approximate the location of the edges and to crop the image to a region of interest (ROI) reducing processing time. By approximating the edges, the detected edge points can be sorted and later used to fit a line to each edge.

Noise in these fluoroscopic images has several major contributing factors: inherent image noise, variance in patient anatomy, the variability of imaging parameters and the position of the C-arm relative to the patient. Furthermore, the bed is part of the image background and a catheter artifact is occasionally present. As in [53] and [57], a median filter is applied to the cropped image to reduce the noise.

As is evident in Figure 2.3a the background of the fluoroscopic image is not constant. This results from the operating table appearing in only the upper half of the image and various anatomical structures (such as the pubic arch) in the image. To help compensate for this the image is processed on a row-by-row and column-by-column basis. Each pixel is normalized as followings:

$$I_{norm}(x,z) = \frac{I(x,z)}{\sqrt{\sum I^2_{array}}}. \tag{2.2}$$

where $I_{norm}(x, z)$ is the normalized intensity of the pixel at coordinate (x, z), $I(x, z)$ is the intensity of the pixel, and I_{array} is an array of pixel intensities (typically a row or column of the image).

Although the exact composition of the TRUS probe is not known, Figure 2.3a demonstrates the probe attenuates significantly more radiation than the surrounding soft tissue. But, instead of producing clear edges, the conical projection model results in blurring at the edge of the probe artifact, referred to as edge effects. Some of the X-rays pass through only a portion of the object, so less radiation is attenuated resulting in blurring. This blurring produces an intensity gradient from artifact to the background of the image. These edge effects are illustrated in Figure 2.4b which is the intensity profile of one row of pixels in Figure 2.4a.

Next, the 1D gradient, I_{grad}, for each row and column of the image is approximated by taking the difference in intensity between adjacent pixels. If the gradient of the i^{th} pixel exceeds fixed gradient threshold, T_{grad}, then the edge point, X_{edge}, is computed as an average weighted by the gradient of the surrounding pixels:

$$X_{edge} = \frac{\sum_{j=-S}^{S} (i+j) \cdot |I_{grad}(i+j)|}{\sum_{j=-S}^{S} |I_{grad}(i+j)|}, \tag{2.3}$$

where S defines the search region in pixels. The values for S and T_{grad} were experimentally determined from tests on fluoroscopic images of the TRUS probe. The edge points of the TRUS probe artifact shown in Figure 2.3a are plotted in Figure 2.3b.

As can be seen in Figure 2.3b many edge points are found. To fit a line to the edges of the probe artifact these edge points must be sorted according to the edge they represent. Using the corners estimated by the user and the known dimensions of the probe each edge point is assigned to one of the edges of the probe or discarded as a potential edge point. Next, the edge points are dewarped (see Section 2.4 for the details of the dewarping algorithm). A first order line is fitted to each set of edge points using a least-squares minimization. The intersection of the horizontal and vertical edges are the corners of the TRUS probe artifact used for the registration algorithm present in Section 2.5. The results of finding the corners of the TRUS probe in Figure 2.3a are given in Figure 2.3c.

Algorithm 1 The algorithm to find the corners of TRUS probe in a fluoroscopic image

Input: I_{org} - a fluoroscopic image of the TRUS probe

Roughly select the corners of the probe artifact (manually)
$I = crop(I_{org})$
Estimate the location of probe edges
Apply median filter to I
for n = 1 to number of rows in I **do**
  $I_{array} = I(n,:)$ $\{I(n,:)$ is the nth row of pixels in $I\}$
  I_{norm} = normalize(I_{array})
  X_{edge_h} = Find edge points in I_{norm}
  Sort X_{edge_h} based on estimated edge locations
end for
for m = 1 to number of columns in I **do**
  $I_{array} = I(:,m)$ $\{I(:,m)$ is the mth column of pixels in $I\}$
  I_{norm} = normalize(I_{array})
  X_{edge_v} = Find edge points in I_{norm}
  Sort X_{edge_v} based on estimated edge locations
end for
Dewarp X_{edge_h} and X_{edge_v}
Fit first-order line to each edge
$X_{corners}$ = Find intersection of the horizontal and vertical edges

Output: $X_{corners}$ - the corners of the TRUS probe artifact in the fluoroscopic image I_{org}

2.4 Dewarping of Fluoroscopic Images

There are two types of distortion (i.e. warping) present in fluoroscopic images: pincushion distortion and S-distortion [51]. Pincushion distortion results from the spherical shape of the photocathode focusing the electrons onto the flat plane of the output phosphors (see Figure 2.2), causing the outward displacement of pixels from their undistorted position. S-distortion is caused by magnetic fields acting on the electrons as they travel from the photocathode to the output phosphors. The magnetic fields result from the Earth's magnetic core and local sources, such as the cathode ray tube (CRT) in the display of the fluoroscope. S-distortion causes translations and rotations, which may not be uniform for all pixels. This causes a straight line to appear as a S-shaped line in the fluoroscopic image. S-distortion is dependent on the location and orientation of the C-arm, while pincushion distortion is constant for a given C-arm.

The warping in the image can be measured using a grid of fiducial markers with a known geometry. Figure 2.5a is a fluoroscopic image of an 11 X 11 grid of steal ball bearings embedded in

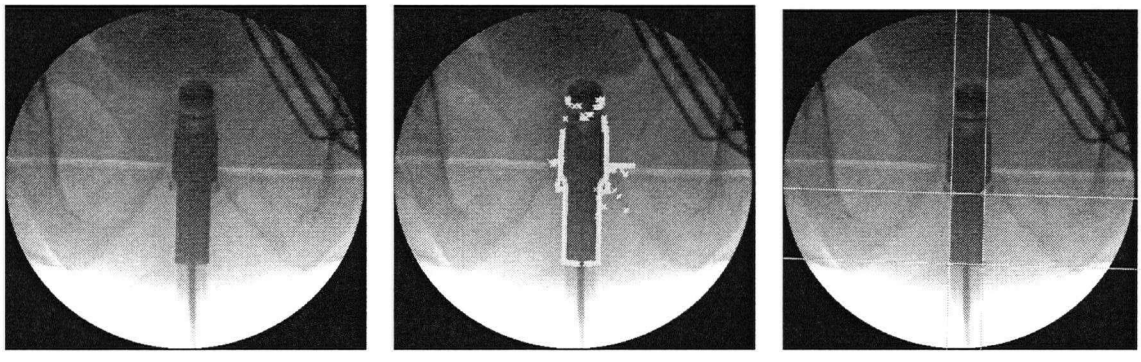

(a) (b) (c)

Figure 2.3: (a) A fluoroscopic image of the TRUS probe, (b) the detected edge points, (c) the detected edges (the intersections of the edges are defined as the corners of the probe artifact)

Plexiglas. By observation, some pincushion distortion is visible in the ball bearings furthest from the center. This is better highlighted in Figure 2.5b by plotting just the coordinates of the ball bearings. S-distortion is clearly illustrated in Figure 2.5c by plotting the coordinates of one row of ball bearings.

2.4.1 Dewarping Functions

To remove image warping, the warping can be modelled to define one or more transformations from the warped image to the undistorted image. These transformations are referred to as the dewarping function.

Dewarping functions can usually be classified as either global or local. Global functions define one transformation for the whole image, while local functions subdivide the image into elements and define a transformation for each element. Global functions tend be less accurate, but can be implemented using physically-based principles. Local functions are more accurate, but are not physically-based, so they must be redefined when the C-arm is rotated or translated. Furthermore, local functions can have discontinuities at the boundaries of the elements. Localized functions smoothed with a global function give good results, but are non-linear and of higher order than other models [51].

Selecting a dewarping function is dependent on the C-arm, the application, the grid, the region of interest in the image, the accuracy required, the time available to compute the unwarped coor-

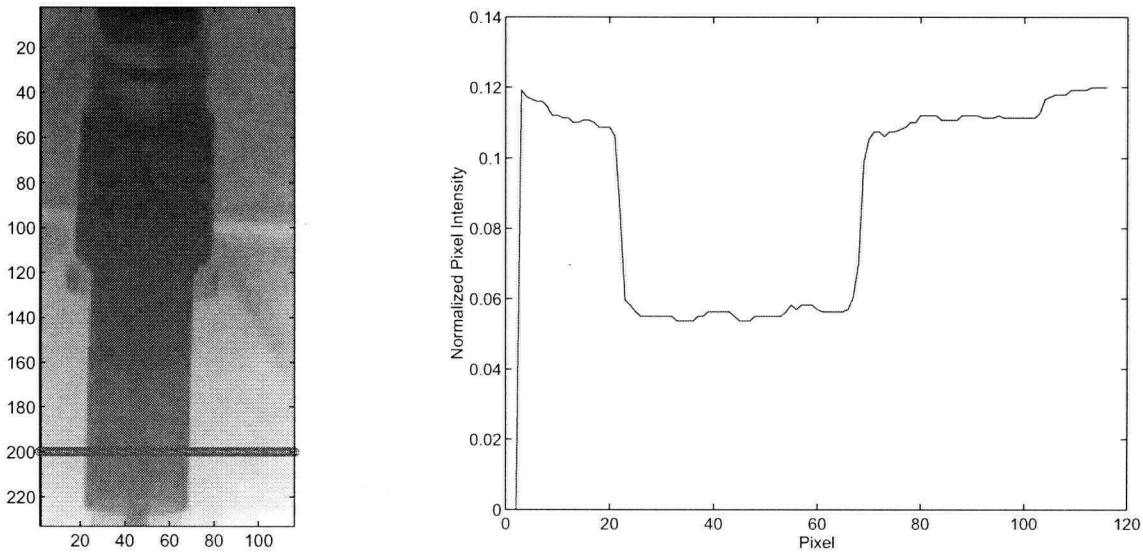

(a) (b)

Figure 2.4: (a) A cropped image of the TRUS probe, and (b) a plot of the intensity profile for the horizontal red line in (a) to show the edge effects observed in a fluoroscopic image of the TRUS probe.

dinates, and whether the dewarping will be done online or offline. For our RTD system the ROI is the region most likely to contain the TRUS probe and seed artifacts. Referring to Figure 2.5a this region includes the whole height of the image, but excludes the two columns of ball bearings on the far left and right of the dewarping jig. For RTD the computation of the unwarped image must be fast and can be sped up by only dewarping the coordinates of the seeds or edge points, rather than dewarping the whole image and interpolating a new image.

It is desirable to determine the dewarping function offline and use the same function for all cases, but online dewarping is possible. One approach is to leave a dewarping grid on for the entire procedure, but the grid may distort or block some of the seed artifacts. Alternatively, since the C-arm is not moved during the procedure and the equipment used for the procedure is always turned on for the entire procedure, the magnetic fields in the room are fairly constant. Therefore, the grid could be placed on the detector and removed after a calibration image is acquired. But, if the warping function only slightly changes between procedures it will be ideal to use the same function for all procedures eliminating additional calibration steps.

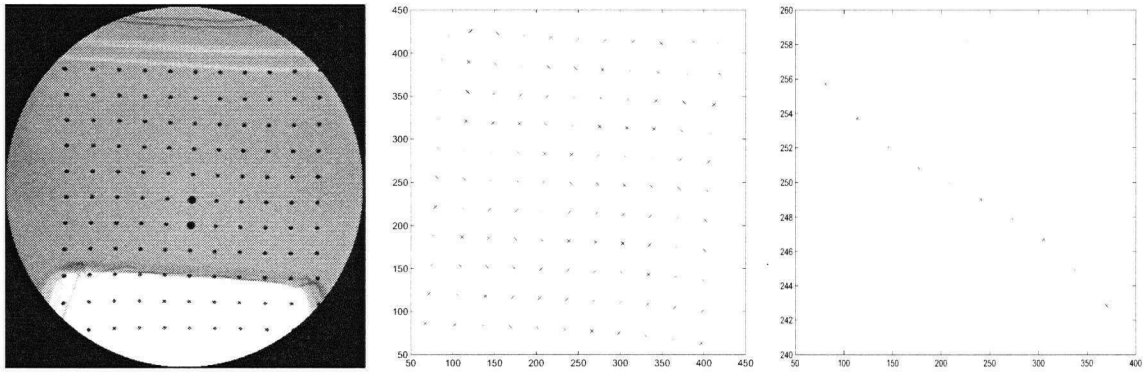

(a) (b) (c)

Figure 2.5: (a) A fluoroscopic image of the 11 X 11 grid of steal ball bearings. (b) A plot of the coordinates of the ball bearing to demonstrate pincushion distortion. (c) A plot of one row of ball bearings to demonstrate S-distortion

However, determining the optimal dewarping model for the C-arm is beyond the scope of this thesis, so just two methods are considered: a local method and a global physical method. These functions are described in Appendix A. The dewarping algorithm is implemented such that it can be easily changed without effecting the remaining components of the system.

An optimal dewarping function for fluoroscopic images has not been established in the literature. For example, the three-film RTD system in [23] uses a bilinear coordinate transform and cubic-convolution to estimate pixel intensities. A similar system reported in [57] uses a 5^{th}-order polynomial to globally dewarp the image. Another three-film RTD system in [52] does not report a dewarping method. In [51], Tang does an extensive review of dewarping functions without establishing an optimal function, but chooses a local linear model to dewarp fluoroscopic images as part of a 3D registration algorithm.

2.4.2 Experimental Results

To test the two dewarping functions, described in Appendix A, steel ball-bearings (referred to as test points) were added to the Plexiglas jig in Figure 2.5a at known locations inside the elements, on the boundary of elements and at the intersection of four elements (see Figure 2.6a). Fluoroscopic images of this test grid were acquired with the C-arm displaced and rotated about the typical position and orientation used during implants to account for slightly variances in setup. Throughout the

experiment, all the equipment, including the monitors of the fluoroscope, the ultrasound machine and anaesthetist's monitoring station, were turned on to ensure all magnetic fields that are locally-generated were present.

The centroids of the test points and the tie points in the fluoroscopic image were found using a thresholding technique and were manually verified. The dewarping functions were defined for both models using the images acquired when the C-arm was not rotated about either axes, which is typically the desired orientation for an implant. The center and radius of the fluoroscopic image was determined using the software presented in [3]. The center and radius of the fluoroscopic image was within 0.25 mm for all the images. The results with no dewarping, dewarping with the local model, and dewarping with the global model are given in Tables 2.1, 2.2 and 2.3, respectively.

Table 2.1: Error in localizing the test points caused by warping

Position and Orientation			Region of Interest (mm)			Entire Image (mm)		
trans (m)	θ_z (deg)	θ_x (deg)	Mean	Max	STD	Mean	Max	STD
0	0	0	0.85	3.10	0.67	1.08	3.16	0.80
0	0	5	0.75	3.09	0.72	0.95	3.09	0.81
0	0	6	0.86	3.16	0.72	1.07	3.16	0.81
0	5	5	0.78	3.03	0.67	1.00	3.03	0.79
0	0	-5	0.94	3.16	0.69	1.18	3.27	0.83
0	-5	5	0.82	3.23	0.75	1.02	3.23	0.83
0.75 (-z)	0	0	0.79	1.61	0.38	0.81	2.05	0.46
0.75 (-z)	5	-5	0.87	1.66	0.40	0.88	1.72	0.42
0.75 (-z)	-5	-5	0.87	1.86	0.47	0.90	2.19	0.52
0.25 (+y)	0	0	0.82	1.71	0.42	0.85	2.30	0.48

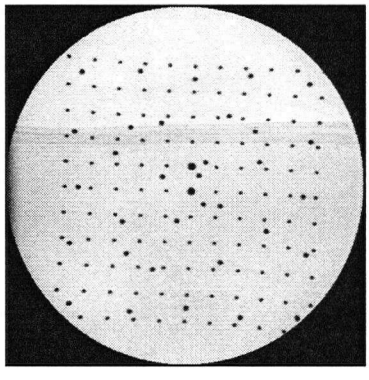

Figure 2.6: A fluoroscopic image of the modified dewarping jig used to test the dewarping models.

Table 2.2: Error in dewarping the test points using the local method

Position and Orientation			Region of Interest (mm)			Entire Image (mm)		
trans (m)	θ_z (deg)	θ_x (deg)	Mean	Max	STD	Mean	Max	STD
0	0	0	0.14	0.34	0.07	0.14	0.36	0.07
0	0	5	0.18	0.38	0.10	0.20	0.38	0.10
0	0	6	0.20	0.45	0.11	0.21	0.45	0.11
0	5	5	0.20	0.31	0.07	0.19	0.31	0.07
0	0	-5	0.16	0.57	0.13	0.19	0.57	0.14
0	-5	5	0.18	0.40	0.12	0.20	0.44	0.12
0.75 (-z)	0	0	1.05	1.99	0.50	1.15	2.03	0.50
0.75 (-z)	5	-5	1.12	1.84	0.48	1.23	1.84	0.47
0.75 (-z)	-5	-5	1.13	2.02	0.52	1.23	2.26	0.56
0.25 (+y)	0	0	1.05	2.05	0.52	1.14	2.16	0.54

Table 2.3: Error in dewarping the test points using the global method

Position and Orientation			Region of Interest (mm)			Entire Image (mm)		
trans (m)	θ_z (deg)	θ_x (deg)	Mean	Max	STD	Mean	Max	STD
0	0	0	0.38	1.04	0.21	0.45	1.27	0.26
0	0	5	0.40	0.67	0.18	0.45	1.02	0.22
0	0	6	0.41	0.76	0.17	0.46	1.06	0.23
0	5	5	0.39	0.91	0.19	0.46	1.16	0.23
0	0	-5	0.41	1.29	0.25	0.48	1.55	0.32
0	-5	5	0.42	0.67	0.16	0.46	0.95	0.19
0.75 (-z)	0	0	1.09	2.00	0.56	1.18	2.31	0.62
0.75 (-z)	5	-5	1.16	2.08	0.55	1.24	2.28	0.58
0.75 (-z)	-5	-5	1.17	2.14	0.57	1.26	2.76	0.67
0.25 (+y)	0	0	1.10	1.92	0.58	1.18	2.43	0.64

The results in Table 2.1 show the maximum error in the position of test points is 3.23 mm. However, both the local and global dewarping functions reduce the error caused by warping when the C-arm is not translated to 0.57 mm and 1.55 mm, respectively. As expected the local function reduces

both the mean and maximum error more than the global function. However, according to Table 2.1 when the C-arm is translated the characteristics of the warping change because the magnetic fields acting on the electrons change. So, when the dewarping functions defined before the translation are applied to these images they introduce more error than the warping itself. Similar results where dewarping can introduce more error than the warping itself are reported in [59].

Fortunately, the position of the bed is marked on the floor of the operating room, so the position of the C-arm is quite consistent between procedures. Therefore, the same dewarping function can be used for all procedures. The local dewarping method will be used for the remainder of this work because it best reduces the amount of error caused by warping.

2.5 Registering TRUS and Fluoroscopic Images

Registration defines the transformation between two data sets. In this work, the fluoroscopic and TRUS images contain the data of interest. The (x,z)-coordinates of the seeds in the fluoroscopic image are projected back to the TRUS image frame, so the y-coordinate can be determined, and ultimately the 3D seed distribution with respect to the base frame (and prostate). The transformation between the TRUS and fluoroscopic images must be known to project the seeds found in the fluoroscopic image back to the TRUS frame, such that:

$$X_{TRUS} = T_{FT} \cdot X_{FLUORO}, \tag{2.4}$$

where X_{TRUS} and X_{FLUORO} are (x,z)-coordinates in the TRUS and fluoroscopic images, respectively and T_{FT} is the transformation from the fluoroscopic image to the TRUS image. In general, a 3D affine transformation, T, is defined as:

$$T = \begin{bmatrix} s_x c(\theta_z)c(\theta_y) & c(\theta_z)s(\theta_y)s(\theta_x) - s(\theta_z)c(\theta_x) & c(\theta_z)s(\theta_y)c(\theta_x) + s(\theta_z)s(\theta_x) & d_x \\ s(\theta_z)c(\theta_y) & s_y s(\theta_z)s(\theta_y)s(\theta_x) + c(\theta_z)c(\theta_x) & s(\theta_z)s(\theta_y)c(\theta_x) - c(\theta_z)s(\theta_x) & d_y \\ -s(\theta_y) & c(\theta_y)s(\theta_x) & s_z c(\theta_y)c(\theta_x) & d_z \\ 0 & 0 & 0 & 1 \end{bmatrix}, \tag{2.5}$$

where the functions cosine and sin are abbreviated c and s and θ_x, θ_y, and θ_z are the rotations about the x, y and z-axes, respectively. The scaling of the x, y, and z-axes are represented as s_x,

s_y, and s_z, respectively. The translations in the x, y, and z directions are represented by d_x, d_y, and d_z, respectively.

However, in this case, the y-coordinates of the seeds are not determined from the fluoroscopic image. And, the rotation about the z-axis is assumed to be zero because the C-arm is locked orthogonal to the (x,z)-plane of the base frame. So, the homogenous transformation between the fluoroscopic and TRUS images, T_{FT}, simplifies to:

$$T_{FT} = \begin{bmatrix} s_x cos(\theta_y) & sin(\theta_y)cos(\theta_x) & d_x \\ -sin(\theta_y) & s_z cos(\theta_y)cos(\theta_x) & d_z \\ 0 & 0 & 1 \end{bmatrix}. \tag{2.6}$$

2.5.1 Prior Work

In [51], six or seven fiducial markers with known geometry have been used to determine the pose of the object from a single fluoroscopic image with 1 mm and 2 degrees of accuracy. TRUS and fluoroscopic images have been fused in [23] by detecting four needle tips in both TRUS and fluoroscopic images. As mentioned in Section 1.2, [53] uses a special TRUS probe equipped with fiducial markers for point-based registration between fluoroscopic and TRUS images. In [50] implanted seeds have been used as fiducial markers to register TRUS and fluoroscopic images with 3 mm accuracy in a phantom. And, in [4] three gold fiducial markers have been used to register TRUS and fluoroscopic images. A system has been proposed at John Hopkins University where a wire-stealth is placed over a TRUS probe. This allows the TRUS and fluoroscopic images to be registered [30].

2.5.2 Method

To the best of our knowledge the TRUS probe artifact has not been used to register TRUS and fluoroscopic images. However, using the corners of the probe artifact in the fluoroscopic image, the physical dimensions of the probe, the source to image distance of the C-arm, and the resolution of the fluoroscopic and TRUS images, a homogenous coordinate transformation from a single fluoroscopic image to the TRUS image can be determined as follows.

The registration algorithm is based on similar triangles, but does not constrain the probe to be centered on the isocentric axis of the C-arm. Instead, the projection model uses a chord of the cross-section of the TRUS probe to determine the transformation. This chord is defined by the line

connecting the two points where the radiation beams from the source are tangent to the edge of the probe (see Figure 2.8). Secondly, the method considers two cases depending on the position of the probe artifact with respect to the vertical midline of the fluoroscopic image.

Using the corners of the probe artifact in the fluoroscopic image, the physical dimensions of the probe, the source to image distance of the C-arm, and the resolution of the fluoroscopic and TRUS images, a homogenous coordinate transformation between the two images is defined:

$$T_{FT} = \begin{bmatrix} s_x cos(\theta_y) & sin(\theta_y)cos(\theta_x) & d_x \\ -sin(\theta_y) & s_z cos(\theta_y)cos(\theta_x) & d_z \\ 0 & 0 & 1 \end{bmatrix}, \tag{2.7}$$

where θ_x and θ_y are the rotations about the x and y-axes, respectively. The s_x and s_z are the scaling of the x and z coordinates from the fluoroscopic to TRUS images, respectively, derived from the resolution of both images and the fluoroscopic projection model. The translations in the x and z directions are represented by d_x and d_z, respectively. Because the y-coordinates of the seeds are determined in the TRUS image frame, scale and translation terms in the y-direction are not included in Equation 2.7. Furthermore, the rotation about the z-axis is assumed to be small as the C-arm is locked orthogonal to the (x,z)-plane (see Section 2.5.3). The coordinate systems referred to throughout this proof are shown in Figure 1.5.

2.5.2.1 Determining θ_y

First, the rotation of the TRUS probe about the y-axis, θ_y, is determined. Referring to Figure 2.7, which is a top view of the probe artifact (i.e. from the perspective of the source in the C-arm), θ_y is calculated as follows:

$$\theta_y = \frac{\pi}{2} - atan\left(\frac{x_A - x_B}{z_A - z_B}\right), \tag{2.8}$$

where the coordinates of the corners of the probe are denoted (x_A, z_A) and (x_B, z_B).

2.5.2.2 Determining d_y

Although d_y is not included in Equation 2.7 it must be determined, so the coordinates of the seeds found in the fluoroscopic image can be back-projected to the TRUS image. Using θ_y, (x_A, z_A) and (x_B, z_B), are rotated about the y-axis and designated (x'_A, z'_A) and (x'_B, z'_B), respectively. Denoting

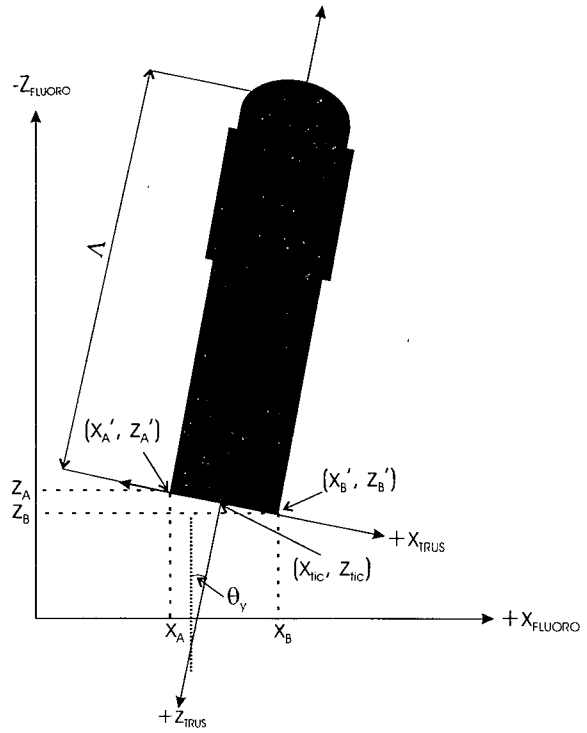

Figure 2.7: A top view of the TRUS probe artifact in the fluoroscopic image

the coordinate of the center of the fluoroscopic image as (x_{fic}, z_{fic}) and referring to Figure 2.8, we can determine the distance from the center of the probe artifact to (x_{fic}, z_{fic}), denoted x_{ic}, as follows:

$$x_{ic} = x_{fic} - \frac{x'_A + x'_B}{2}. \tag{2.9}$$

Next, the distances from each edge of the probe artifact to x_{fic} are denoted x_{idA} and x_{idB}, which are determined as follows:

$$x_{idA} = min(|x'_A - x_{fic}|, |x'_B - x_{fic}|) \tag{2.10}$$

$$x_{idB} = max(|x'_A - x_{fic}|, |x'_B - x_{fic}|). \tag{2.11}$$

Now, two cases based on the position of the TRUS probe artifact with respect to the fluoroscopic image must be considered: when the probe artifact does overlap and does not overlap the vertical midline of the fluoroscopic image.

Case I: Probe Artifact Does Overlap Vertical Midline of the Image

In this case the probe artifact overlaps x_{fic} as illustrated in Figure 2.8. Denoting the source to image distance as H and the radius of the TRUS probe as R_o, and referring to Figure 2.8, the vertical distance from the fluoroscopic image plane to the TRUS probe, d_y, can be determined as follows:

$$\theta_A = atan\left(\frac{H}{x_{idA}}\right) \tag{2.12}$$

$$\theta_B = atan\left(\frac{H}{x_{idB}}\right) \tag{2.13}$$

$$\theta_E = atan\left(\frac{x_{ic}}{H}\right) \tag{2.14}$$

$$\theta_F = \frac{\pi}{2} - \theta_A \tag{2.15}$$

$$\theta_C = \frac{\pi}{2} - \theta_B \tag{2.16}$$

$$\theta_D = \theta_C - \theta_E \tag{2.17}$$

$$K = \frac{R_o}{sin(\theta_D)} \tag{2.18}$$

$$d_y = H - K \cdot cos(\theta_E). \tag{2.19}$$

Case II: Probe Artifact Does Not Overlap the Vertical Midline of the Image

In this case the probe artifact does not overlap x_{fic} as illustrated in Figure 2.9. Again, denoting the source to image distance as H and the radius of the TRUS probe as R_o, and referring to Figure 2.9, the distance from the fluoroscopic image plane to the TRUS probe, d_y, can be determined as follows:

$$\theta_C = atan\left(\frac{x_{idA}}{H}\right) \tag{2.20}$$

$$\theta_B = atan\left(\frac{x_{idB}}{H}\right) - \theta_C \tag{2.21}$$

$$K = \frac{R_o}{tan(\frac{\theta_B}{2})} \tag{2.22}$$

$$\theta_A = \frac{\pi}{2} - \frac{\theta_B}{2} \tag{2.23}$$

$$L = sin(\frac{\pi}{2} - \theta_A) \cdot R_o \tag{2.24}$$

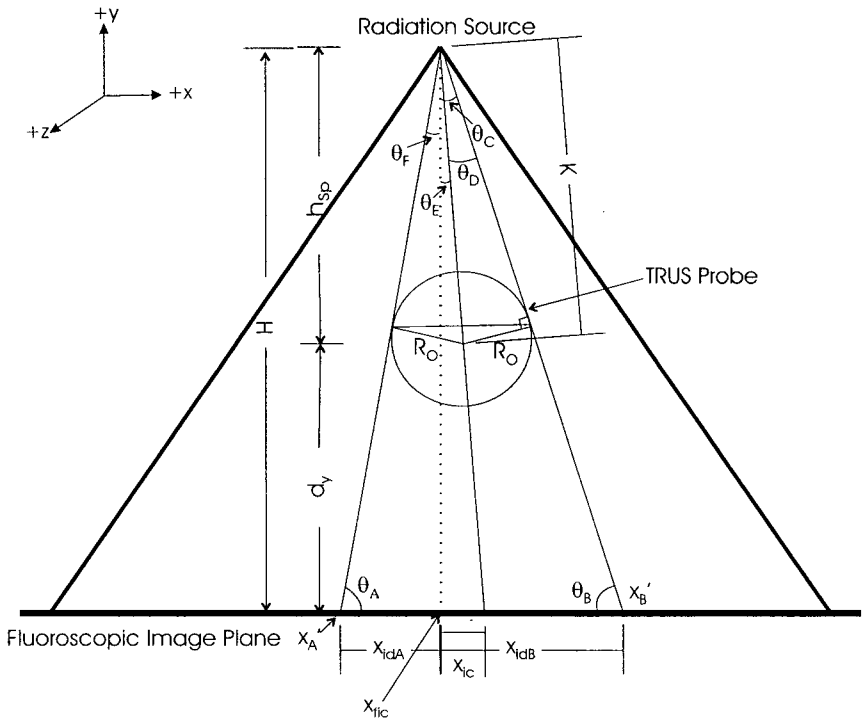

Figure 2.8: Case I: The TRUS probe artifact does overlap the vertical midline of the fluoroscopic image.

$$d_y = H - (K + L) \cdot cos(\theta_C + \frac{\theta_B}{2}). \tag{2.25}$$

2.5.2.3 Determining s_x and s_z

The variables s_x and s_z represent the ratio of the fluoroscopic and TRUS image resolutions and the back-projection from the fluoroscopic image space to TRUS image space. Thus, s_x and s_z are both a function of the image resolutions and the height of the TRUS probe from the fluoroscopic image:

$$s_x = \left(\frac{H - d_y}{H}\right) \cdot \left(\frac{rx_{TRUS}}{rx_{fluoro}}\right) \tag{2.26}$$

$$s_z = \left(\frac{H - d_y}{H}\right) \left(\frac{rz_{TRUS}}{rz_{fluoro}}\right), \tag{2.27}$$

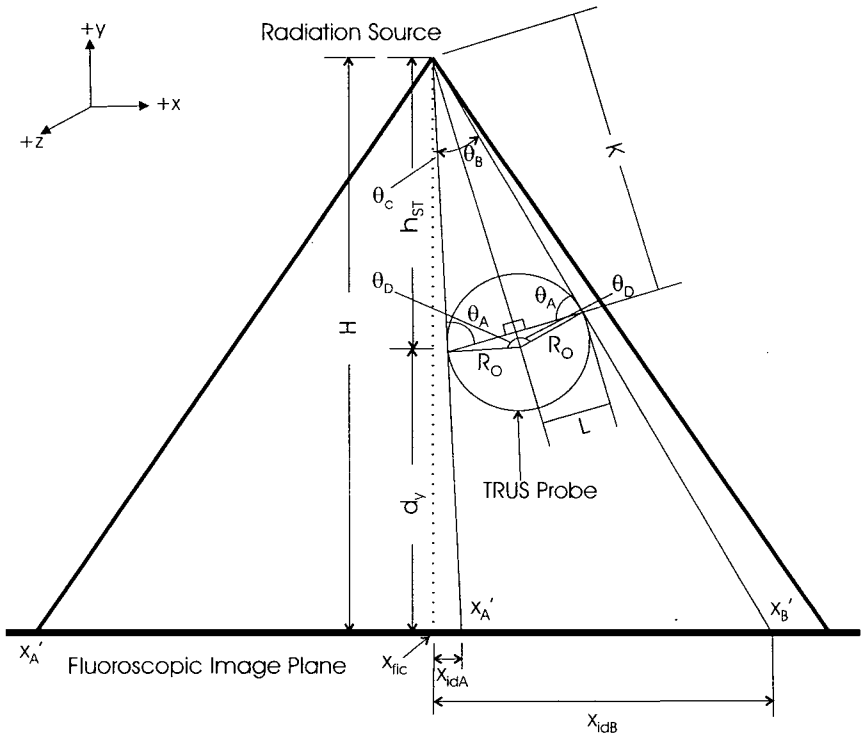

Figure 2.9: Case II: The TRUS probe artifact does not overlap the vertical midline of the fluoroscopic image.

where the resolution of the TRUS and fluoroscopic images (in millimeters per pixels) are denoted in rx_{trus} and rx_{fluoro} in the x-direction and rz_{trus} and rz_{fluoro} in the z-axis, respectively.

2.5.2.4 Determining d_x and d_z

The center of the TRUS probe artifact corresponds to the center of the TRUS image projected to the fluoroscopic image and is denoted (x_{tic}, z_{tic}). To compute the translation from the fluoroscopic image to the TRUS image, the seed coordinates and the center of the TRUS image are defined with respect to the center of the fluoroscopic image, (x_{fic}, z_{fic}). Then, these coordinates are back-projected to the TRUS image and redefined with respect to the left edge of the TRUS image, yielding:

$$d_x = \left(\frac{x'_A + x'_B}{2} - x_{fic} \right) \cdot s_x + x_{tic}. \tag{2.28}$$

Using a similar method d_z is computed, except the TRUS image does not correspond to the line connecting x'_A and x'_B. Referring to Figure 2.7, an offset must be added to d_z, to compensate

for the distance from the corners to the image plane of TRUS, when it is imaging the base of the prostate, Λ:

$$d_z = \left(\frac{z'_A + z'_B}{2} - z_{fic} \right) \cdot s_z + z_{tic} + \Lambda. \tag{2.29}$$

2.5.2.5 Determining θ_x

Referring to Figure 2.10, the rotation about the x-axis, θ_x, is computed by determining the height of the TRUS probe above the fluoroscopic image at another point, d'_y, on the probe artifact. Knowing the distance, Π, along the z-axis of the probe, the rotation about the x-axis can be determined as follows:

$$\theta_x = arcsin(\frac{d_y - d'_y}{\Pi}). \tag{2.30}$$

2.5.3 Error Analysis

The accuracy of the registration algorithm is most sensitive to the height of the TRUS frame above the fluoroscopic image plane denoted d_y. The accuracy with which the height of the probe can be

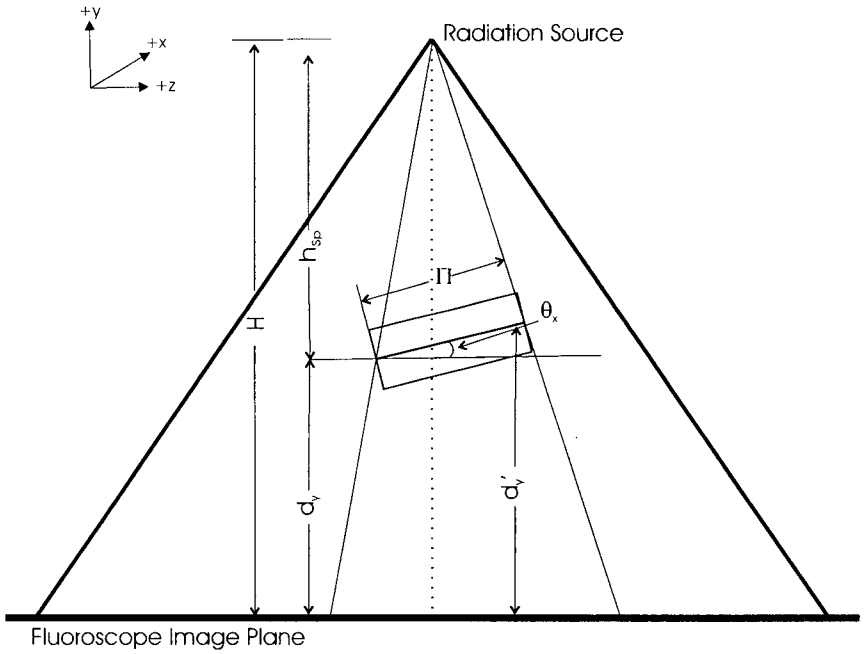

Figure 2.10: A side view of the TRUS probe and the fluoroscopic image plane.

determined is a function of image resolution and the true height of the probe. Figure 2.12a shows the error in determining d_y as a function of image resolution for several different heights.

Because the resolution of the fluoroscopic images is only slightly better than 0.5 mm/pixel, the height of small objects, such as seeds, cannot be determined from a fluoroscopic image. However, by fitting a line to the edge points on the probe, the resolution of the fluoroscopic can be improved. This allows the height of the probe to be determined with reasonable accuracy as demonstrated in the next section through experimental results.

Referring to Equation 2.26 and 2.27, we see that s_x and s_z are dependent on d_y. However, the triangle formed between the point source and the fluoroscopic image is sufficiently steep (see Figure 2.11) because the ratio of Δy and Δx is large. Therefore, errors in determining the height result in only a small error when back-projecting coordinates from the fluoroscopic image to the TRUS image frame. The error in back-projecting points from the (x,z)-plane as a function of error in the height is shown in Figure 2.12b for a point 10 mm from the center of the fluoroscopic image.

Fortunately, both the TRUS and fluoroscopic axis (see Figure 1.5) are roughly parallel so θ_x,

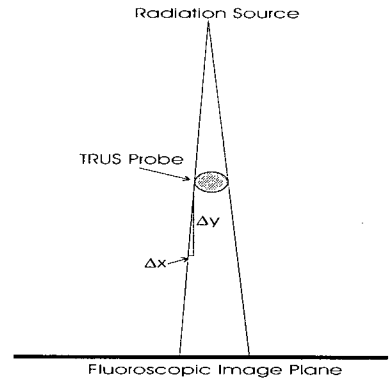

Figure 2.11: A simple model of the fluoroscopic projection image.

θ_y, and θ_z are small. As shown above, θ_y can be computed with reasonable accuracy. However, θ_x is more error prone as shown in the experimental results given in the next section. We see from Equation 2.6 the cosine of θ_x is used to compute the transformation, so if θ_x is small the function will be close to one. We assume θ_z is zero because the fluoroscopic image is positioned orthogonal to the (x,z)-plane of the TRUS image. Therefore, θ_z is not present in Equation 2.5.

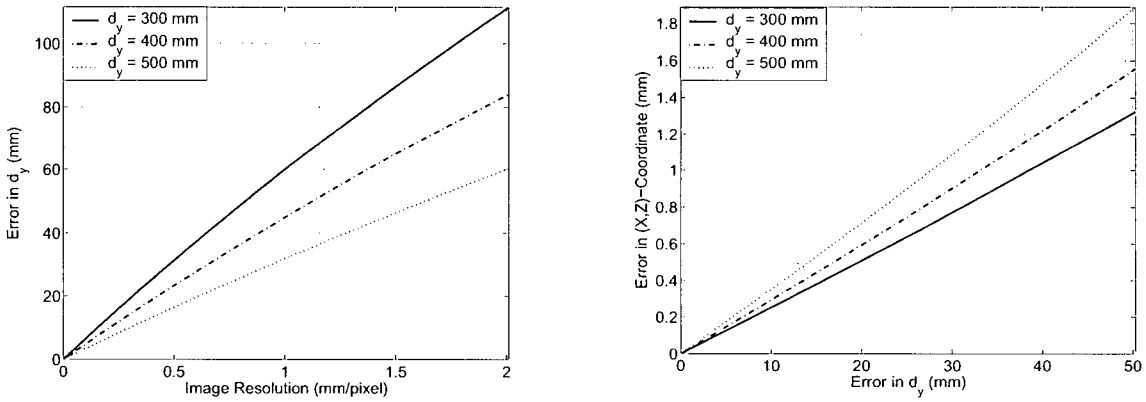

(a) (b)

Figure 2.12: (a) The error in d_y as a function of fluoroscopic image resolution, and (b) the error in back projecting the (x,z)-coordinates as a function of error in d_y.

2.5.4 Results

Our registration algorithm was tested in the operating room at the VCC used for prostate brachytherapy. The setup shown in Figure 1.2 was mounted to the bed. Using the fine vertical adjustment of the stage the vertical position of the probe was incrementally adjusted and measured before a fluoroscopic image was acquired. The rotation about both the x and y-axes was measured to be approximately zero and the C-arm was locked orthogonal to the (x,z)-plane. Two experiments were done, the first with the probe overlapping the vertical midline of the fluoroscopic image and the second with the probe not overlapping the vertical midline of the fluoroscopic image. In both cases the images were dewarped as described in Section 2.4.1.

With the probe artifact overlapping the vertical midline of the image, 21 fluoroscopic images at different heights were acquired, ranging from 305 mm to 335 mm above the fluoroscopic image plane. The resulting error is shown in the scatter plot in Figure 2.13a. The mean absolute error is 1.1 mm and a maximum absolute error is 2.8 mm. The mean error in computing the rotation about the x-axis was reported to be 6.17 degrees.

With the probe artifact off-center, such that the artifact does not overlap the vertical midline of the image, 15 fluoroscopic images at different heights were acquired, ranging from 282 mm to 312 mm. The resulting error is shown in the scatter plot in Figure 2.13b. The mean absolute error

is 1.6 mm and a maximum absolute error is 5.8 mm. The mean error in computing the rotation about the x-axis was reported to be 3.81 degrees.

The results from both cases are very promising. Referring to Figures 2.12a and 2.12b, the height of the probe can be determined with enough accuracy to back-project the (x,z)-coordinates of the seeds from the fluoroscopic image to the TRUS image space with reasonable accuracy.

The high error in the rotation about the x-axis results from error introduced in determining additional corners of the probe artifact. The bottom of the probe artifact is the only horizontal edge of the probe artifact of significant length. Therefore, only a few edge points are detected for the other dimensions of the probe artifact and thus the edges are poorly delineated. Fortunately, errors in determining θ_x contribute only minimal error to our registration approach as discussed in the previous section.

The accuracy with which the height of the probe can be determined is somewhat surprising, given the steep triangle shown in Figure 2.11 and the resolution of the fluoroscopic image. However, fitting lines to the edges of the probe artifact significantly improves the resolution at which the corners of the TRUS probe are delineated accounting for this high accuracy.

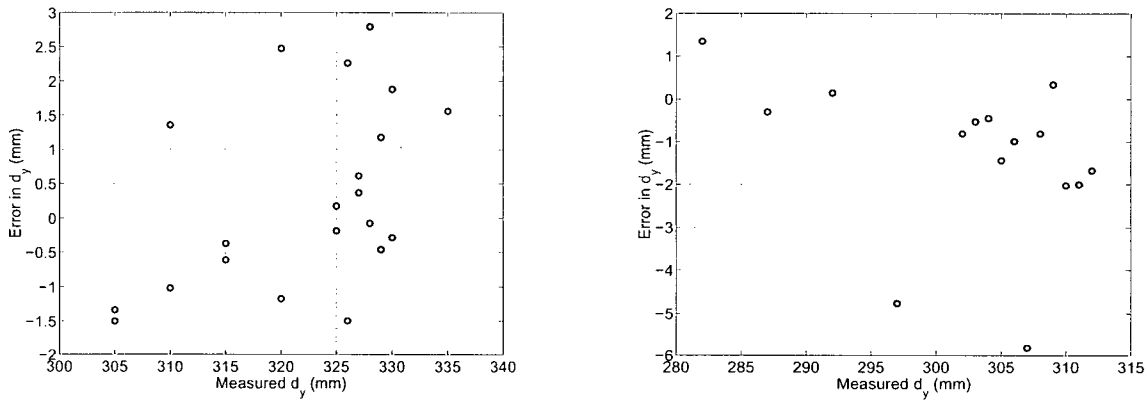

(a) (b)

Figure 2.13: A scatter plot of the error in determining the height of the TRUS probe versus the measured height, when the probe artifact (a) did overlap and (b) did not overlap the vertical midline of the fluoroscopic image

2.6 Registering the TRUS and Needle Guide

Ultimately, the seed distribution is reported in a base frame. The base frame is the needle guide because it is rigidly attached to the TRUS probe and the prostate can easily be defined in this frame. The transformation from a point, X_{TRUS}, in the TRUS image to a point, X_{BASE}, in the base frame is defined as:

$$X_{BASE} = T_{TB} \cdot X_{TRUS}, \tag{2.31}$$

where T_{TB} is defined as:

$$T_{TB} = \begin{bmatrix} s_x & 0 & 0 & 0 \\ 0 & s_y & 0 & d_y \\ 0 & 0 & 0 & d_z \\ 0 & 0 & 0 & 1 \end{bmatrix}. \tag{2.32}$$

The offset in the z-direction, d_z, is determined when the radiation oncologist inserts the first needle, which in the VCC protocol is a needle destined for the base plane (the most superior plane) of the prostate. The TRUS probe is positioned to image the base plane of the prostate, and the needle advanced until a white artifact appears in the TRUS image. The distance from the needle guide to the hub of the needle is measured using a ruler and reported with millimeter accuracy to the radiation therapist. By knowing the length of the needle, L_n, and the distance from the needle guide to the hub of the needle, D_{th}, the displacement of the base plane of the prostate in the z-direction to the needle, d_z, can be determined (see Figure 2.14):

$$d_z = L_n - D_{th}. \tag{2.33}$$

Both coordinate systems are parallel and the scaling constants, s_x and s_y are determined from the known resolution of the TRUS image. Knowing the transformation between the base frame and the TRUS frame, both the TRUS and fluoroscopic images are essentially registered to the base frame of the system.

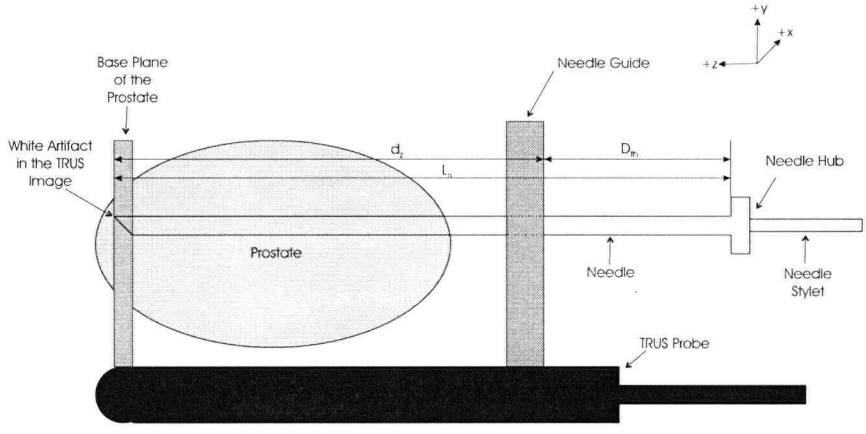

Figure 2.14: A diagram of a needle inserted into the prostate through a needle guide under TRUS guidance

2.7 Conclusion

The calibration procedure for our RTD system fits into the current procedure for prostate brachytherapy with minor modifications. Registering the preoperative and intraoperative TRUS images is currently practiced. An additional fluoroscopic image of the TRUS probe is acquired. The same set of local dewarping transformations will be used for all procedures, as the dewarping varies little with rotation of the C-arm and the C-arm is positioned at roughly at the same location in the operating room. Comparing Figure 2.12b and Figure 2.13 we see the TRUS and fluoroscopic images can be registered accurately enough to determine the (x,z)-coordinates of the seeds in the TRUS frame from a single fluoroscopic image. Finally, registering the TRUS images to the base frame is currently part of the practiced protocol.

Chapter 3

Finding the Needle Tip from TRUS

Because the y-coordinate of the seeds cannot be determined from a single fluoroscopic image, a needle path must be interpolated from the needle tip to the entry point of the needle. The entry point of the needle and the expected location of each needle tip are known from the preoperative plan. However, it is not possible or even desirable to always guide the needle tip to the position given in the preoperative plan. Therefore, the needle tip position must be accurately delineated from TRUS.

It is desirable to automate the needle tip localization step to ensure the system can operate in real-time and within the current protocol used for prostate brachytherapy. This problem can be divided into two distinct problems: identifying the last video frame in TRUS containing a needle tip artifact and locating the needle tip from the artifact in the TRUS image.

3.1 Prior Work

The RTD system presented in [23] uses four needle tip artifacts to register the TRUS and fluoroscopic images. In this work the needle tip artifacts are manually located with an accuracy of 1.1 mm. This work suggests automating needle tip localization in TRUS images is difficult, but improved accuracy might be achieved with 3D US. In [21], which is an early paper on the work presented in this thesis, the needle tips are manually selected. To the best of our knowledge these are the only two works which attempt to localize the needle tip artifact from an image perpendicularly to the needle direction. There are several works that attempt to delineate a needle artifact when the needle direction is parallel to the image plane. In these works the goal is to delineate a

line rather than a point.

In [20], a method for tracking a steerable needle in US is presented. Several filters are tested to reduce image noise and a median filter is selected as an optimal filter. Two techniques are attempted to determine the needle direction: a masking algorithm and fitting a third-order line to the edge points found using an edge detector. The later method is found to be more robust, but delineating the tip needle is still difficult. To overcome this problem the needle is vibrated and power doppler imaging is used to delineate the needle tip.

Another approach for segmenting a needle from a US image is presented in [18]. The goal of this work is to segment a breast biopsy needle from a US image, where the needle is again parallel to the image plane. A variance map is used to remove the speckle in the image. A thresholding technique is implemented to create a binary image, followed by a closing operation to smooth the edges in the binary image. Next, principal component analysis is used to determine the direction of the needle from the clusters of pixels that make up the needle artifact. Once the needle direction is determined the needle tip is found by masking the binary image with the needle path. This paper suggests that prior knowledge of the needle location would be beneficial and that a sequence of images might be used to detect motion between them, and hence, help delineate the needle artifact.

In [15], a method of segmenting a needle from a 3D ultrasound volume is presented. This method uses two orthogonal 2D image projections, which are both parallel to the needle direction and intersect on the line of the needle tip artifact. Using a cropped image volume (from priori knowledge) the needle is segmented from the 2D images using a fixed threshold. In [17] the same authors delineated a needle from a 2D TRUS image using an adaptive threshold and Hough transforms. The two techniques presented in [15] and [17] are combined in [16] to increase the robustness of the algorithm.

As part of a robotic needle guidance system, a method to delineate a needle artifact from US images is briefly presented in [27]. A Hough transform is used to find the dominating line representing the direction of the needle, however the details of the segmentation method are not given. The end point is found by searching for groups of unconnected pixels.

From these works, it is clear that automating needle delineation is a difficult. There is support for using a median filter to reduce image noise and an initial estimate of the needle location to reduce processing time.

3.2 Methods

Figure 3.1 describes the method used to find the needle tip artifact in TRUS. A search for a clustered change in intensity between sequential frames is done in a cropped region of the image centered at the expected needle tip location (which is known from the preoperative plan). This search returns frames which may contain the needle tip artifact immediately prior to the needle being retracted and an approximation of the centroid of these needle tip artifacts in each frames. Next, the centroid of the artifact is more accurately computed using an adaptive thresholding method. The location of the centroid is displayed on the TRUS image so the radiation oncologist can confirm the needle tip has been correctly located. The radiation oncologist can manually select another location as the needle tip, overriding the automatically found needle tip.

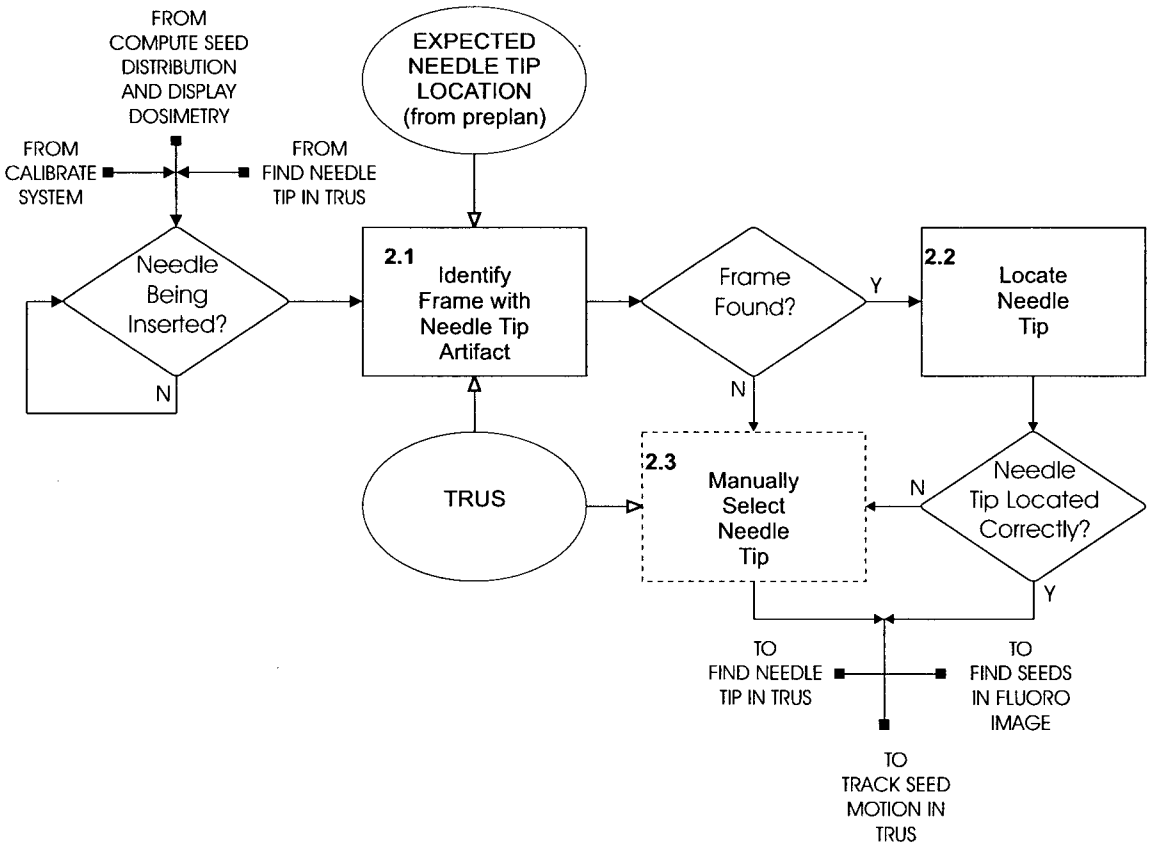

Figure 3.1: A flow chart of Block 2 of Figure 1.6 showing our approach for finding a needle tip in TRUS

3.2.1 Identifying the Frame with the Needle Tip Artifact

To accurately determine the coordinate of the needle tip the frame containing the needle tip artifact immediately prior to the needle being retracted must be determined. There are two items of a priori knowledge that help automate this process, but also several factors contributing to noise.

The expected needle tip location is known from the preplan. Through observation of the clinical data presented in this work, and in agreement with two practicing radiation oncologist, the needle tip artifact appears in the TRUS image within 2.5 mm of the expected location of the needle tip for the majority of the needles inserted. Using this information the frames are cropped to localize the search and reduce processing time.

The second item of a priori information is the time of the needle retraction. Although several possible automated options to determine when the needle has been retracted exist, such as a video camera or a variety of sensors, in the system presented here this is done manually.

The noise components include US speckle, patient and prostate motion, TRUS probe motion, and rectal gas. Identifying the frame immediately prior to the needle retraction is complicated by multiple needle tip artifacts that occur as the radiation oncologist positions the needle. Through a sequence of filtering and imposing thresholds the noise components can be reduced.

3.2.1.1 Methods

Algorithm 2 presents our approach to use the a priori knowledge and reduce the image noise to find the frame containing the needle tip just prior to the retraction.

After the user indicates the needle has been retracted, the previous N frames, from F_1 to F_N, are acquired for processing. This frames are cropped to the region expected to contain the needle tip artifact.

Next, a median filter is applied to each cropped image to remove US speckle noise. Speckle distribution is highly non-linear. The median filter is more robust than a mean filter because a single very unrepresentative pixel in a neighborhood will not affect the median value. Since the median value must be the value of one of the pixels in the neighborhood, the median filter does not create new unrealistic pixel values when the filter straddles an edge. Therefore, the median filter can preserve sharp edges while removing salt-and-pepper speckles.

The basic idea of Algorithm 2 is to detect intensity differences between sequential frames in the

region of the expected needle tip. To achieve this the algorithm takes the difference, F_D, between every k frames:

$$F_D = F_{N-(i-1)*k} - F_{N-i*k}, \qquad 1 < i < floor(N/k). \tag{3.1}$$

Figures 3.2a and 3.2b show two sequential frames. Frame $F_{N-(i-1)*k}$ does not have a needle tip artifact while Frame F_{N-i*k} does, the resulting difference image, with $k = 10$, is shown as Figure 3.2c.

This method works well assuming the TRUS probe does not move with respect to the anatomy. If the TRUS probe is translated in the z-direction (for example, to image another slice of the prostate), the patient or prostate moves, or the stage holding the TRUS probe is adjusted there will be a large change between sequential frames. Fortunately, a significant portion of F_D will appear as high intensity. By computing the mean intensity value of F_D large changes (i.e. greater than $T_{max\mu}$) between frames can be detected and F_D is ignored.

Figure 3.2c demonstrates that the needle tip artifact appears clearly in the difference image, but there is still some low intensity noise resulting from small changes in intensity between sequential frames. Fortunately, the needle tip artifact causes a large clustered change in intensity, so applying a fixed intensity threshold to F_D allows potential needle tip artifacts to be identified. The result of applying this thresholding technique to Figure 3.2c is shown in Figure 3.2d.

Even after applying a threshold some non-artifact pixels still appear in the binary image (as observed in Figure 3.2d). Therefore, a connected pixel algorithm is applied to find the clusters of

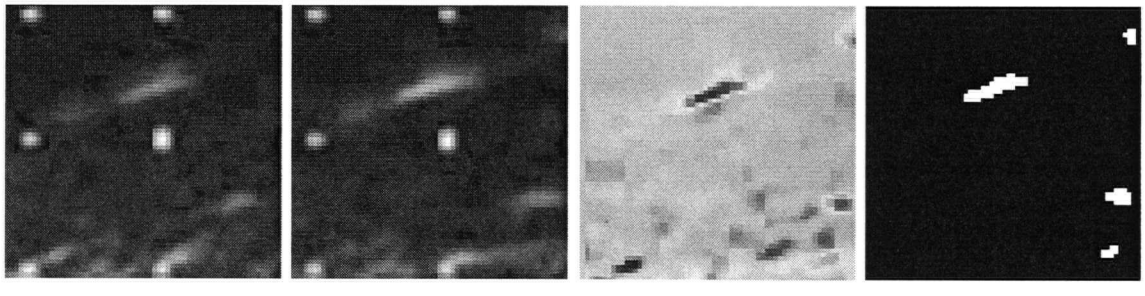

(a) (b) (c) (d)

Figure 3.2: TRUS images cropped to the region expected to contain a needle tip artifact, where (a) is frame 1 and (b) at frame 10. (c) The difference image resulting from the subtraction of (b) from (a), and (d) is a binary image of (c).

white pixels. These clusters are filtered based on size to identify potential needle tip artifacts.

To correctly position a needle radiation oncologists often insert and retract the needle several times, therefore the needle tip artifact appears and disappears from the TRUS image. The frame containing a needle tip artifact closest to the time of the needle retraction is used to determine the coordinate of the needle tip.

As shown in Figure 3.1, if no needle tip artifact is detected the next step in localizing the needle tip is bypassed and the artifact is manually selected by the radiation oncologist.

Algorithm 2 The algorithm to identify the frame with the needle tip artifact

Input: TRUS video
The expected location of the needle tip

Signal Needle has been Retracted
Get Previous N Frames
Crop Frames
Apply Median Filter
Compute Difference Between Sequential Frames
if Mean Difference $\leq T_{max\mu}$ **then**
  Create a Binary Image using a Fixed Threshold
  Look for Clusters of White Pixels
  Filter Clusters Based on Size
  Check for Repeated Artifacts
end if

Output: The TRUS frame containing the needle tip artifact
The approximate centroid of the needle tip artifact

3.2.2 Locating the Centroid of the Needle Tip

The metal of the needle acts as a specular reflector because of the significant difference in acoustic impedance between the needle and the soft tissue of the prostate. Therefore, needle tip artifacts appear as clusters of high intensity pixels in the TRUS images [18]. From observations in a phantom and clinical data, the shape and location of the artifact is related to the angle of the bevel on the needle tip. The bevel acts as a parabolic reflector. When the inside surface of the bevel is facing the source of ultrasound waves, the sounds waves are reflected directly back to the transducer of the probe create a bright intensity artifact in the TRUS image. When the angle between the normal of

the bevel and the direction of propagation of the sound waves is 90 degrees the sounds waves are reflected away from the transducer. Lastly, when the tip is not in the image, but the entire shaft is present there are two regions of high intensity appear in the image.

Through experimentation it was found that the center of the needle tip is the desired point because it corresponds to the center of the needle tip shaft and thus the center of the seeds being implanted.

Locating the needle tip from the artifact involves finding the coordinates of the center of the needle tip artifact. The z-coordinate of the needle tip is known from the preplan or the position of the TRUS probe. The image background is known from the frame $F_{N-(i-1)*k}$. US speckle introduces noise into the system, but knowing the frame with the needle tip artifact minimizes the contribution of the other noise components mentioned in the previous section. Our approach for identifying the centroid of the needle tip artifact is given in Algorithm 3.

Given F_D, a binary image is created using an adaptive thresholding technique. The mean intensity of the image, μ_{bk}, is computed from which a threshold is defined:

$$T_{base} = \alpha * \mu_{bk}, \tag{3.2}$$

where α is a constant between 0 and 1. Next, the pixels in F_D are sorted by intensity. Then an image, I_r, is created by leaving the $N_{artifact}$ highest intensity pixels that are also greater than T_{base} unchanged, but assigning all other pixels a value of 0. Here, $N_{artifact}$ is the maximum size of most needle tip artifacts determined by observation and experimentation.

To smooth the edges a median filter is applied to I_r. Lastly, the centroid of the artifact is found by computing an average weighted by the intensity of the non-zero pixels.

Algorithm 3 The algorithm to locating centroid of the needle tip

Input:F_D - a TRUS image with a needle tip artifact

Create an Image from F_D using an Adaptive Threshold
Apply Median Filter
Compute the Centroid of Non-Zero Pixels

Output: The coordinates of the centroid of the needle tip artifact.

3.3 Results

To demonstrate the algorithm can correctly locate needle tip artifacts in TRUS clinical data collected during implants was processed post-operatively. The US frames were collected at 30 frames per second (FPS) from the video output of the US machine using an Adaptec AVC-2210 video capture device. The video was digitized in MPEG file format and later compressed using the X-DIV codex to an AVI file format. The procedure was recorded with a video camera so the position of the TRUS probe and the time of each needle retraction times are known.

The method presented in this chapter is tested on twenty-two needles inserted during one procedure. The location of the needle tip manually identified. The location found using our automated method is compared to the manually selected location. The parameters used in the algorithm are given in Table 3.1.

For twenty-two needle tips the mean Euclidean distance between the manually and automatically detected needle tips was 3.7 mm. The mean absolute difference in the y-direction was 1.9 mm. Of the twenty-two needle tips, five would have needed to be manually relocated, either because the wrong frame was selected or the noise resulted in the wrong centroid being computed.

The two reasons for high error were the needle tip not appearing as a bright high intensity artifact or the artifact only appears when there significant motion in the image, therefore the frame is ignored.

3.4 Conclusion

A new method to locate a needle tip in TRUS has been presented. To the best of our knowledge this is the first work reported to localize a needle tip in US when the needle direction is orthogonal to the to the US image. Our method has been shown to work on noisy clinical data, however some needle tips which appear in noisy regions of the image must be manually selected. There are a lot of parameters to be set using our method. Many of these have been determined experimentally, however optimizing these is an area for future work.

Table 3.1: Parameters used to demonstrate our needle tip finding algorithm

Parameter	Value
N	90
preprocessing median filter size	3 x 3 pixels
k	10
$T_{max\mu}$	20
T_{diff}	25
Max cluster size	400 pixels
Min cluster size	40 pixels
α	0.9
$N_{artifact}$	100
postprocessing median filter size	5 x 5 pixels

Chapter 4

Locating Seeds in Fluoroscopic Images

The (x,z)-coordinates of the seeds must be determined in a fluoroscopic image so the seed position can be back-projected to the base frame to compute the 3D seed distribution. For our RTD system, most of the seed artifacts must be automatically located to ensure the system is real-time and to minimize changes to the current protocol for the prostate brachytherapy.

As discussed in Chapter 2, seeds appear as dark artifacts in fluoroscopic images because they are composed of metals which attenuate X-ray energy more than the surrounding tissues. Figure 4.1 is a fluoroscopic image of implanted seeds. Automatically delineating the seeds from a fluoroscopic image is complicated by background image noise and overlapping seed artifacts, where two seeds appear as one artifact in the fluoroscopic image.

Furthermore, seeds can move between fluoroscopic images, so the system must be able to update the coordinates of the previously located seeds. To explain this, two terms must be defined: *old seeds* and *new seeds*. If a sequence of n fluoroscopic images are taken, I_o at time t_o to I_n at time t_n, then all the seeds imaged in I_{n-1} are referred to as old seeds. Those seeds implanted between I_{n-1} and I_n will appear only in I_n so they are referred to as new seeds. Fortunately, the problem of updating the coordinates of the old seeds is simplified by knowing the (x,z)-coordinate of the seeds in the fluoroscopic image I_{n-1}.

Because the (x,z)-coordinates of the seeds are used to compute the y-coordinate of the seeds based on a needle path, every seed must be associated with a needle path. Figure 4.1 illustrates the complexity of associating a seed with a needle when, at the end of a procedure, 80 to 150 seeds are present in the image. However, this problem is simplified by knowing the expected seed locations

from the preoperative plan and the needle path.

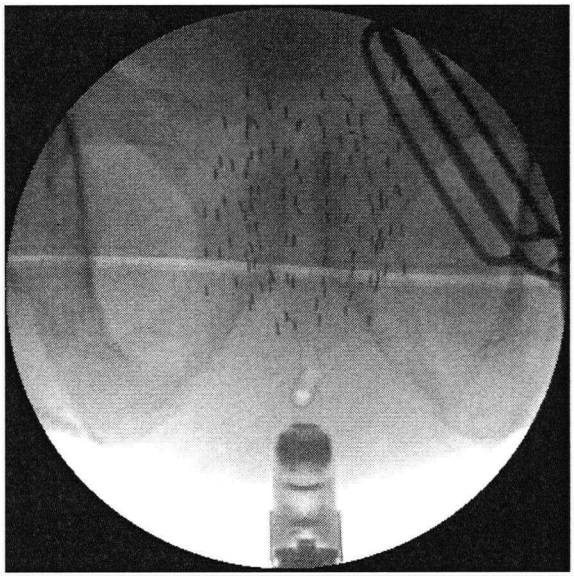

Figure 4.1: An example of a fluoroscopic image of implanted seeds

4.1 Prior Work

Several approaches for automated seed delineation in fluoroscopic images are presented in the literature. The simplest being manually locating the seeds in digitized radiographs as reported in early approaches for computing postoperative dosimetry. [2], [45], [5], [1], [47]

In [6] a multiscale geometric statistical pattern recognition (MGSPR) segmentation method for segmenting seeds from digitized radiographs is proposed. This approach requires a training set to describe seed artifacts. This training set is applied to an image with seeds at unknown locations to determine the location and orientation of the seeds in the image. However, the potential of this technique is questionable because it was only tested on computer-simulated images.

A more developed method is presented in [57]. The noise in the image is reduced as follows:

$$v(x, y) = log(u(x, y) + 1) \tag{4.1}$$

where $u(x, y)$ is the original fluoroscopic image and $v(x, y)$ is the noise-reduced image. Next, the image is normalized as follows:

$$w(x, y) = \frac{v(x, y) - v_{min}(x, y)}{v_{max}(x, y) - v_{min}(x, y)} 255 + 0.5, \tag{4.2}$$

where $w(x, y)$ is the normalized image and, $v_{min}(x, y)$ and $v_{max}(x, y)$ are the minimum and maximum intensity values of the image $v(x, y)$, respectively. The background is removed using a top-hat opening gray-scale morphological filter (morphological operators are described in [9] and the Appendix of [53]). A threshold is set dynamically using an entropy-based method and the seeds are segmented from the image. The segmented artifacts are labelled using a simply recursive labelling technique based on connected pixels. The resulting artifacts are analyzed as particles to distinguish noise from valid seed artifacts and identify clusters of seed artifacts.

The system presented in [53] first inverts the fluoroscopic image of the seeds and fiducial markers. Then, a gray-scale top-hat opening algorithm is applied to suppress the background noise. Next, a threshold is dynamically set based on the average brightness of the image and a binary image is produced. The seeds are segmented from clusters using a particle analysis algorithm which considers perimeter, eccentricity and moment invariants.

The seed segmentation algorithm used in the RTD system reported in [23] and [32] is explained in more detail in [10]. First, the image background is estimated with the morphological opening function followed by gray-scale reconstruction. The resulting image still contains some unwanted structures in the background, so a morphological estimate of the background is subtracted from the image (a background image is acquired at the beginning of the procedure). The result is an image with only seeds, needles and a low frequency background. Then, a the threshold is dynamically set using discriminant analysis to to delineate the seeds and needle tip artifacts. The end points of the seeds are found using a connected component analysis and the binary image is analyzed through template matching. The algorithm finds 59 to 60 seeds when 61 seed artifacts are present in the image. The remaining seeds are located manually.

The majority of these works use some combination of morphological operators and thresholding to locate and label seed artifacts. Morphological operators take advantage of the distinct and consistent shape of the seed artifacts, while thresholding takes advantage of the intensity contrast between the seed artifact and the image background. However, these works do not make use of a

priori information about the expected seed location and as a result have difficult matching seeds between multiple fluoroscopic images. [32] Although these methods have been verified in phantoms, they have not been extensively tested on clinical data. Therefore, problems such as artifact exclusion and merging (two or more seeds appear as one artifact) have not been fully explored. Morphological operators and thresholding, combined with a priori knowledge of the expected seed distribution, will be needed for our approach.

4.2 Methods

Figure 4.2 describes our method to find the (x,z)-coordinates of seeds in a fluoroscopic image. A fluoroscopic image of the coronal plane of the patient is acquired. Because the seeds are distinctly different than the image background a thresholding and morphological operators are used to identify potential seed artifacts in the image (morphological operators are described in [9] and the Appendix of [53]). To simplify the search for new seeds, the old seeds are first identified in the image. The coordinates of the old seeds are updated using their coordinates in the previous fluoroscopic image (i.e. I_{n-1}). The new seeds are identified and matched to a needle using information from the preoperative plan and the needle path. The coordinates of all the seeds are displayed and confirmed by the radiation oncologist. The seed locations can be manually updated, if necessary. Finally the coordinates of the seeds are dewarped using the method presented in Section 2.4.

4.2.1 Identifying Possible Seed Artifacts

The algorithm for identifying seed artifacts is given as Algorithm 4. The image, I_n is cropped to a region of interest (ROI) using the expected seed locations to save computation time. A median filter is applied to the image to reduce some of the background noise and the image is inverted.

Although the seed artifacts appear as significantly darker artifacts than their surrounding tissue, a simple thresholding algorithm cannot be used to create a binary image because as is evident in Figure 4.3a the background of the image is not consistent. The operating table is in the background of the top half of the image and not the bottom and the anatomy of the patient varies within the image as well as between patients. However, the seed artifacts are clearly distinguishable, so locally setting the threshold effectively creates a binary image, I_b, differentiating the seed artifacts from the background. The local threshold, T_I, is set between the mean intensity of the region and the

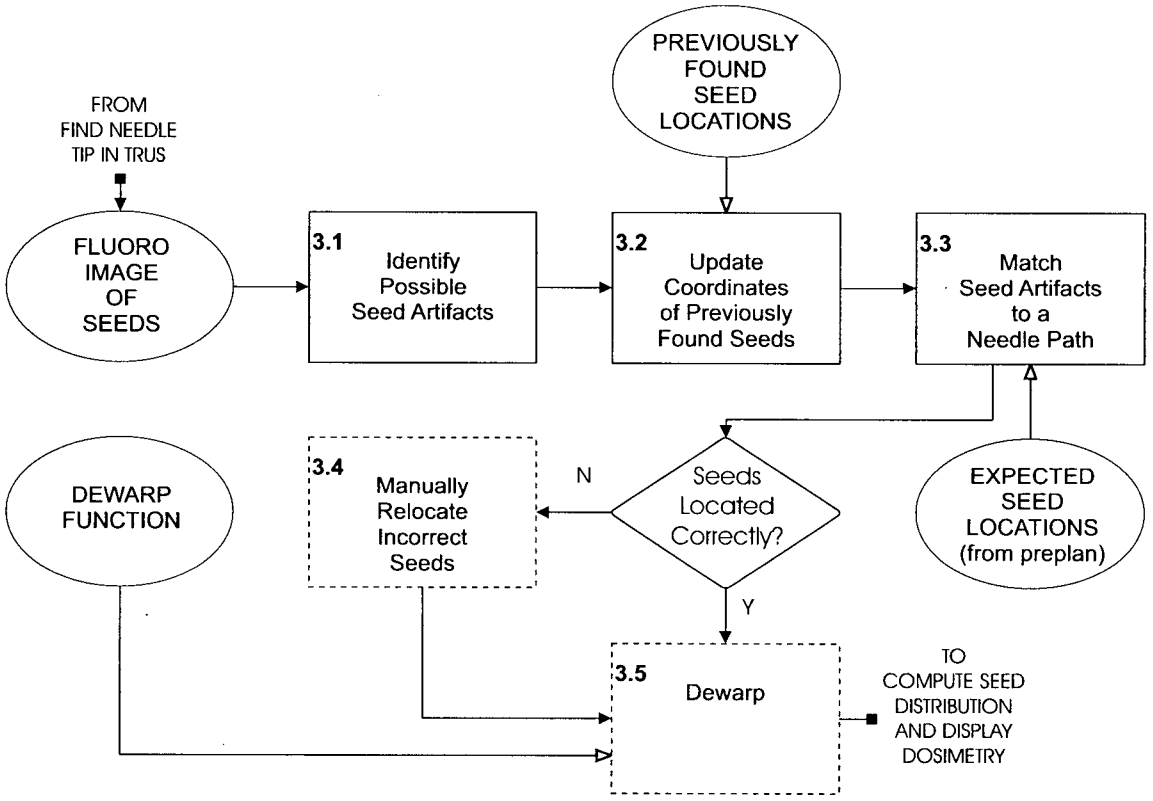

Figure 4.2: A flow chart of Block 3 of Figure 1.6 showing our approach for locating seeds in fluoroscopic images.

maximum pixel intensity (the image has been inverted so the seed artifacts are now a maximum). The local background is defined as a region of 9 x 5 pixels about the pixel of interest. Figure 4.3b shows the resulting binary image, I_b.

The sensitivity of the thresholding algorithm is controlled by the parameter α. Increasing α reduces the noise in the binary image, but increases the risk of eliminating seed artifacts. The morphological opening function can be used to take advantage of the known shape of the seed artifact. The opening function produces another binary image from two inputs: the binary image and a structure element, SE. The structure is an approximate to the shape of the seeds, which is 4 pixels long by 2 pixels wide. The results of applying the opening function to Figure 4.3b are shown in Figure 4.3c.

Once a binary image is created the connected components must be labelled. This is achieved by simple search:

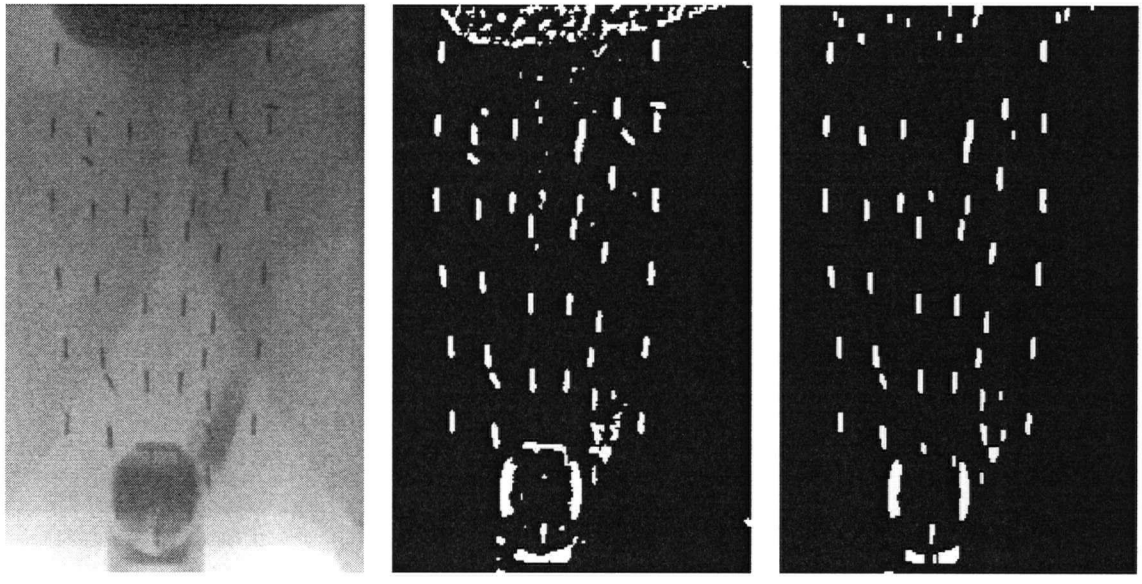

(a) (b) (c)

Figure 4.3: (a) A fluoroscopic image of the seeds, (b) a binary image of (a), and (c) an opened image of (b)

1. Starting in the top-left corner of I_b, search for the first white pixel.
2. When a white pixel is found, check the eight neighboring pixels labelling all white pixels.
3. Repeat step (2) until no more white pixels are found.
4. Continue searching I_b for white unlabelled pixels.

As demonstrated in Figure 4.3c, the TRUS probe and clamp appear as artifacts in the image, along with some inherent noise. These artifacts are removed as candidate seed artifacts by restricting the size of the clusters to be greater than C_{min} and less than C_{max}.

The problem of seed artifact identification using only projection images is complicated by is the possibility of overlapping seeds which merge to appear as one cluster of connected pixels. [57], [10], [53] This problem is overcome by doing a particle analysis. Although, more advanced particle analysis methods are used in [57], [10] and [53], where both the dimensions and orientation of the artifact are considered, only the dimensions of the clusters are considered here. This allows merged artifacts to be identified as two or more artifacts if the length or width of the artifact

exceeds L_{seed} or W_{seed}, respectively. Lastly the centroid of each seed artifact is to computed as follows:

$$(x_c, z_c) = \left(\frac{(x_{max} - x_{min})}{floor((x_{max} - x_{min})/W_{seed}) + 1}, \frac{(z_{max} - z_{min})}{floor((z_{max} - z_{min})/L_{seed}) + 1} \right), \tag{4.3}$$

where (x_c, z_c) are the (x,z)-coordinates of centroid of each of the possible seed artifacts and x_{max}, x_{min}, z_{max}, and z_{min} denote the range of the cluster of connected pixels. Figure 4.4 shows the coordinates of the seed artifacts shown as yellow x's.

Algorithm 4 An algorithm to identify possible seed artifacts in a fluoroscopic image

Input: I_n - a fluoroscopic image of the implanted seeds

I_n = Crop(I_n)
Apply median filter
I_{max} = max(I_n)
I_n = I_{max} - I_n
for y = 1 to number of rows in I_n **do**
  for x = 1 to number of columns in I_n **do**

$$\mu_v = \frac{\sum_{i=-R}^{R} \sum_{j=-S}^{S} I_n(x+i, y+j)}{(2R+1)*(2S+1)}$$

    $T_I = \mu_v + \alpha(I_{max} - \mu_v)$
    if $I_n(x, y) \geq T_I$ **then**
      $I_b(x, y) = 1$
    else
      $I_b(x, y) = 0$
    end if
  end for
end for
Apply open(I_b, SE) {open() is a morphological operation}
Identify clusters
Do particle analysis
Compute the centroid of each possible seed artifact

Output: The (x,z)-coordinates of the centroid of each seed artifact

4.2.2 Updating the Coordinates of Previously Found Seeds

As noted [38], [12], [48] and [44], the seeds can move intraoperatively, so the (x,z)-coordinates of the seeds must be updated after each fluoroscopic image. Furthermore, by identifying the old seeds

Figure 4.4: The coordinates of the seed artifacts (marked as yellow x's) found in the fluoroscopic image shown in Figure 4.3a.

in the fluoroscopic image I_n, the search for new seeds is simplified.

Given the (x,z)-coordinates of the seed artifacts are known from the image I_{n-1}, the candidate seed artifacts found using Algorithm 4 within a distance r_o of the old seed artifact are identified. Then, these possible seed artifacts are associated with each needle by minimizing the error terms given in Equations 4.4 and 4.5 in the next section. After a seed artifact has been associated with a needle, it is removed as a candidate seed artifact for other needles to simplify the search for additional seeds.

Interestingly, tests on sequences of fluoroscopic images show intraoperative seed motion cannot be characterized as an affine transform in the (x,z)-plane. It is possible that this motion can be characterized as a combination of rotating, swelling and shifting in 3D, but an extensive classifying of intraoperative seed motion is left as possible future work.

4.2.3 Matching Seed Artifacts to a Needle Path

Because the needle path is used to determine the y-coordinate of the seeds, each seed artifact must be associated with a needle. Fortunately, the seeds lie roughly on the predicted needle path and the seed spacing is known from the preoperative plan. Therefore, this information can be incorporated

into a model to predict the seed locations for each needle, and hence, select the seed artifacts for a given needle.

In Chapter 5 a needle path for each needle is determined from the location of the needle tip and the entry point of the needle. By projecting this needle path to the fluoroscopic image and from the known seed spacing the expected locations of the seeds are predicted. Interestingly, modelling the needle path as a line more closely predicts the expected seed locations than a second-order curve for the majority of needles.

Although the seed locations in the fluoroscopic image can be predicted quite accurately, one source of error is introduced through intraoperative seed motion between the time of the needle insertion and the acquisition of the fluoroscopic image. Secondly, some needles are inserted slightly more superiorly than required by the preoperative plan. And lastly, the needle tip may not accurately localized in TRUS. To compensate for these errors a search algorithm for potential seeds is employed. A radius of r_o centered at the predicted location of each seed artifact is searched for potential seed artifacts to find combinations of seed artifacts that could be associated with a given needle path.

Now that the potential seed artifacts for a given needle have been identified the correct combination of seeds must be found. To do this a cost function is evaluated for all possible combinations of the potential seed artifacts identified in the search for potential seed artifacts. The cost function models both the distance from the predicted seed artifacts to the potential seed artifacts and the spacing of the seeds as springs.

The first part of the cost function is as follows:

$$E_s = \sum_{i=1}^{n} (0.5 \cdot K_{long} \cdot (\zeta_i - \zeta_{i-1} - \Delta_{seed})^2 + 0.5 \cdot K_{lat} \cdot (\xi_i - \xi_{i-1})^2). \tag{4.4}$$

The first term of Equation 4.4 computes the energy between the seeds in the z-direction. Here, the Δ_{seed} is seed spacing required by the preoperative plan, which is the equilibrium position of the spring, ζ_i is the z-coordinate of the i^{th} potential seed artifact, and K_{long} is the spring constant. The second term accounts for seeds deviating from a straight needle path. Here, the equilibrium position of the combination of seeds is zero, ξ_i is the x-coordinate of the i^{th} potential seed artifact, and K_{lat} is the spring constant.

An additional cost is added to each combination of seeds based on the distance from the most

superior seed to the needle tip. The x-coordinate of the needle tip is accurately known from TRUS, however from observations of clinical images the z-coordinate of the needle tip varies. Therefore, a term is added to the cost function to pull the x-coordinate of the most superior seed artifact to the location of the projected needle tip:

$$E = E_s + 0.5 \cdot K_{offset} \cdot (x_o - \xi_o)^2. \tag{4.5}$$

Here x_o and ξ_o are the x-coordinates of needle tip and the most superior potential seed artifact, respectively, and K_{offset} is the spring constant.

The combination of seed artifacts that minimizes the error term, E, is selected at the combination of seed artifacts for a given needle. These seed artifacts are removed from candidate seed artifacts to help simplify the search for additional seed artifacts in the fluoroscopic image.

The values of r_o, K_{long}, K_{lat} and K_{offset} were determined through experimentation. As presented in the next section this method of matching seed artifacts to needles works in clinical data, but some manually intervention is required. Loose seeds[1] do not always line up parallel to the z-axis and have inconsistent spacing. Therefore, they are difficult to segment from the image and match to a needle. Therefore, each seed is searched for individually leaving only the second term of Equations 4.5 contributing to the error term.

4.3 Results

It is difficult to test the accuracy with which the seeds are located because the true location of the seeds in clinical data is not known and phantoms do not properly create the noise observed in clinical images. In Chapter 6 the final seed distribution determined by our RTD system is compared to a known seed distribution in a phantom and the seed distribution found using postoperative CT images in clinical data. However, these results are coupled with error introduced through registration, dewarping and identifying the needle tip. Therefore, our method is validated by plotting the coordinates of the seed artifacts found in clinical data on the fluoroscopic image and manually verifying the seed artifacts for each needle are correct. A similar validation approach is used in [53] and [56], where the seeds determined using their approach for RTD are projected to fluoroscopic

[1]The two types of seeds implanted at the VCC are described in the introduction of Chapter 1.

images of the implant seeds. The error between the projected seed location and the seed artifact in the fluoroscopic image is reported.

The TRUS and fluoroscopic images obtained from an implant were processed using our approach to determine RTD (Chapter 6 presents the details of data collection). The TRUS and fluoroscopic images were registered and the needle tip for each needle was identified using TRUS. After each row of needles, the seed artifacts are segmented from a fluoroscopic image. The old seeds are identified and their locations updated, and then, new seeds are identified for each needle. The coordinates of the seed artifacts are plotted on the fluoroscopic image for each needle. Seeds artifacts found to be misclassified are recorded as an error and manually relocated to the correct seed artifact, as indicated in Step 3.4 of Figure 4.2. Table 4.1 gives the values of the parameters used in this test.

Table 4.1: The parameters used to locate and track seed artifacts in fluoroscopic images.

Parameter	Value
R	4 pixels
S	8 pixels
α	0.09
SE	4 x 2 pixels
C_{max}	100 pixels
C_{min}	8 pixels
L_{seed}	15 pixels
W_{seed}	5 pixels
K_{long}	1000
K_{lat}	60
K_{top}	10
r_o	25 pixels
median filter size	3 x 3 pixels

Out of the 100 new seeds delineated in the images and associated with needles, 73 were found to be correct. The majority of missed new seeds occur in the last fluoroscopic image when the seed artifacts were very clustered (see Figure 4.5). In the prior images the two reasons for missed seed artifacts were exclusion by the TRUS probe or the seeds were deposited further in the negative z-direction than indicated by the preoperative plan. The first problem can be easily solved by

backing the probe up further before acquiring fluoroscopic images and the second is a consequence of the procedure where manual intervention will be required.

Of the 238 old seed artifacts tracked between sequential images, 211 seed artifacts were cor-

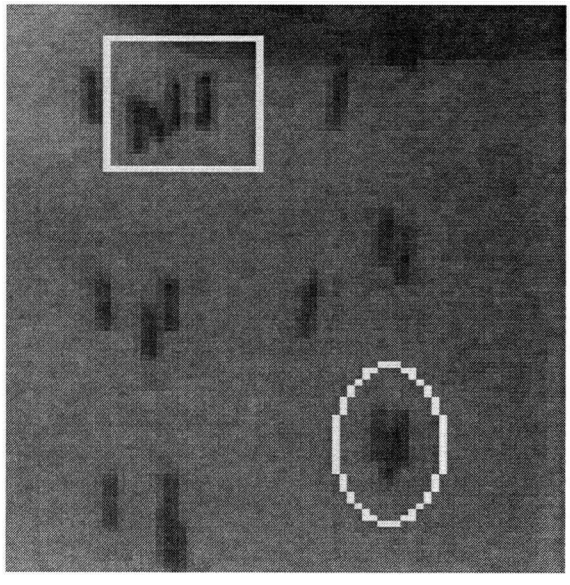

Figure 4.5: A fluoroscopic image showing seed artifacts merging (enclosed by the yellow rectangle) and partial occlusion (enclosed by the yellow oval).

rectly identified and assigned to the correct needle. Again, the majority of the errors occurred when the number of artifacts in the image increased in the last fluoroscopic image. It was noted that the loose seeds tended to move a lot between sequential fluoroscopic images. However, for seeds incased in RAPID Strand the majority of the seed motion was observed between the first image of the seeds (I_n) and the next fluoroscopic image (I_{n+1}). In the fluoroscopic images that followed little seed motion was noted simplifying the seed artifact tracking.

4.4 Conclusion

This chapter presents a method to locate and match seed artifacts to a needle path. Our approach is tested on one case of clinical data.

As shown in Figure 4.4, the seed artifacts, with the exception of loose seeds, are identified quite well using previously published methods. Loose seeds are not consistently delineated if they rotate

about the x or y-axis. Rotation about the y-axis causes the seed artifact to be eliminated by the opening function, while rotation about the x-axis causes the seed artifact to be too small to be detected. Figure 4.4 does show some false positives resulting from the TRUS probe and penis clamp artifacts being present in the image. In practice the TRUS probe should be further retracted and the penis clamp moved to eliminate this problem.

This chapter also presents, to the best of our knowledge, the first attempt to automatically match seed artifacts to a needle path. The majority of the errors observed occurred near the end of the procedure when the seed artifacts become clustered resulting in seed artifacts merging or being excluded (see Figure 4.5). Further refinement of the parameters of the cost function given as Equation 4.5 may improve the accuracy of our approach, but this is left as an area of future work.

Our approach for updating the location of the seed artifacts in sequential fluoroscopic images is quite promising. The majority of the misclassified seed artifacts result from loose seeds, which tend to move significantly more than RAPID Strand seeds. Reporting intraoperative seed motion from these fluoroscopic images may be an area of further research of interest to the medical community.

Chapter 5

Computing Seed Distribution and Displaying Dosimetry

Once the (x,z)-coordinates of the seeds have been determined from a fluoroscopic image and back-projected to the base frame, the y-coordinate of each seed must be found to compute the 3D seed distribution. Next, the y-coordinate of the seeds must be tracked to account for intraoperative seed motion. The dose distribution (a.k.a. dosimetry) is computed based on the seed distribution. Lastly, to achieve interactive planning, the dosimetry must be displayed to the radiation oncologist.

5.1 Methods

Figure 5.1 describes our approach for computing the 3D seed distribution and displaying the dosimetry to the radiation oncologist. By knowing the entry point of the needle in the needle guide (from the preoperative plan) and coordinate of the needle tip, a needle path can be interpolated. Using the interpolated needle path and the (x,z)-coordinates of the seeds the y-coordinate of each seed is computed. Throughout the procedure the y-coordinate of the seeds is tracked using a correlation technique. The 3D seed distribution is used to compute dosimetry. Lastly, the dosimetry is displayed to the radiation oncologist by displaying both a color-coded dosimetry map and the corresponding TRUS image.

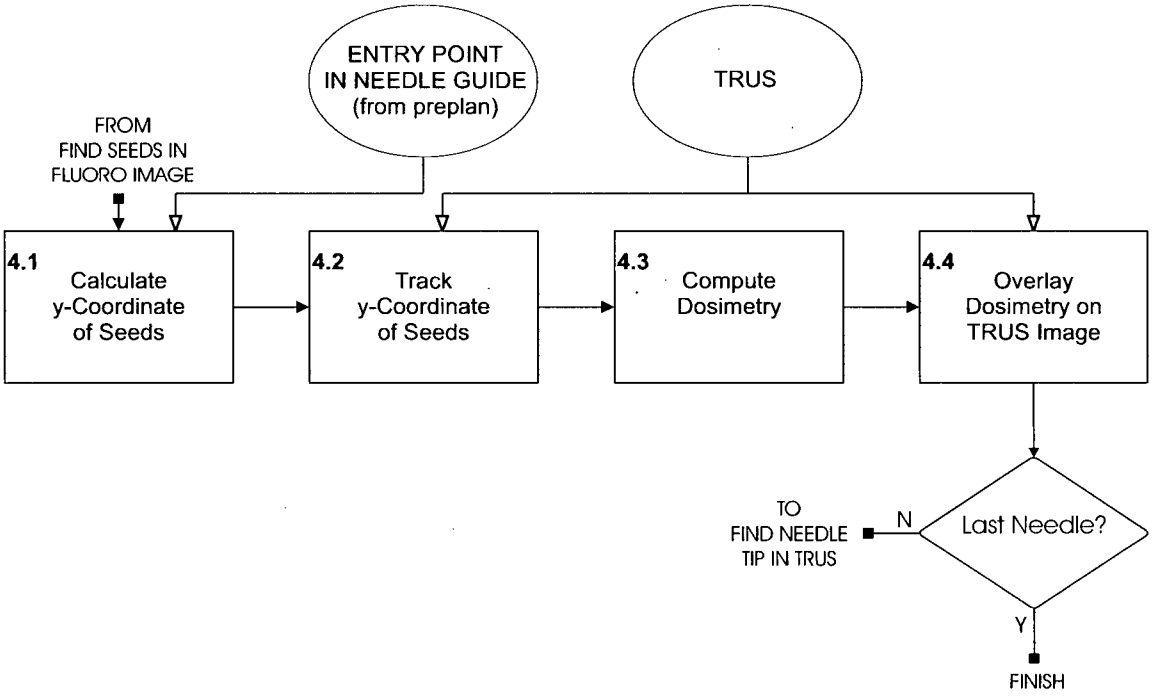

Figure 5.1: A flow chart of Block 4 of Figure 1.6 showing our approach for computing the seed distribution and displaying dosimetry.

5.1.1 Calculating the y-Coordinate of the Seeds

As shown in Figure 2.13a the resolution of the available fluoroscopic images is not sufficient to accurately determine the y-coordinates of seeds. And, B-mode TRUS cannot localize seeds because they do not appear reliably in the images [24]. However, using the needle tip artifact, which does appear reliably in TRUS images (see Chapter 3), and the known entry point of the needle from the preoperative plan, a needle path can be interpolated.

Referring to Section 4.2.3, both first-order and second-order needle paths were projected to the fluoroscopic image. For the majority of needles a first order needle-path more accurately predicted the location of seed artifacts. The large differences in stiffness between the needle and the soft tissue of the prostate could explain this observation. Although the needle bends under the force of the radiation oncologist's fingers, it returns to a linear path when this force is removed, which occurs before the needle is retracted and the seeds deposited. Therefore, a first-order path is also used for predicting the needle path.

Denoting the (x,y,z)-coordinates of the seeds as (x_s,y_s,z_s) the needle path can be expressed as

follows:

$$y_s = ax_s + bz_s + c, \tag{5.1}$$

where a and b are the slopes of the needle path in the (x,y) and (y,z)-planes, respectively. Using the two known points on the needle path, the coordinates of the hole in the needle guide used to insert the needle and the position of the needle tip, the value of these coefficients can be computed. Then, the value of c is computed by substituting the coordinate of the needle tip into Equation 5.1.

5.1.2 Tracking Seed Motion in TRUS

Intraoperative seed motion during prostate brachytherapy is well documented. Seed motion results from edema, patient motion and prostate shifting in response to forces applied during needle insertions [38], [12], [48], [44]. In our system, seed motion in the (x,z)-plane is tracked using sequential fluoroscopic images as presented in Section 4.2.2.

Because dosimetry is displayed with respect to the TRUS images, seed motion must be tracked with respect to the TRUS probe. There are two ways the seeds can move with respect to the TRUS probe: the prostates moves as mentioned above or the TRUS probe is translated. The later cases occurs if the radiation oncologist uses the fine adjustments on the stage shown in Figure 1.2 to adjust the position of the TRUS probe. The purpose of these small adjustments is to realign the intraoperative TRUS images to the preoperative TRUS images. In this section an approach to track both these sources of seed motion in the y-direction using TRUS is presented.

5.1.2.1 Prior Work

There has been a significant amount of work reported on tracking organ motion using various imaging modalities. However, only a very brief review specific to approaches which directly use image data from brightness-mode (B-mode) US is presented in this section.

In [55] blood flow is successfully tracked *in vivo* using a normalized cross-correlation coefficient method. A mask is cropped from an image and the normalized cross-correlation is computed between the mask and a region of interest (ROI) in another image. The location of the maximum cross-correlation coefficient is assumed to be the location of the mask in the second image. Similar work is reported in [7], except a sum of absolute difference (SAD) is used to compute the new location of the mask. A non-normalized time domain correlation-based algorithm is used in [58] as

a measure of similarity to track motion in phantoms.

These methods all measure the similarity between a mask and a sequential image expected to have similar artifacts and/or noise characteristics. Because TRUS images of the prostate have several distinct artifacts that appear in sequential image the same approach will be used here.

5.1.2.2 Methods

Algorithm 5 describes our approach to tracking seed motion using TRUS. The basis of our seed tracking algorithm is to correlate a mask from a TRUS image, denoted I_o, with a later frame, denoted I_n. In our current system masks are manually selected from I_o by either the radiation oncologist or a radiation therapist. Ideally, masks contain a bright artifact, such as a seed or blood trail or distinct features, such as the prostate boundary.

This seed tracking method uses a single transverse slice of the prostate. If the TRUS probe is translated in the z-direction to image a new slice, new masks must be selected. However, if the motion is minimal, the probe can be returned to the original slice and the seed tracking resumed. That being said, this method works best if the TRUS probe is *parked* at a consistent slice when not being used to image the prostate or guide a needle, in particular if the stage is adjusted to compensate for prostate motion. Using the same slice allows changes in the prostate position to be easy observed by comparing sequence images.

It may be possible to automate this step by either searching I_o for clusters of high intensity artifacts or unique features. Since the prostate boundary is known from the preplan volume study, it could be selected as a mask. However, automated mask selection and the selection of optimal masks is a complex problem beyond the scope of this thesis and will be dealt with in the future.

The goal of this step is to determine the location of the mask selected from I_o in the new frame I_n. This is accomplished by doing a normalized cross-correlation of the mask with a ROI in I_n, denoted I_{roi}. The mask, I_{mask}, consists of N x M pixels centered at (x_c^o, y_c^o), while I_{roi} is an $(N + 2S$ x $M + 2T)$ patch of pixels (R and S define the ROI in I_n) with the same centroid. The normalized cross-correlation coefficient of I_{mask} and I_{roi} is computed as follows:

$$\rho(m,n) = \frac{\sum_{i=1}^{M}\sum_{j=1}^{N}\left(I_{mask}(i,j) - \mu_{mask}\right)\cdot\left(I_{roi}(i+n,j+m) - \mu_{roi}\right)}{\sqrt{\sum_{i=1}^{M}\sum_{j=1}^{N}\left(I_{mask}(i,j) - \mu_{mask}\right)^2 \cdot \sum_{i=1}^{M}\sum_{j=1}^{N}\left(I_{roi}(i+n,j+m) - \mu_{mask}\right)^2}}, \quad (5.2)$$

where μ_{mask} and μ_{roi} are the mean intensity value of I_{mask} and I_{roi}, respectively.

The maximum correlation-coefficient in the matrix, $\rho(m,n)$, corresponds to the centroid, (x'_c, y'_c), of I_{mask} in I_n. Calculating the distance between (x^o_c, y^o_c) and (x'_c, y'_c) gives the distance the mask has move with respect to the TRUS probe. However, since the x-coordinate is already updated using sequential fluoroscopy images, only y^o_c and y'_c are used to update the y-coordinate of the seeds.

Once the motion of each of the masks is computed, the motion of each of the seeds in the y-direction is computed based on the distance from the seed to (x^o_c, y^o_c) as follows:

$$y'_s = \frac{\sum_{i=1}^{K} (y'_c(i) - y^o_c(i)) \sqrt{(y^o_s - y^o_c(i))^2 + (x^o_s - x^o_c(i))^2}}{\sum_{i=1}^{K} \sqrt{(y^o_s - y^o_c(i))^2 + (x^o_s - x^o_c(i))^2}}. \tag{5.3}$$

Here, y'_s is the new y-coordinate of the seed, K is the number of masks, i refers to the i^{th} mask, and x^o_s and y^o_s are the coordinates of the seed in I_n.

Algorithm 5 The algorithm to tracking the y-coordinate of the seeds.

Input: TRUS video

Find Artifacts to Track
Track Artifacts
Update the y-Coordinate of the Seeds

Output: The coordinates of the seeds.

5.1.2.3 Results

This seed tracking algorithm was tested on clinical data. During the procedure the height of the probe was adjusted, the frames immediately before and after the adjustment are shown as Figures 5.2a and 5.2b. The location of three distinct artifacts (see Figure 5.2c) was found in both the old and new frames by finding the centroid of the artifact using a thresholding technique. To define a gold standard, the motion of the centroid of these artifacts between the old and new frames (reported in the second column of Table 5.1) is defined as the *true motion* of the prostate. Two seeds or blood trail artifacts and the anterior boundary of the prostate were selected as masks (see Figure 5.2c). The motion detected by our algorithm (reported in the third column of Table 5.1) was

compared to the *true motion* of the three artifacts used to define the gold standard. The results in Table 5.1 show that seed motion can be intraoperatively tracked in TRUS with a high degree of accuracy.

Table 5.1: The results of tracking seed motion in clinical data using TRUS

Seed	Seed Motion in Image (mm)	Detected Seed Motion (mm)
1	−0.924	−0.947
2	−0.924	−0.912
3	−0.922	−0.995

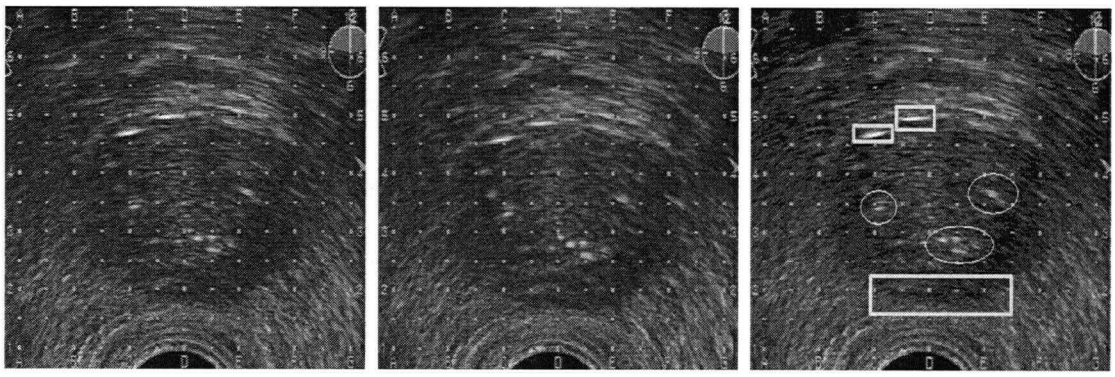

(a) (b) (c)

Figure 5.2: (a) The old frame, I_o, (b) the new frame, I_n (note seed motion between frames), and (c) the masks (enclosed in rectangles) and seeds (circled) used to show TRUS can be used to track seed motion in clinical data

5.1.3 Computing Dosimetry

The dose distribution resulting from the 3D seed distribution determined in the previous section must be computed to convey dosimetry information to the radiation oncologist.

The seeds used at the VCC are Amersham 6711 which contain the isotope Iodine-125. For the purposes of computing dosimetry the prostate space is divided in 2.5 mm^3 voxels. The center of the voxel is taken as the point of interest. The voxel size was selected at the suggestion of a radiation oncologist.

The dose rate calculation is based on the Report of Task Group Number 43 of the American Association of Physicists in Medicine [43]. A point source model is used here as seed orientation cannot be determined accurately enough to compute a more complicated model (as a line source model). Consistent with the recommendations in [43], the geometric center of a seed artifact is assumed to be the geometric center of the seed.

The dose model for each seed is defined as:

$$D(r) = \lambda^{-1} \cdot S_{Ko} \cdot \Lambda \cdot \frac{G_p(r)}{G_p(r_o)} \cdot g_p(r) \cdot \phi_{an}(r), \tag{5.4}$$

where:

- r is the distance, in centimeters, from the geometric center of a seed to the center of the voxel of interest, (x_v, y_v, z_v). Equation 5.4 is only defined for r greater than 0.05 cm. If r is less than $D(r = 0.05cm)$ is used to compute the dose contribution.
- r_o represents a reference point 1 cm from the center of the seed.
- λ is the decay constant, which is computed as follows:

$$\lambda = \frac{log(2)}{T_{\frac{1}{2}}}, \tag{5.5}$$

  where $T_{\frac{1}{2}}$ is the half-life of the seeds, which is 1425.6 hours for Amersham 6711 seeds.
- S_{Ko} is the initial air-kerma strength of a seed, measured as a unit of air-kerma strength, U. S_{Ko} is 0.424 U for seeds used at the VCC.
- Λ is the dose-rate constant in water, measured in $cGy \cdot h^{-1} \cdot U^{-1}$. Λ is reported to be 0.965 $cGy \cdot h^{-1} \cdot U^{-1}$ in [43] for Amersham 6711 seeds.
- $G_p(r)$ models the radioactivity as a function of r. For a point source:

$$G_p(r) = \frac{1}{r^2}. \tag{5.6}$$

- $g_p(r)$ is the radial dose function describing the dose rate at a distance r from a source relative to the dose rate at r_o. The numerical values of $g_p(r)$ for Amersham 6711 seeds are linearly interpolated from Table II of [43]. This term is dimensionless.

- $\phi_{an}(r)$ is the 1D anisotropy function. The numerical values of $\phi_{an}(r)$ for Amersham 6711 seeds are linearly interpolated from Table V of [43]. This term is dimensionless.

The total dose is determined by summing the dose contributions from each seed. A plot of the one-dimensional dosimetry resulting from seven seeds is given as Figure 5.3.

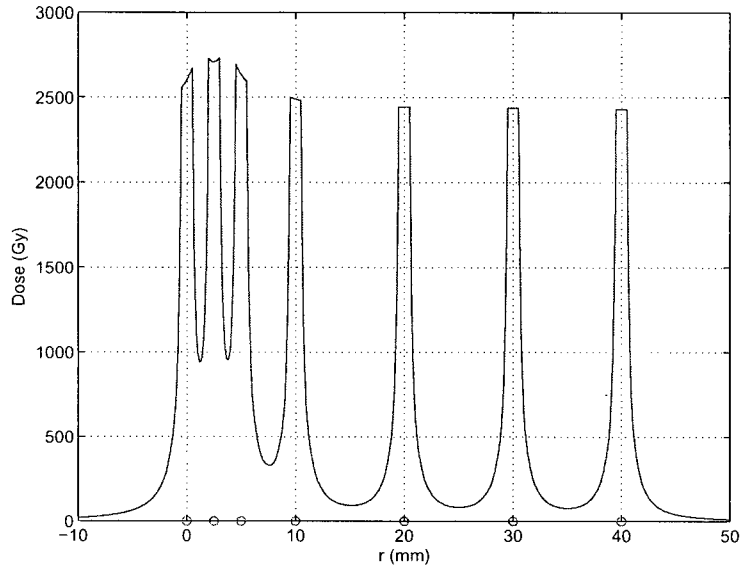

Figure 5.3: A 1D plot of dose versus seed position for seven seeds positioned at 0, 2.5, 5, 10, 20, 30, and 40 mm (shown as red circles)

5.1.4 Overlaying Dosimetry on TRUS Images

To allow radiation oncologists to do interactive planning the dosimetry resulting from the implanted seeds must be displayed with respect to the prostate. This allows for additional seeds to be inserted to compensate for under-dosed regions of the gland.

A transverse dosimetry map is displayed for each TRUS image, where the dosimetry map corresponds to a TRUS image. The dosimetry map displays the amplitude of the dose for the each voxel. A smoothing function is applied to smooth the dosimetry display between adjacent voxels. In order to remove the spikes introduced by the dosimetry computation (see Figure 5.3) the dose displayed is saturated at a threshold T_{sat} defined as:

$$T_{sat} = \mu_d + 3\theta_d, \tag{5.7}$$

where μ_d and θ_d are the mean and the standard deviation of the amplitude of the dosimetry, respectively. As future work, this color-coded map could designed to map colors to dose values which are clinical relevant.

Displaying the dosimetry and TRUS images adjacent to each other allows the radiation oncologist to register the dosimetry map to the TRUS image and modify the preoperative plan as needed. It would be ideal to overlay a semi-transparent color-coded dosimetry map over a TRUS image. As a step towards that, two images are displayed beside each other, one being the color-coded map and the other a TRUS image a particular slice of the prostate. Figure 5.4 shows four slices of the dose delivered to the prostate and the corresponding TRUS image.

5.2 Conclusions

A method to compute and track the y-coordinate of the implanted seeds motion has been presented. Once the 3D seed distribution is computed the resulting dosimetry and displayed to the radiation oncologist.

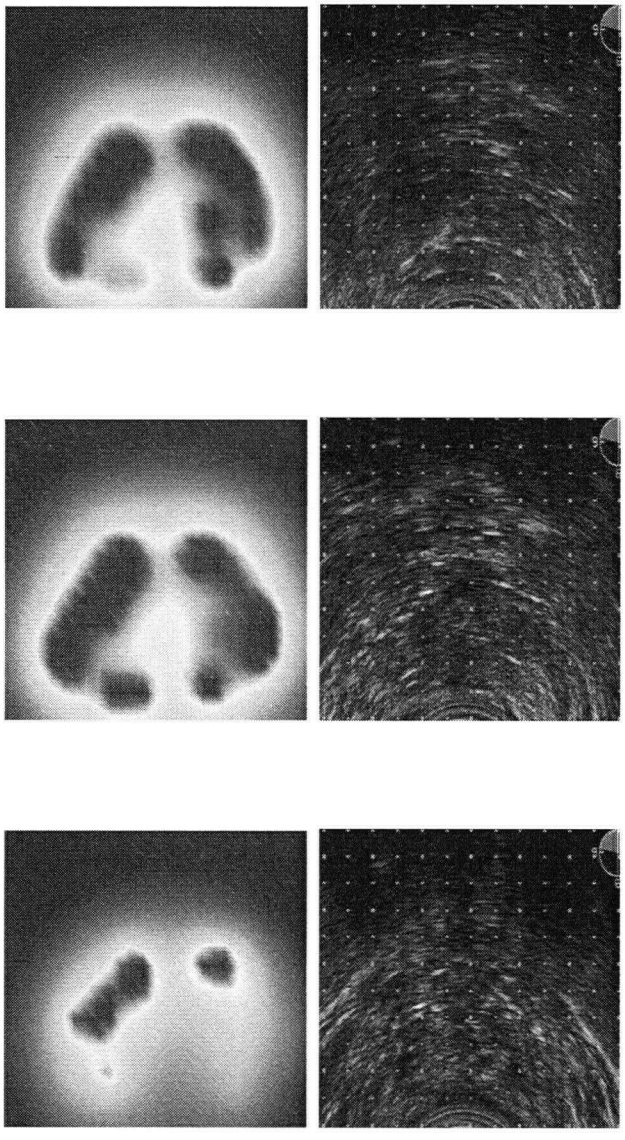

Figure 5.4: The images on the left show the the color-coded dosimetry for several slices of the prostate volume and the images on the right are the corresponding TRUS images.

Chapter 6

Results

In Chapter 2 the error in our registration and dewarping methods was quantified. In Chapters 3 and 4 our methods for localizing needle tips in TRUS and seeds in fluoroscopic images were supported with tests on clinical data. In this chapter our overall approach is validated on a phantom and tested on clinical data.

Reporting meaningful error parameters is difficult. The error in localizing seeds in the phantom is easily computed, but the phantom lacks the noise of clinical images along with intraoperative seed motion. However, it is difficult to define a *gold standard* for the location of seeds in clinical data.

Similar problems in validation of RTD system are evident in works discussed in Chapter 1. The system presented in [23] is tested on two phantoms and the root mean square error is reported to be 0.8 mm and 1.3 mm. The registration error is reported separately. The total radiation dose received by the prostate (i.e. D90 and V100) is compared to that determined from CT images. The work reported in [52] is also validated using a phantom reporting point-pair error.

In [11] the results of using an IMR imaging machine to computed RTD are reported in terms of dose coverage to anatomical structures, such as the rectum and urethra, and percentage of under-dosed regions. Here, implants with and without interactive planning are compared. This form of validation assumes the seeds are being accurately located and requires that interactive planning be done throughout the procedure.

In [40] the seed distribution determined from three fluoroscopic images was projected onto the same fluoroscopic images. The difference between the location of the projected seed and the seed

artifact in the images is reported to have a mean of 0.5 mm. In [56] and [53] similar approaches for RTD are compared to the seed locations found using traditional radiographic three-film methods. In all works a point-pair error between the seed distributions is reported.

From the variety of error metrics reported in these works it is clear a gold standard for validating RTD systems have not been established. In this work CT images are used to define the location of the seeds. Although in most institutions CT images are used to define post-operative dosimetry, the resulting seed distribution does suffer from post-operative seed migration, prostate swelling and errors in locating the seed locations in the CT images [37]. Furthermore it is difficult to report meaningful error metrics, so several based on dosimetry and seed distributions are reported.

6.1 Phantom Results

The phantom shown in Figure 6.1a was constructed to further validate our registration algorithm and to estimate the accuracy with which our system can locate seeds. The phantom is contained in a Plexiglas box (approximately 100 mm in each dimension). In one wall of the box there is one 32.5 mm diameter hole to insert a TRUS probe and four 1.5 mm diameter holes to insert needles. Mounted on the inside of the same wall is a metal needle guide to prevent needle deflection. On the inside of the opposite wall there is a Plexiglas shelf with four grooves to hold seeds that are aligned with the holes in the needle guide. A latex condom filled with ultrasound gel extends from the 32.5 mm diameter hole to the opposite wall to simulate the rectum. Twelve seeds are secured in the grooves of the Plexiglas shelf and the remaining space in the phantom is filled with gelatin (13 percent gelatin and 3 percent cellulose by mass).

A TRUS probe was inserted in the condom to a pre-determined depth between the metal needle guide and the Plexiglas shelf (the angle was measured to be approximately zero). A single fluoroscopic image was acquired (see Figure 6.1b). The first needle was inserted until the needle tip appeared in the TRUS image (see Figure 6.1c). The distance from the wall of the phantom to the hub of the needle was recorded. Using this distance and the fluoroscopic image of the TRUS probe, the TRUS image and fluoroscopic image spaces were registered. Three more needles were inserted until each needle tip appeared in the TRUS image.

The seed coordinates found by our system closely match the known seed locations. The mean absolute error in the x, y, and z-directions is 0.96 mm, 0.33 and 0.68 mm, respectively, and the

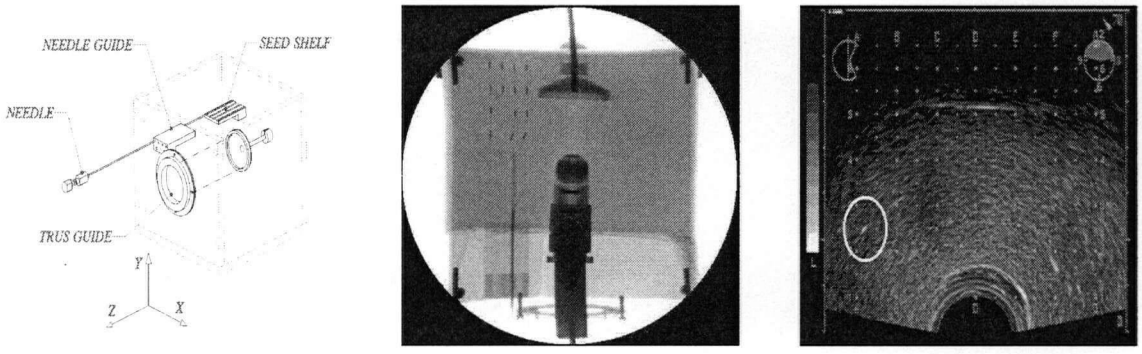

(a) (b) (c)

Figure 6.1: (a) Diagram of the phantom, (b) a fluoroscopic image of the phantom, and (c) a TRUS image of the phantom (the needle tip artifact is enclosed by a circle)

maximum error is 1.85 mm, 0.56 mm and 1.63 mm. The mean and maximum error in Euclidean distance are 1.40 mm and 1.84 mm, respectively. Table 6.1 gives the error for each seed in the phantom. These results support our approach for registering the TRUS and fluoroscopic image and our method for computing the coordinates of the seeds. However, our approach must be tested on clinical data to prove its overall ability to achieve real-time dosimetry.

Table 6.1: The error in the distance between the known location and the computed location of the seeds in the phantom.

Seed	Error in x (mm)	Error in y (mm)	Error in z (mm)	Error in Euclidian Distance (mm)
1	-0.78	-0.43	-1.61	1.84
2	0.19	-0.14	-0.57	0.61
3	1.01	-0.27	0.05	1.05
4	1.72	-0.56	0.08	1.81
5	-0.51	-0.39	-1.60	1.72
6	0.46	-0.13	-0.46	0.66
7	-0.63	-0.35	-1.63	1.78
8	0.92	-0.25	-0.02	0.95
9	1.85	-0.50	0.42	0.96
10	-0.74	-0.30	-1.32	1.54
11	1.04	-0.22	0.08	1.06
12	1.68	-0.45	0.31	1.76

6.2 Clinical Results

Our approach was tested on clinical data collected during eight prostate brachytherapy implants. The ultrasound video was captured at 30 frames per second using an Adaptec AVC-2210 video capture device. The video was digitized as MPEG file format and later compressed using the DIVXMPG4 (version 3) codex to an AVI file format. Fluoroscopic images were acquired as described in Figure 1.4, stored digitally as bitmaps on the fluoroscope's hard drive, and later downloaded through the machine's floppy drive. All procedures were recorded with a video camera and synchronized with the US video so the time of each needle retraction is known. Computed tomography (CT) images of the patient's prostate were acquired three to four hours after each implant and the seed artifacts were located in the CT images using Variseed's software.

The images acquired during the implants were processed post-operatively. For each case two seed distributions were generated from the seed locations found using our RTD system and the CT images. The two seed distributions are registered by defining a transformation from the CT to RTD seed distributions. An initial transformation between the two distributions is guessed based on the typical difference in the orientation of the prostate between the CT and TRUS images acquired during the implant. In some cases the two seed distributions are manually observed to be significantly different. In these cases, matching seeds in the two distributions are manually selected to define an initial transformation.

Next, corresponding points within a fixed distance between the two distributions are selected using a closest point method (typically resulting in more than ten points). A transformation, restricted to rotations, translations and scaling, is defined. Rotations and translations are required to account for the different coordinates system between the RTD and CT data. Scaling accounts for uniform post-operative prostate swelling. This is acceptable because the registration method, which would contribute error in scaling, is validated in Chapter 1 and with our phantom experiment. Shearing is not allowed because it will inaccurately deform the CT distribution to match the RTD seed distribution. Figure 6.2 compares a set of registered RTD and CT seed distributions in three orthogonal views (the seed distributions for all eight cases are given in Appendix B).

Two sets of error, each with several metrics, are reported. The first set are based on dose and the second based on the distance between seeds in the two distributions. In both cases the seed locations determined from the CT images are considered to be the *gold standard*.

The first dose metric computes the percent error in dosimetry, $e(x, y, z)$, on a voxel-by-voxel basis as follows:

$$e(x, y, z) = \frac{D_{RTD}(x, y, z) - D_{CT}(x, y, z)}{D_{CT}(x, y, z)} \cdot 100, \tag{6.1}$$

where x, y, and z are the coordinates of the voxel, and D_{RTD} and D_{CT} represent the dosimetry computed using Equation 5.4 and the seed distributions found from RTD and CT data, respectively. The mean percentage error, μ_e, is given in Table 6.2 and a plot of the percentage error versus percentage volume are reported (see Figure 6.3 as a example and Appendix B for the results for all cases).

The second dose metric uses a minimum dose threshold, defined as the $D90$ (the computation of the $D90$ is discussed below). Voxels that are below this threshold are located in both D_{RTD} and D_{CT} and mean Euclidean distance to the closest under-dosed voxel in D_{CT}, $\mu_{disUDose}$, is computed. This value for each case is reported in Table 6.2. This metric indicates the accuracy with which our RTD system can identify under-dosed regions, and therefore assist in interactive planning.

The last dose metric compares the dose delivered to the entire prostate. The $D90$ is defined as the dose delivered to 90 percent of the prostate volume and the $V100$ is the percentage of the prostate receiving 100 percent of the prescription dose. For both metrics the prostate volume is defined as a rectangular box enclosing both seed distributions with a 5 mm boarder. The $D90$ and $V100$ for the RTD and CT seed distribution are denoted $D90_{RTD}$ and $V100_{RTD}$ and $D90_{CT}$ and $V100_{CT}$, respectively. The results are given in Table 6.2 for each case.

Because the dosimetry calculation is very sensitive to small errors when the seed is close to a voxel center, three parameters based on just the seed distributions are given. The first, e', is defined as Equation 6.1, but dose computation is defined as:

$$D_x(r) = \frac{1}{r^2}, \tag{6.2}$$

where D_x represents the dose computation for D_{RTD} and D_{CT} and r is the distance between a seed and voxel center. This is essentially the same as Equation 5.4, except $g_p(r)$ and $F(r, \theta)$ are excluded. In the second, e'' is again defined as Equation 6.1, except the dose computation is defined as:

$$D_x(r) = \frac{1}{r}, \tag{6.3}$$

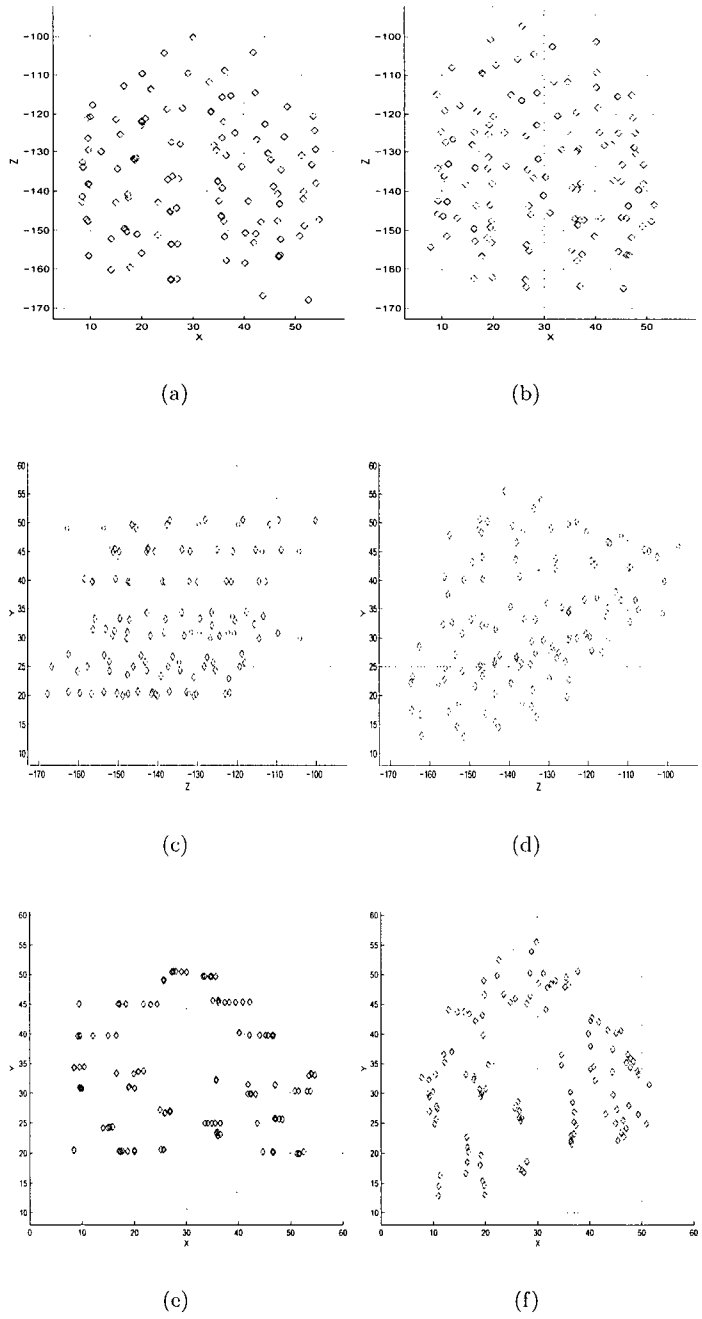

Figure 6.2: A top view of (a) the RTD and (b) the CT seed distributions, (c) and (d) are a side view of the RTD and CT seed distributions, respectively, and (e) and (f) are a front view of the RTD and CT seed distributions, respectively.

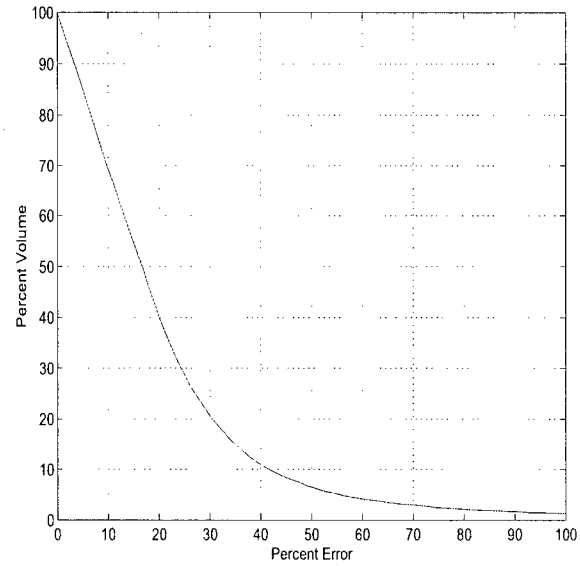

Figure 6.3: A plot of percent error in dosimetry (see Equation 6.1) versus percent volume.

where D_x represented the dose computation for D_{RTD} and D_{CT} and r is the distance between a seed and voxel center. The last metric is the Euclidian distance between a seed in the RTD distribution and the closest seed in the CT distribution and the mean, μ_{pp}, is reported for each case. These metrics are given in Table 6.3 for each case of clinical data.

Table 6.2: The dose error metrics reported for the clinical data.

Case	μ_e (percent)	$\mu_{disUDose}$ (mm)	$D90_{RTD}$ (Gy)	$D90_{CT}$ (Gy)	$V100_{RTD}$ (percent)	$V100_{CT}$ (percent)
A	22.75	0.38	36.0	33.3	32.7	30.9
B	21.02	0.40	62.2	65.1	58.2	58.9
C	22.96	0.23	28.4	35.3	26.2	34.0
D	18.31	0.15	18.1	17.8	24.9	24.6
E	31.31	0.30	35.9	40.2	45.0	47.9
F	25.24	0.20	23.7	22.9	44.2	42.6
G	22.71	0.24	46.6	47.6	52.1	51.6
H	20.18	0.29	34.4	32.5	32.8	30.9
Phantom	17.01	0.01	30.1	31.6	37.4	37.4

Table 6.3: The distance error metrics reported for the clinical data.

Case	$\mu_{e'}$ (percent)	$\mu_{e''}$ (percent)	μ_{pp} (mm)
A	18.42	4.35	3.60
B	17.80	3.96	3.84
C	17.46	3.83	4.33
D	13.15	2.40	4.49
E	23.24	6.09	4.43
F	18.62	4.90	4.33
G	17.62	4.56	4.15
H	15.83	3.55	4.01

6.3 Discussion

The clinical results given in Tables 6.2 and 6.3 show that our approach can be used on clinical noisy images. These tables also show the accuracy of the system varies significantly by the error matric reported.

A sample of the two seed distributions is shown in Figure 6.2 (the seed distributions for all cases is given in Appendix B). In the RTD and CT seed distributions boundaries of the two seed distributions roughly match, however the frontal view shown in Figures 6.2e and 6.2f appear to be rotated about the z-axis by approximately 90 degrees. Referring to Figure 6.2d we see there is significant postoperative swelling in negative z-direction. This is occurs because this end of the prostate is not constrained by the pubic arch and allowed for more swelling than in the positive z-direction. This swelling causes the frontal view of the seed distribution to appear as columns of seeds.

6.3.1 Sources of Error

First, there is error in the location of seeds found using our approach. This error results from the registration of the TRUS and fluoroscopic images, the localization of needle tips, the localization of seed in the fluoroscopic image, and intraoperative seed motion.

Unfortunately, the seed distribution found using CT images is not always representative of the

seed distribution at the time of the implant. It is well known that after an implant the prostate continues to swell resulting in the seed migration. In [19] CT images obtained the day of or immediately after an implant are reported to underestimate the dose delivered to the prostate because the prostate is larger than at any other time in the protracted dose delivery period. And, in [61] and [60] post-operative edema is reported to increase the prostate volume 40 to 50 percent. Although our registration technique allows for scaling of the seed distributions to partly compensate for edema, nonuniform swelling and the resulting seed migration are not accounted for. Our observations have also shown that the seeds move between sequential fluoroscopic images. It is reasonable to assume that if the seeds migrate intraoperatively they will continue to move immediately after the implant.

Error is also introduced into our validation method when defining a transformation between the RTD and CT seed distributions. The corresponding points do not exactly match because of the errors present in both distributions as mentioned above.

6.3.2 Percentage Dose Error

The percentage dose error, μ_e, is quite high for all cases. The equation for the dose computation is given as Equation 5.4, but repeated for the purposes of discussion:

$$D(r) = \lambda^{-1} \cdot S_{Ko} \cdot \Lambda \cdot \frac{G_p(r)}{G_p(r_o)} \cdot g_p(r) \cdot \phi_{an}(r). \tag{6.4}$$

Since, dose is inversely proportional to the square of the distance between the grid point and the seed location. Therefore, this function is very sensitive to seeds that are close to the voxel center. The $g_p(r)$ function also contributes to this sensitivity. Figure 6.4 shows a plot of $g_p(r)$ versus r to illustrate this point.

The μ_e for the phantom is 17.01 percent when compared to the known seed locations. In this case the mean and maximum error in Euclidian distance are 1.40 mm and 1.96 mm, respectively. This shows that a small error in seed locations results in a large error in the percentage error in dose.

6.3.3 Seed Distribution Error

To get a better idea of the relationship between the seed locations, dosimetry was computed without the g_p and F_p term in Equation 6.4. These results, given in Table 6.3 show significantly less error

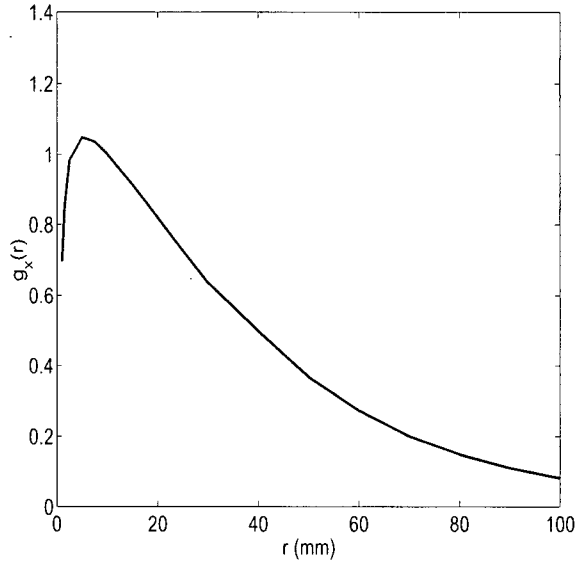

Figure 6.4: A plot of $g_p(r)$ versus r to show $g_p(r)$ has a significant impact on dosimetry.

than those in e. When dose is computed as being only inversely proportional to the distance from the grid point the error drops significantly. The purpose of these metrics is to show the two seed distributions are reasonable close.

6.3.4 Under-dosed Distance Error

Reporting the error mean error between under-dosed voxels indicates how well regions not receiving sufficient dose are found using our approach. For most cases the mean distance between under-dosed regions between the two distributions is low. This is partly because under-dosed regions typically appear on the extremes of the volumes.

6.3.5 Dose Volume Error

For most cases the $D90$ and $V100$ closely correspond between the RTD and CT seed distributions. As reporting in [19] determining the dose delivered to the entire prostate is not necessarily indicative of the location of the seeds. There are many different seed distributions that can give the same D90 and V100 values. That being said, these metrics are used to support the RTD systems proposed in [23]. These parameters is commonly reported in literature as they are meaningful to the medical community and a correlation between the D90 and tumor control was found in [19].

6.4 Conclusion

The results from a phantom study strongly support our method to compute seed distributions. However, both the TRUS and fluoroscopic images of the phantom images lack the noise of clinical images. The eight cases of clinical data presented (plots of the seed distributions are given in Appendix B) lends support to our method, however the seed distributions determined from post-operative CT images do not provide an ideal gold standard.

It might be possible to achieve a more accurate gold standard by acquiring three or more fluoroscopic images of the patient at the end of an implant. But, the films must be taken at a sufficiently large angle to limit seed exclusion and seed artifacts merging. The three-film algorithm presented in [40] is reported to give the best results on clinical data.

Chapter 7

Conclusions and Future Work

A means of computing real-time dosimetry for prostate brachytherapy has been presented. Our approach is designed to fit into the current protocol practiced at the VCC and using the currently available image equipment. Our method has resulted in several contributions.

1. A new method to register TRUS and fluoroscopic using a single fluoroscopic image of the TRUS probe has been presented and tested. A fluoroscopic image of the TRUS probe is acquired, then using the known dimensions of the TRUS probe and the C-arm a transformation between the two images is computed. The transformation is determined with enough accuracy to back-project the location of the seed artifacts from the fluoroscopic image to the TRUS image. The position of the TRUS probe with respect to the fluoroscopic image is determined with a maximum error of 5.8 mm, which occurs in determining the height of the probe above the fluoroscopic image. The rotation about the x-axis is determined with limited accuracy, but it has been shown that this does not contribute significant error to the transformation.

2. A new method of automatically determining the location of a needle tip in a TRUS is presented. To the best of our knowledge, a method to automatically locate the position of a needle in an image perpendicular to the needle direction has not been previously reported. To achieve this, clustered changes in intensity between sequential TRUS images are detected and the needle tip is localized using an adaptive thresholding technique. Our method has been shown to work on clinical data.

3. A means of delineating brachytherapy seeds from a fluoroscopic image is presented based on previously published work. Using the predicted location of the seeds and the known seed spacing, a new method of matching the seed artifacts to a needle path is presented. The distance between the seeds and the predict seed locations is modelled as a spring and the energy in the springs is minimized to determine the seed artifacts that match to a given needle path.

4. Intraoperative seed motion is tracked throughout the procedure. Although the multiple film systems reported in the literature could be used to track intraoperative seed motion, to the best of our knowledge no such work has been previously reported. In this work the seed motion in the coronal plane is determined by updating the position of the seeds from sequential fluoroscopic images. A correlation technique is used to track artifacts in TRUS. The motion of these artifacts is used to determine the vertical motion of the seeds with respect to the TRUS probe.

5. A new procedure to compute the location of seeds as they are implanted for prostate brachytherapy is presented. The coordinate of each needle tip is determined from TRUS. After each fluoroscopic image is acquired at a fixed angle, the (x,z)-coordinates of the seeds are determined and back-projected to the TRUS image. A needle path is interpolated from the needle tip to the known entry point of the needle in the needle guide and the y-coordinates of the seeds are computed. The resulting dosimetry is displayed in the TRUS image frame allowing the radiation oncologist to do interactive planning. To the best of our knowledge, this is the first work to fuse fluoroscopy and TRUS to compute the seed distribution. Furthermore, the C-arm does not need to be rotated throughout the procedure to update the dosimetry allowing the system to be easily integrated into the current protocol used for prostate brachytherapy at the VCC.

6. Our method has been validated on a phantom and tested on clinical data. The phantom results show the accuracy of our approach under ideal conditions. The clinical data shows that our approach is feasible in a clinical setting. However, it is difficult to determine the accuracy of our system using the present clinical data.

7.1 Future Work

As this system is a first prototype there are several opportunities for future work.

1. Many parameters are used for finding the needle tip in TRUS and the location of the seeds in a fluoroscopic image. Optimizing these parameters and increasing the robustness of these algorithms will decrease the amount of manual interventions required by our system.

2. Our approach could be further tested on clinical data and possible better validated if three or more fluoroscopic images of the seed distribution were acquired at the end of the procedure. Postoperative seed motion would be less than is observed in postoperative CT images acquired three to four hours after the procedure.

3. Because our approach requires the radiation oncologist and radiation therapists to interact with our system an user interface needs to be developed and tested in the operating room. Such an interface will require significant feedback from both the radiation therapists and the radiation oncologists.

4. Accurately delineating the prostate volume from the TRUS images would allow for better tracking of intraoperative seed motion. This could be expanded to recommend seed or needle tips locations to the radiation oncologist to ensure the prostate receives enough radiation to destroy all the cancerous cells.

Bibliography

[1] M.D. Altschuler, P.A. Findlay, and R.D. Epperson. Rapid, accurate, three-deminisional location of multiple seeds in implant radiotherapy treatment planning. *Physics in Medicine and Biology*, 28:1305–1318, 1983.

[2] H.I. Amols and I.I. Rosen. A three-film technique for reconstruction radioactive seed implants. *Medical Physics*, 8:210–214, 1981.

[3] N. Archip and R. Rohling. Approximation of the center and radius of C-arm images for automatic on-line camera calibration. Technical report, Department of Electrical and Computer Engineering, 2003.

[4] L. Beaulieu, D. Tubic, J. Pouliot, E. Vigneault, and R. Taschereau. Post-implant dosimetry using fusion of ultrasound images with 3D seed coordinates from fluoroscopic images in transperineal interstitial permanent prostate brachytherapy. In *Proceedings of 42nd Annual Meeting of the American Society for Therapeutic Radiology and Oncology*, October 2000.

[5] P.J. Biggs and D.M. Kelly. Geometric reconstruction of seed implants using a three-film technique. *Medical Physics*, 10:701–704, 1983.

[6] W.F. Bird, J.M. Coggins, and E.L. Chaney. Towards automated brachytherapy film implant labeling using statical pattern recognition. In *Proc. of the Seventh Annual IEEE Symposium on Computer-Based Medical Systems*, June 1994.

[7] L.N. Bohs and G.E. Trahey. A novel method for angle independent ultrasonic imaging of blood flow and tissue motion. *IEEE Transactions on Biomdeical Engineering*, 38:280–286, 1991.

[8] L. Chauveic, T. Flam, S. Solignac, N. Thiounn, F. Firmin, B. Debre, J. Rosenwald, P. Phlips, and J. Cosset. Prostate cancer brachytherapy: Is real-time ultrasound-base dosimetry predictive of subsequent CT-based dose distribution calculation? A study of 450 patients by the Institut Curie/Hospital Cochin (Paris) Group. *Int. J. Radiation Oncology Biol Phys*, 59(3):691–695, 2004.

[9] S. Chen and M. Haralick. Recursive erosion, dilation, opening, and closing transforms. *IEEE Trans. Image Process.*, 4:335–345, 1995.

[10] P.S. Cho. Computerized segmentation of clustered seeds in prostate brachytherapy. In *Proc. 13th Int. Conf. on Computers in Radiotherapy*, page 105, May 2000.

[11] R.A. Cormack, H. Kooy, C.M. Tempany, and A.V. D'Amico. A clinical method for real-time dosimetric guidance of transperineal ^{125}I prostate implants using interventional magnetic resonance imaging. *Int. J. Radiation Oncology Biol Phys*, 46(1):207–214, 2000.

[12] R.A. Cormack, C.M. Tempany, and A.V. D'Amico. Optimizing target coverage by dosimetric feedback during prostate brachytherapy. *Int. J. Radiation Oncology Biol Phys*, 48(1):1245–1249, 2000.

[13] Nucletron Corporation. Spot, May 2004.

[14] A.V. D'Amico, R. Cormack, C.M. Tempany, S. Kumar, G. Topulos, H.M. Kooy, and C.N. Coleman. Real-time magnetic resonance image-guided interstitial brachytherapy in the treatment of select patients with clinically localized prostate cancer. *Int. J. Radiation Oncology Biol Phys*, 42(3):507–515, 1998.

[15] M. Ding, H.N. Cardinal, and A. Fenster. Automatic needle segementation in three-dimensional ultrasound images using two orthogonal two-dimensional image projections. *Medical Physics*, 30:222–234, 2003.

[16] M. Ding and A. Fenster. Projection-based needle segmentation in 3D ultrasound images. In *Proc. of 6th MICCAI Conference*, Sept 2003.

[17] M. Ding and A. Fenster. A real-time biopsy needle segmentation technique using Hough transform. *Medical Physics*, 30:2222–2233, 2003.

[18] K.J. Draper, C.C. Blake, L. Gowman, D.B. Downey, and A. Fenster. An algorithm for automatic needle localization in ultrasound-guided breat biopsies. *Medical Physics*, 27:1971–1978, 2000.

[19] W.D. D'Souza, H.D. Thames, and D.A. Kuban. Dose-volume conundrum for response of prostate cancer to brachytherapy: Summary dosimetric measures and their relationship to tumor control probability. *Int. J. Radiation Oncology Biol Phys*, 58:1540–1548, 2004.

[20] R. Ebrahimi and S. Okazawa. Hand-held steerable needle device. Master of Engineering, University of British Columbia, Department of Mechanical Engineering, 2004.

[21] D.G. French, J. Morris, M. Keyes, and S.E. Salcudean. A real-time dosimetry system for prostate brachytherapy using TRUS and fluoroscopy. In *Proc. of 7th MICCAI Conference*, Sept 2004.

[22] G. Gil and Y. Yoon. C-arm image distortion calibration method for computer-aided surgery. *International Journal of Human-friendly Welfare Robotic Systems*, 4(1):20–26, 2003.

[23] L. Gong, P.S. Cho, B.H. Han, K.E. Wallner, S.G. Sutlief, S.P. Pathak, D.R. Haynor, and Y. Kim. Ultrasonography and fluoroscopic fusion for prostate brachytherapy dosimetry. *Int. J. Radiation Oncology Biol Phys*, 54(1):1322–1330, 2002.

[24] B.H. Han, K. Wallner, G. Merrick, W. Butler, S. Sutlief, and J. Sylvester. Prostate brachytherapy seed identification on post-implant TRUS images. *Medical Physics*, 30(1):898–900, 2003.

[25] D.R. Holmes, B.J. Davis, C.J. Bruce, and R.A. Robb. 3D visualization, analysis, and treatment of the prostate using trans-urethral ultrasound. *Computerized Medical Imaging and Graphics*, 27:339–349, 2003.

[26] D.R. Holmes and R.A. Robb. Improved automated brachytherapy seed localization in trans-urethral ultrasound data. In *Proceedings of SPIE - The International Society for Optical Engineering, Progress in Biomedical Optics and Imaging - Medical Imaging 2004: Visualization, Image-Guided Procedures, and Display*, Feb 2004.

[27] J. Hong, T. Dohi, M. Hashizume, K. Konishi, and N. Hata. An ultrasound-driven needle-insertion robot for percutaneous cholecystomy. *Physics in Medicine and Biology*, 49:441–455, 2004.

[28] CMS Inc. Interplant, May 2004.

[29] A. Jain, T. Mustufa, Y. Zhou, E.C. Burdette, G.S. Chirikjian, and G. Fichtinger. A matching and reconstruction of brachytherapy seeds using the Hungarian algorithm (MARSHAL). In *Proceedings of the Conference on Visualization, Image-Guided Procedures, and Display, SPIE 2005*, Feb 2005.

[30] A. Jain, T. Mustufa, Y. Zhou, E.C. Burdette, G.S. Chirikjian, and G. Fichtinger. A robust fluoroscope tracking and calibration (FTRAC) fiducial. In *Proceedings of the Conference on Visualization, Image-Guided Procedures, and Display, SPIE 2005*, Feb 2005.

[31] H. Kooy, R.A. Cormack, G. Mathiowitz, C.M. Tempany, and A.V. D'Amico. A software system for interventional magnetic resonance image-guided prostate brachytherapy. *Computer Aided Surgery*, 5(1):401–413, 2000.

[32] S.T. Lam, P.S. Cho, R.J. Marks II, and S. Narayanan. Three-dimensional seed reconstruction for prostate brachytherapy using Hough transform. *Physics in Medicine and Physics*, 49:557–569, 2004.

[33] S.A. McAleavey, D.J. Rubens, and K.J. Parker. Doppler ultrasound imaging of magnetically vibrated brachytherapy seeds. *IEEE Trans on Biomedical Engineering*, 50(2):252–255, 2003.

[34] E.M. Messing, J.B.Y. Zhang, D.J. Rubens, R.A. Brasacchio, J.G. Strang, A. Soni, M.C. Schell, P.G. Okunieff, and Y. Yu. Intraoperative optimized inverse planning for prostate brachytherapy: Early experience. *Int. J. Radiation Oncology Biol Phys*, 44(4):801–808, 1999.

[35] F.G. Mitri, P. Trompette, and J. Chapelon. Using vibro-acoustography to detect brachytherapy metal seeds. In *Proceedings of the IEEE Ultrasonics Symposium*, Oct 2003.

[36] F.G. Mitri, P. Trompette, and J. Chapelon. Improving the use of vibro-acoustography for brachytherapy metal seed imaging: A feasibility study. *IEEE Trans on Medical Imaging*, 23(1):1–6, 2004.

[37] S. Nag, W. Bice, K. DeWyngaert, B. Prestidge, R. Stoick, and Y. Yu. The American Brachytherapy Society recommendations for permanent prostate brachytherapy postimplant dosimetric analysis. *Int. J. Radiation Oncology Biol Phys*, 46:221–230, 2000.

[38] S. Nag, J.P. Ciezki, R. Cormack, S. Doggett, K. DeWyngaert, G.K. Edmundson, R.G. Stock, N.N. Ston, and Y. Yu. Intraoperative planning and evaluation of permanent prostate brachytherapy: Report of the American Brachytherapy Society. *Int. J. Radiation Oncology Biol Phys*, 51(1):1422–1430, 2001.

[39] S. Narayanan, P.S. Cho, and R.J. Marks II. Fast cross-projection algorithm for reconstruction of seeds in prostate brachytherapy. *Physics in Medicine and Biology*, 29(7):1572–1579, 2002.

[40] S. Narayanan, P.S. Cho, and R.J. Marks II. Three-dimensional seed reconstruction from an incomplete data set for prostate brachytherapy. *Physics in Medicine and Biology*, 49:3483–3494, 2004.

[41] National Cancer Institute of Canada, 2004.

[42] L. Potter. Permanent prostate brachytherapy in men with clinically localised prostate cancer. *Clinical Oncology*, 15(1):301–315, 2003.

[43] M.J. Rivard, B.M. Coursey, L.A. DeWerd, W.F. Hanson, M. Saiful Huq, G.S. Ibbott, M.G. Mitch, R. Nath, and J.F. Williamson. Update of AAPM Task Group No. 43 Report: A revised AAPM protocol for brachytherapy dose calculations. *Medical Physics*, 31:633–668, 2004.

[44] P.L. Roberson, V. Narayana, D.L. McShan, R.J. Winfield, and P.W. McLaughlin. Source placement error for permanent implant of the prostate. *Medical Physics*, 24:251–257, 1997.

[45] M.S. Rosenthal and R. Nath. An automatic seed indentification technique for interstitial implants using three isocentric radiographs. *Medicial Physics*, 10:475–479, 1983.

[46] G. Rossignol, R. Souchon, Y.C. Angel, and J.Y. Chapelon. Using elastography to detect brachytherapy seeds: A feasibility study. In *Proc. of First Int. Conf. Ultrasonic Measurement and Imaging of Tissue Elasticity*, Oct 2002.

[47] R.L. Siddon and L.M. Chin. Two-film brachytherapy reconstruction algorithm. *Medical Physics*, 12:77–83, 1985.

[48] R.G. Stock, N.N. Stone, M.F. Wesson, and J.K. DeWyngaert. A modified technique allowing interactive ultrasound-guided three-dimensional transperineal prostate implantation. *Int. J. Radiation Oncology Biol Phys*, 32:219–225, 1995.

[49] Y. Su, B.J. Davis, M.G. Herman, W.N. LaJoie, and R.A. Robb. Brachytherapy seed localization from fluoroscopic images using a statistical classfier. *Physics in Medicine and Biology*, 29(7):1572–1579, 2002.

[50] Y. Su, B.J. Davis, M.G. Herman, W.N. LaJoie, and R.A. Robb. Fluoroscopy to ultrasound image registration using inplanted seeds as fiducials during permanent prostate brachytherapy. In *Progress in Biomedical Optics and Imaging - Medical Imaging 2004: Visualization, Image-Guided Procedures, and Display*, Feb 2004.

[51] T.S.Y. Tang. Calibration and point-based registration of fluoroscopic images. Master of Science Thesis, Queen's University, Department of Computing and Information Science, 1999.

[52] D.A. Todor, G.N. Cohen, H.I. Amols, and M. Zaider. Operator-free, film-based 3D seed reconstruction in brachytherapy. *Physics in Medicine and Biology*, 47(1):2031–2048, 2002.

[53] D.A. Todor, M. Zaider, G.N. Cohen, M.F. Worman, and M.J. Zelefsky. Intraoperative dynamic dosimetry for prostate implants. *Physics in Medicine and Biology*, 48(1):1153–1171, 2003.

[54] A. Tornes and M. Eriksen. A new brachytherapy seed design for improved ultrasound visualisation. In *Proceedings of the IEEE Ultrasonics Symposium*, Oct 2003.

[55] G.E. Trahey, J.W. Allison, and O.T. Von Ramm. Angle independent ultrasonic detection of blood flow. *IEEE Transactions on Biomdeical Engineering*, 34:965–967, 1987.

[56] D. Tubic, A. Zaccarin, L. Beaulieu, and J. Pouliot. Automated seed detection and three-dimensional reconstruction. II: Reconstruction of permanent prostate implants using simulated annealing. *Physics in Medicine and Biology*, 28(1):2272–2286, 2001.

[57] D. Tubic, A. Zaccarin, J. Pouliot, and L. Beaulieu. Automated seed detection and three-dimensional reconstruction I: Seed localization from fluoroscopic images or radiographs. *Physics in Medicine and Biology*, 28(1):2265–2271, 2001.

[58] E. Turgay. Imaging visco-elastic properties of soft tissue with ultrasound. Master of Applied Science, University of British Columbia, Department of Electrical and Computer Engineering, 2004.

[59] P.M.J. van der Zwet, D.J.H. Meyer, and J.H.C. Reiber. Automated and accurate assessment of the distribution, magnitude, and direction of pincushing distortion in angiographic images. *Investigative Radiology*, 30:204–213, 1995.

[60] F.M. Waterman, N. Yue, B.W. Corn, and A.P. Dicker. Edema associated with I-125 or Pd-103 prostate brachytherapy and its implact on post-implant dosimetry: An analysis base on serial CT aquisition. *Int. J. Radiation Oncology Biol Phys*, 41:1069–1077, 1998.

[61] F.M. Waterman, N. Yue, S. Reisinger, A. Dicker, and B.W. Corn. Effect of edema on the post-operative dosimetry of an I-125 prostate implant: A case study. *Int. J. Radiation Oncology Biol Phys*, 38:335–339, 1997.

[62] M. Zhang, M. Zaider, M. Worman, and G. Cohen. On the question of 3D seed reconstruction in prostate brachytherapy: The determination of X-ray source and film locations. *Physics in Medicine and Biology*, 49:N335–N345, 2004.

Appendix A

Background on Dewarping Functions

In this appendix the details of the two dewarping functions tested in Section 2.4.1 are provided. The first dewarping function is a local model and the second is a global model.

A.1 Local Model

Local models use a grid of known geometry to define transformations between a warped image and an undistorted image. The centroids of the ball bearings in Figure 2.5a are used as tie points. By knowing the undistorted coordinates of the tie points, t_u, and determining the distorted coordinates of the corresponding tie points in the fluoroscopic image, t_d, an affine transformation, A, between the distorted and undistorted coordinate systems can be defined. For the i^{th} element, bounded by a set of three tie points, the following relationship can be defined:

$$t_u(i) = A(i) * t_d(i). \tag{A.1}$$

The affine transformation for a given element is used to dewarp all points inside the element. Using the grid in Figure 2.5a 161 affine transformations were defined.

A.2 Global Model

An alternative to defining multiple transformations is to define just one global transformation to dewarp the whole image. For example,

$$X_d = D * X_u \tag{A.2}$$

where X_u and X_d are the undistorted and distorted coordinates in the fluoroscopic image, respectively and D is the distortion transformation.

The global physical-based model presented in [22] is implemented, where pincushion and S-distortion are considered additive, so the global transformation, D, is defined as:

$$D = D_{rad} + D_{rot} + D_{trans}. \tag{A.3}$$

The pincushion distortion is modelled as:

$$D_{rad}(X_u, Z_u) = (\gamma_1 R_u + \gamma_2 R_u^3) \begin{bmatrix} \frac{X_u}{R_u} \\ \frac{Z_u}{R_u} \end{bmatrix} \tag{A.4}$$

where $R_u = \sqrt{X_u^2 + Z_u^2}$ and γ_1 and γ_2 are constants dependent on the focal length of the C-arm.

S-distortion is decomposed into rotational and translational components denoted by D_{rot} and D_{trans}, respectively:

$$D_{rot}(X_u, Z_u) = (\alpha_1 R_u + \alpha_2 R_u^3) \begin{bmatrix} \frac{-Z_u}{R_u} \\ \frac{X_u}{R_u} \end{bmatrix} \tag{A.5}$$

where α_1 and α_2 are dependent on the magnetic field parallel to the direction the electrons are travelling. This magnetic field acts on the radial velocity of the electrons causing a rotation in the image. And,

$$D_{trans}(X_u, Z_u) = \begin{bmatrix} \beta_{x1} + \beta_{x2} R_u \\ \beta_{z1} + \beta_{z2} R_u \end{bmatrix} \tag{A.6}$$

where β_{x1} and β_{x2} are dependent on the magnetic field transverse to the direction the electrons are travelling. This magnetic field acts on the longitudinal component of the electron's velocity causing a translation in the image.

The grid in Figure 2.5a was used to determine D. The coefficients in D, (γ_1, γ_2, α_1, α_2, β_{x1}, β_{x2}, β_{z1}, and β_{z2}), were determined by minimizing the error in distance between X_d computed using Equation A.2 and the known undistorted locations of the ball bearings.

Appendix B

Results from Clinical Data

In this appendix a three orthogonal plots of the RTD and CT seed distributions and a plot of percentage error in dosimetry (computed using Equation 6.1) are given for each case of clinical data.

B.1 Case A

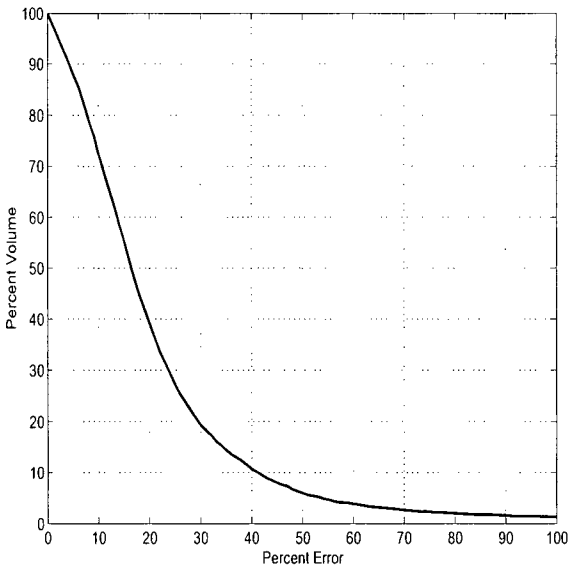

Figure B.1: A plot of percent error in dosimetry (see Equation 6.1) versus percent volume.

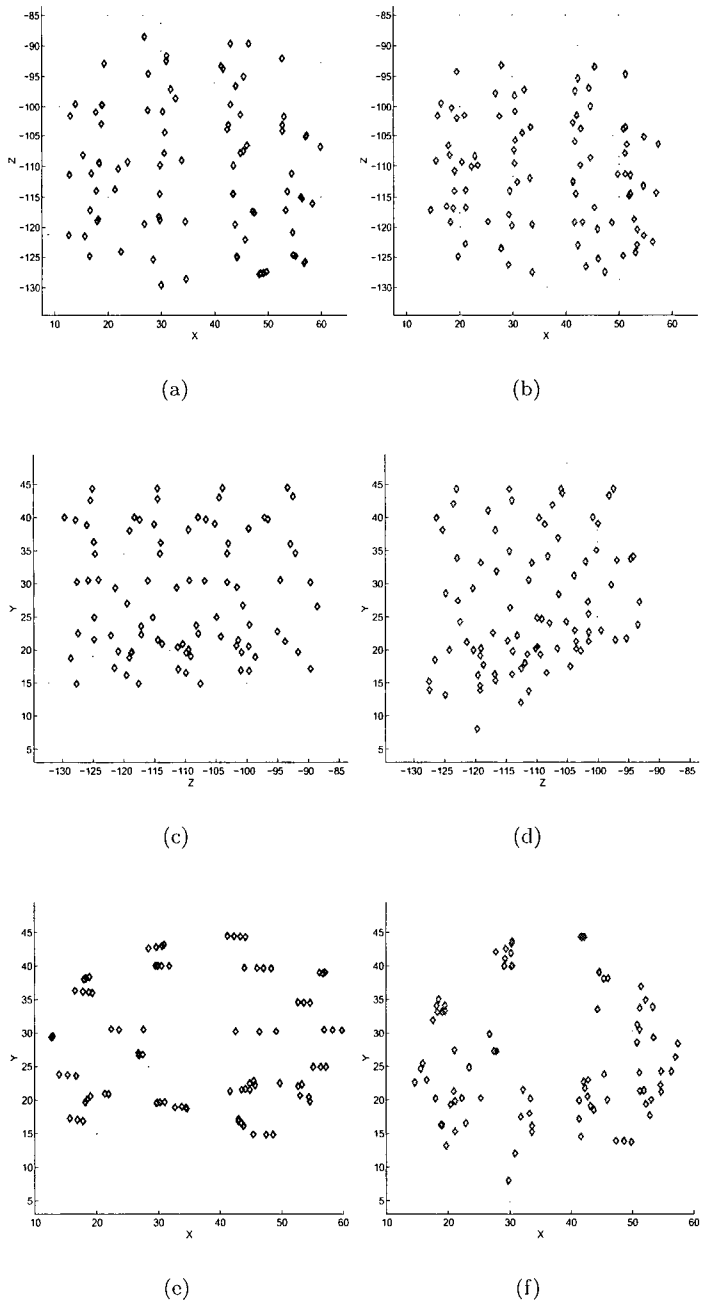

Figure B.2: A top view of (a) the RTD and (b) the CT seed distributions, (c) and (d) are a side view of the RTD and CT seed distributions, respectively, and (e) and (f) are a front view of the RTD and CT seed distributions, respectively.

B.2 Case B

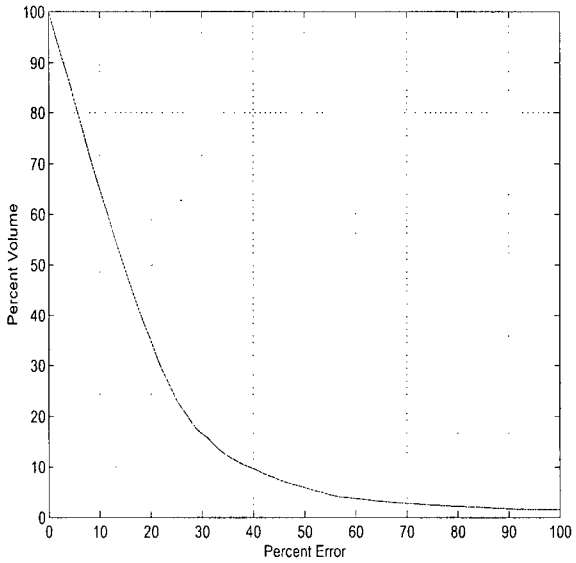

Figure B.3: A plot of percent error in dosimetry (see Equation 6.1) versus percent volume.

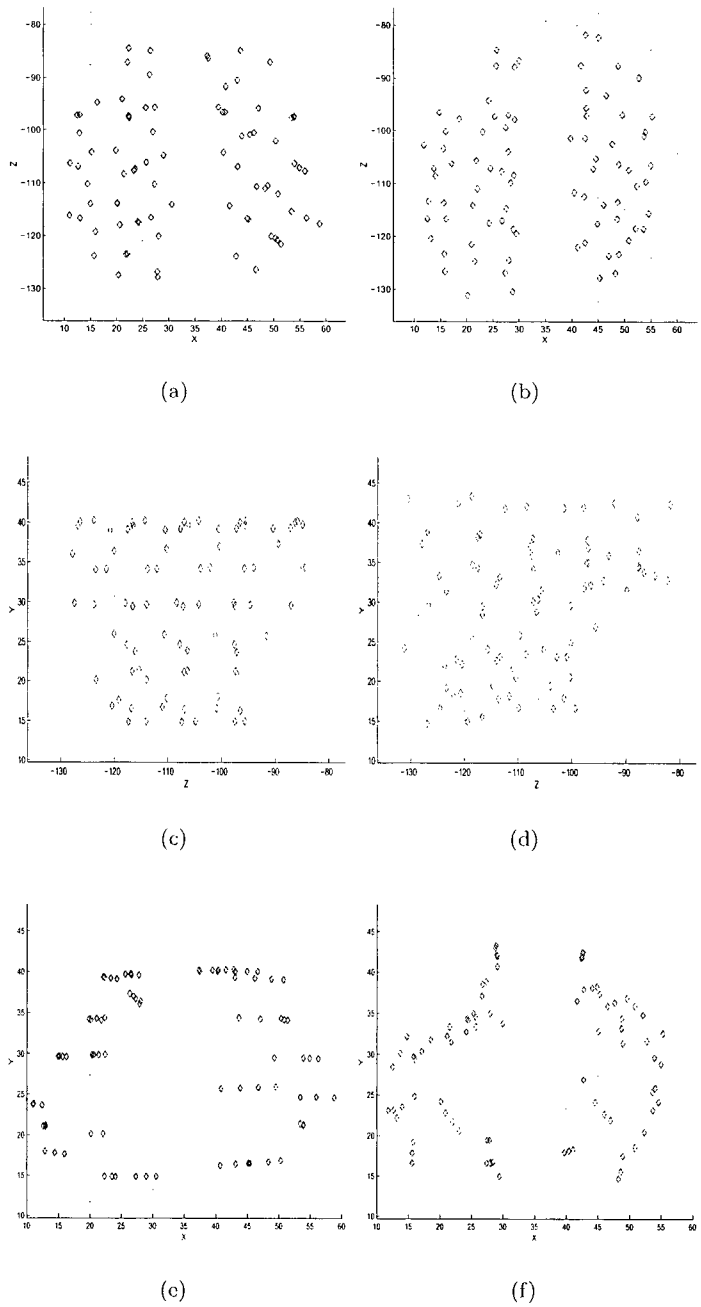

Figure B.4: A top view of (a) the RTD and (b) the CT seed distributions, (c) and (d) are a side view of the RTD and CT seed distributions, respectively, and (e) and (f) are a front view of the RTD and CT seed distributions, respectively.

B.3 Case C

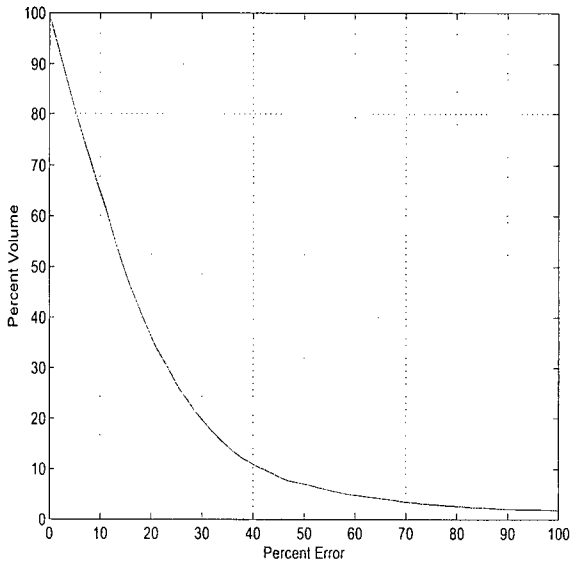

Figure B.5: A plot of percent error in dosimetry (see Equation 6.1) versus percent volume.

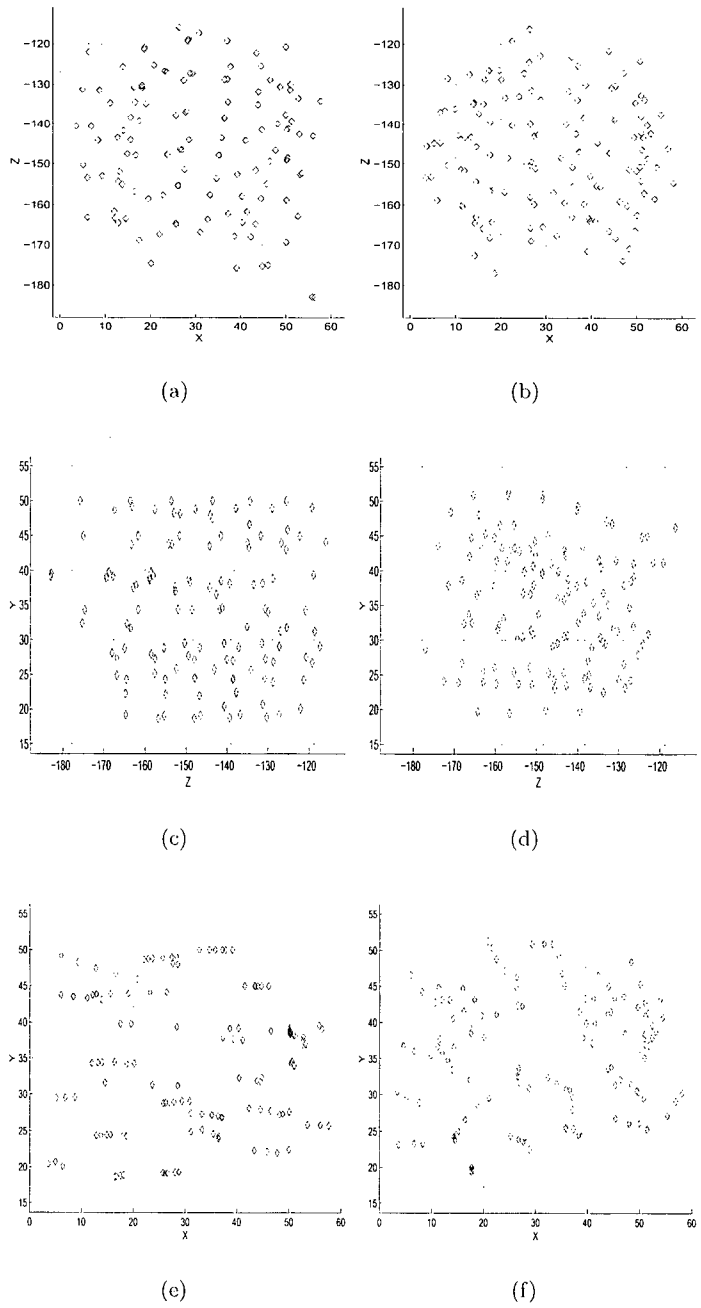

Figure B.6: A top view of (a) the RTD and (b) the CT seed distributions, (c) and (d) are a side view of the RTD and CT seed distributions, respectively, and (e) and (f) are a front view of the RTD and CT seed distributions, respectively.

B.4 Case D

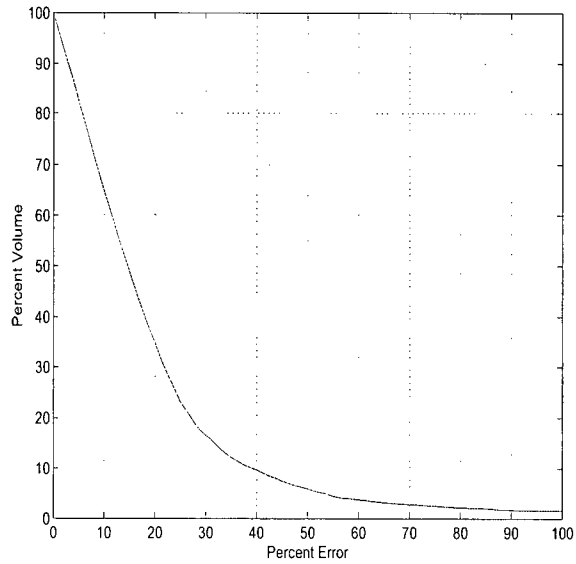

Figure B.7: A plot of percent error in dosimetry (see Equation 6.1) versus percent volume.

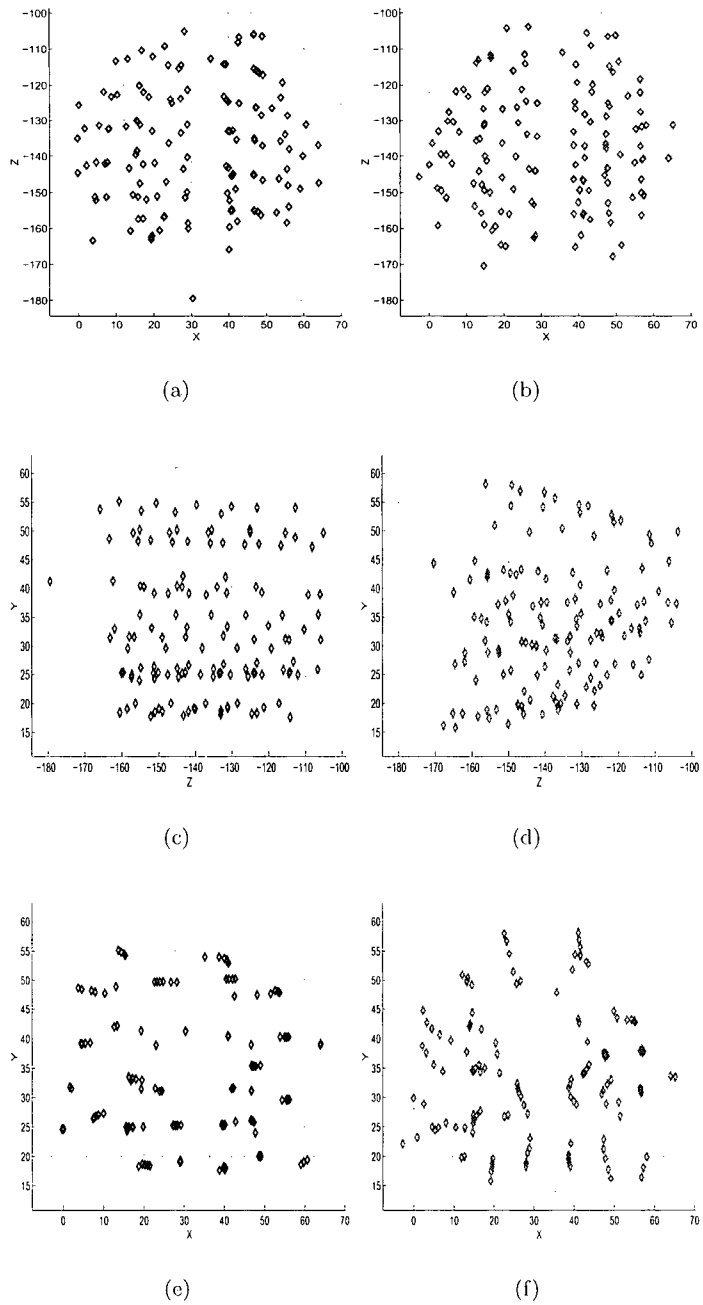

Figure B.8: A top view of (a) the RTD and (b) the CT seed distributions, (c) and (d) are a side view of the RTD and CT seed distributions, respectively, and (e) and (f) are a front view of the RTD and CT seed distributions, respectively.

B.5 Case E

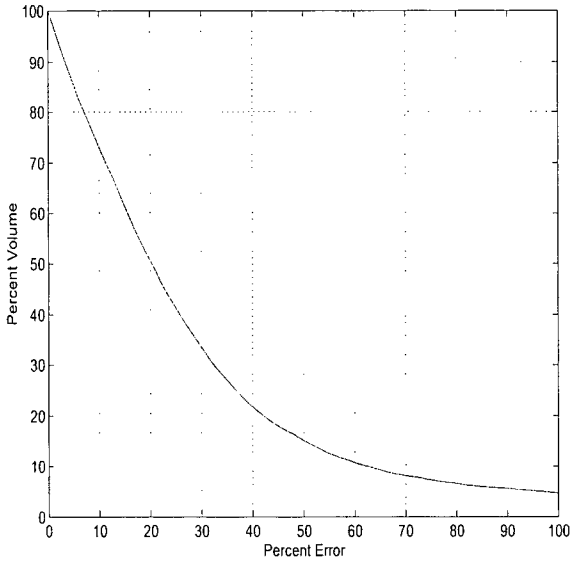

Figure B.9: A plot of percent error in dosimetry (see Equation 6.1) versus percent volume.

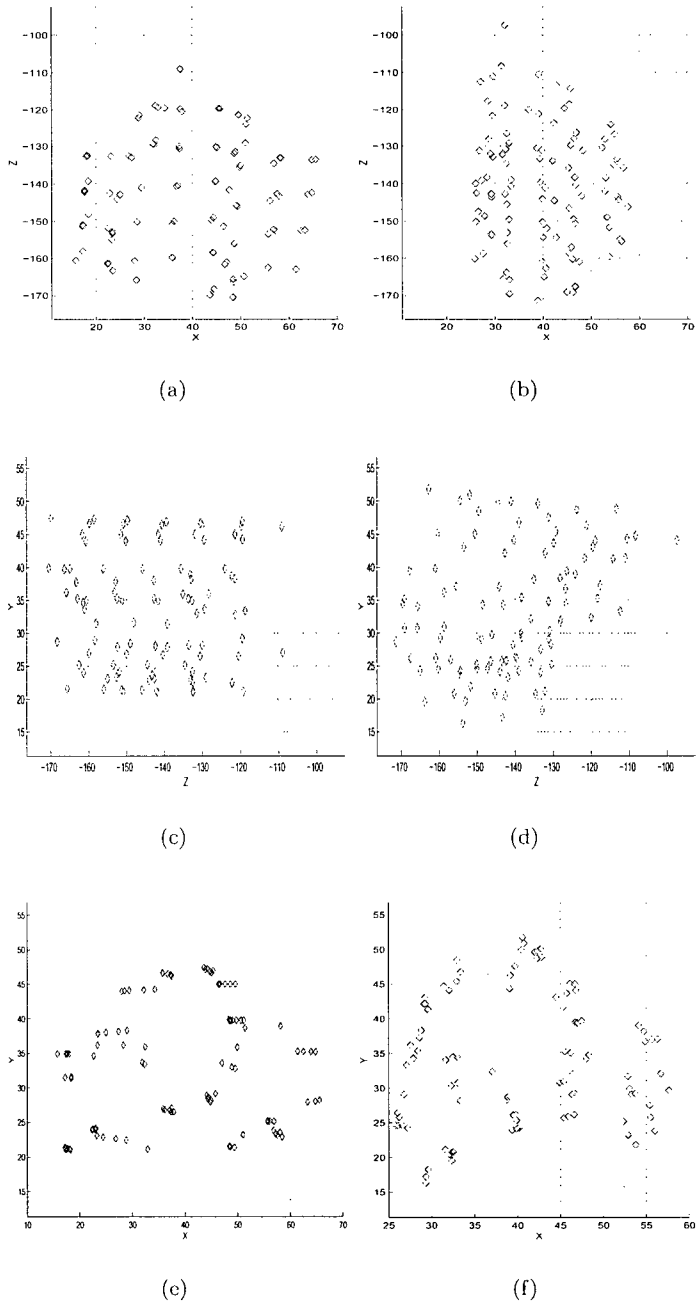

Figure B.10: A top view of (a) the RTD and (b) the CT seed distributions, (c) and (d) are a side view of the RTD and CT seed distributions, respectively, and (e) and (f) are a front view of the RTD and CT seed distributions, respectively.

B.6 Case F

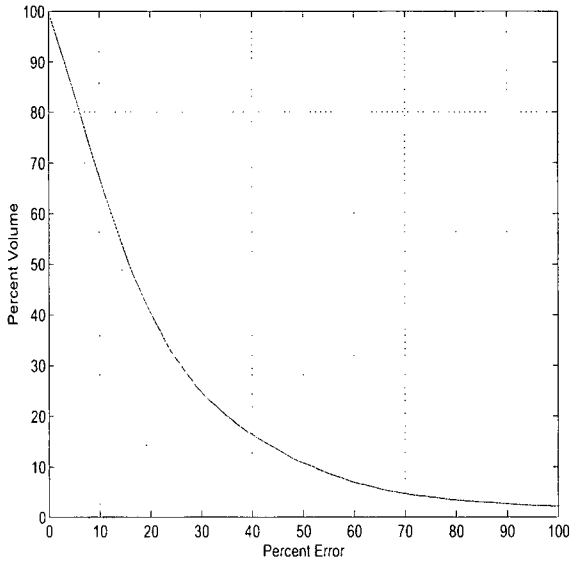

Figure B.11: A plot of percent error in dosimetry (see Equation 6.1) versus percent volume.

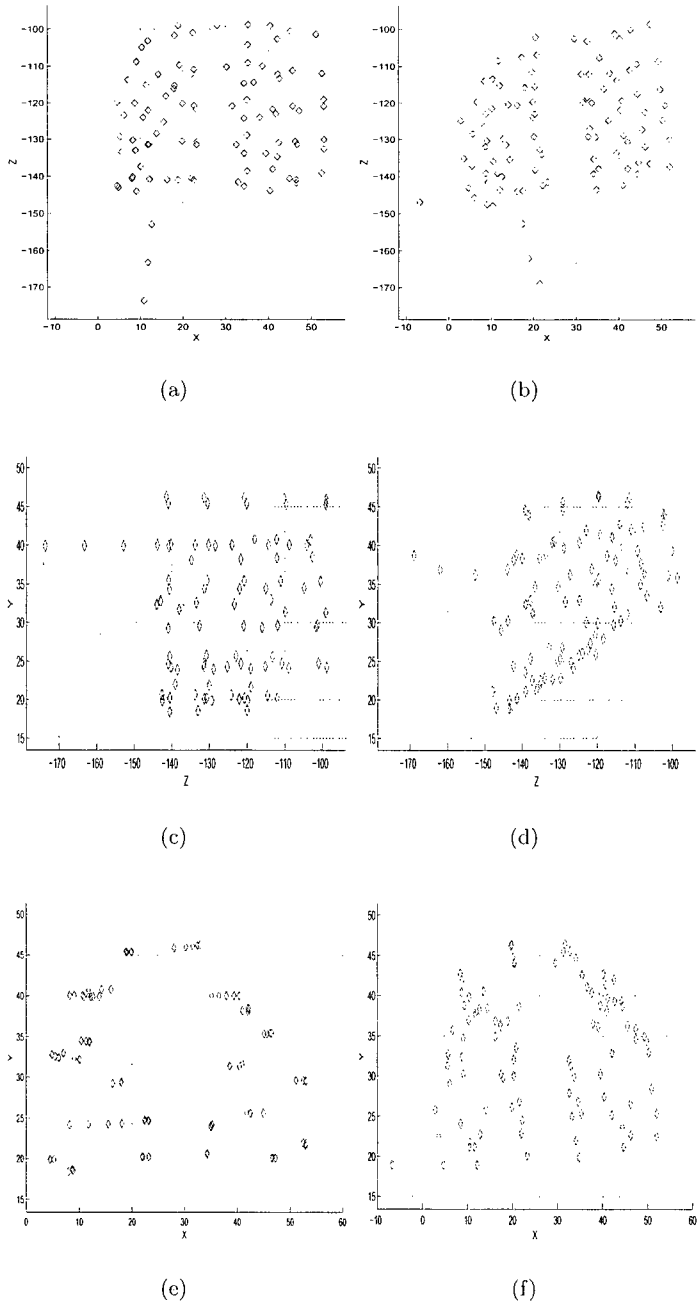

Figure B.12: A top view of (a) the RTD and (b) the CT seed distributions, (c) and (d) are a side view of the RTD and CT seed distributions, respectively, and (e) and (f) are a front view of the RTD and CT seed distributions, respectively.

B.7 Case G

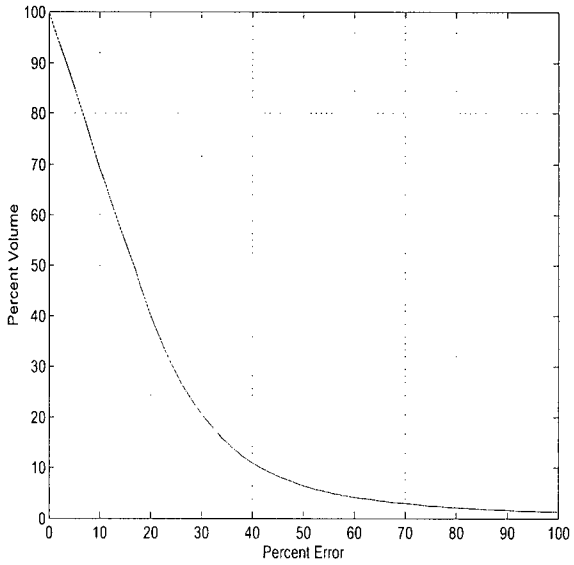

Figure B.13: A plot of percent error in dosimetry (see Equation 6.1) versus percent volume.

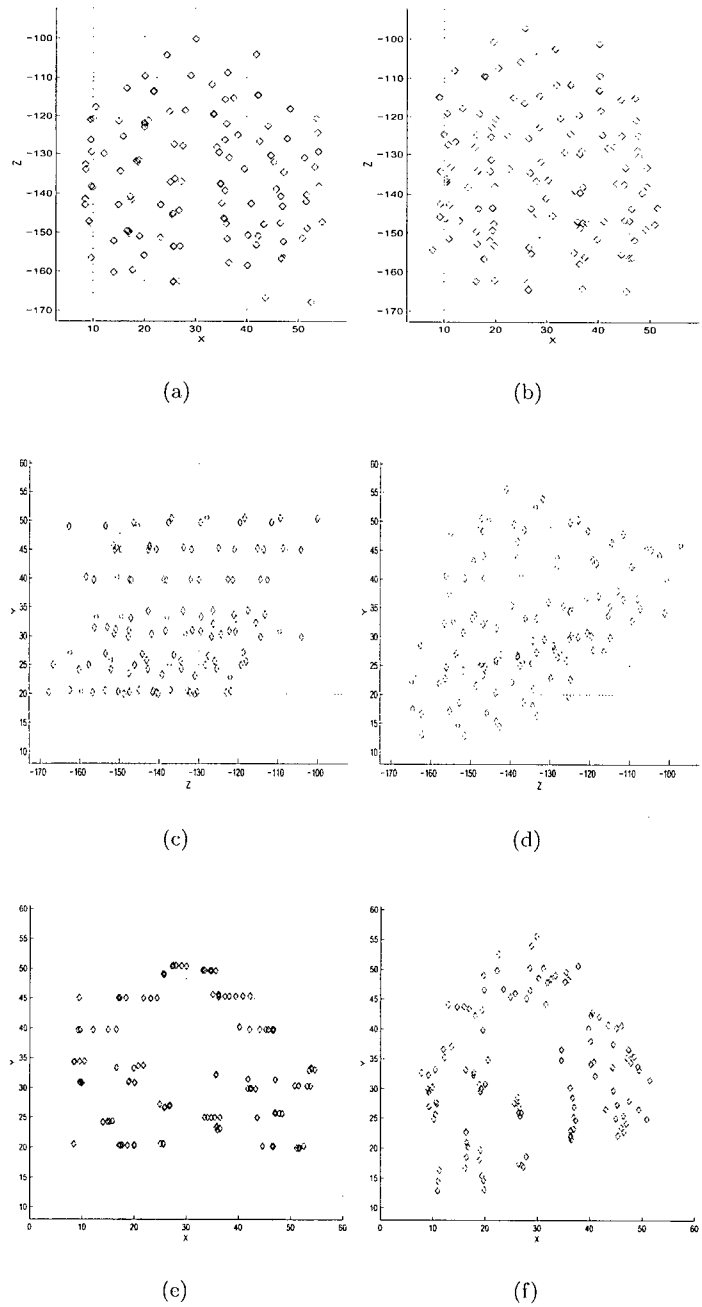

Figure B.14: A top view of (a) the RTD and (b) the CT seed distributions, (c) and (d) are a side view of the RTD and CT seed distributions, respectively, and (e) and (f) are a front view of the RTD and CT seed distributions, respectively.

B.8 Case H

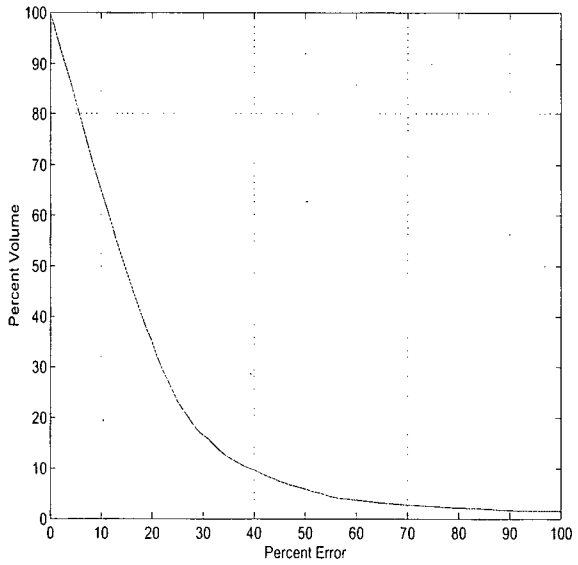

Figure B.15: A plot of percent error in dosimetry (see Equation 6.1) versus percent volume.

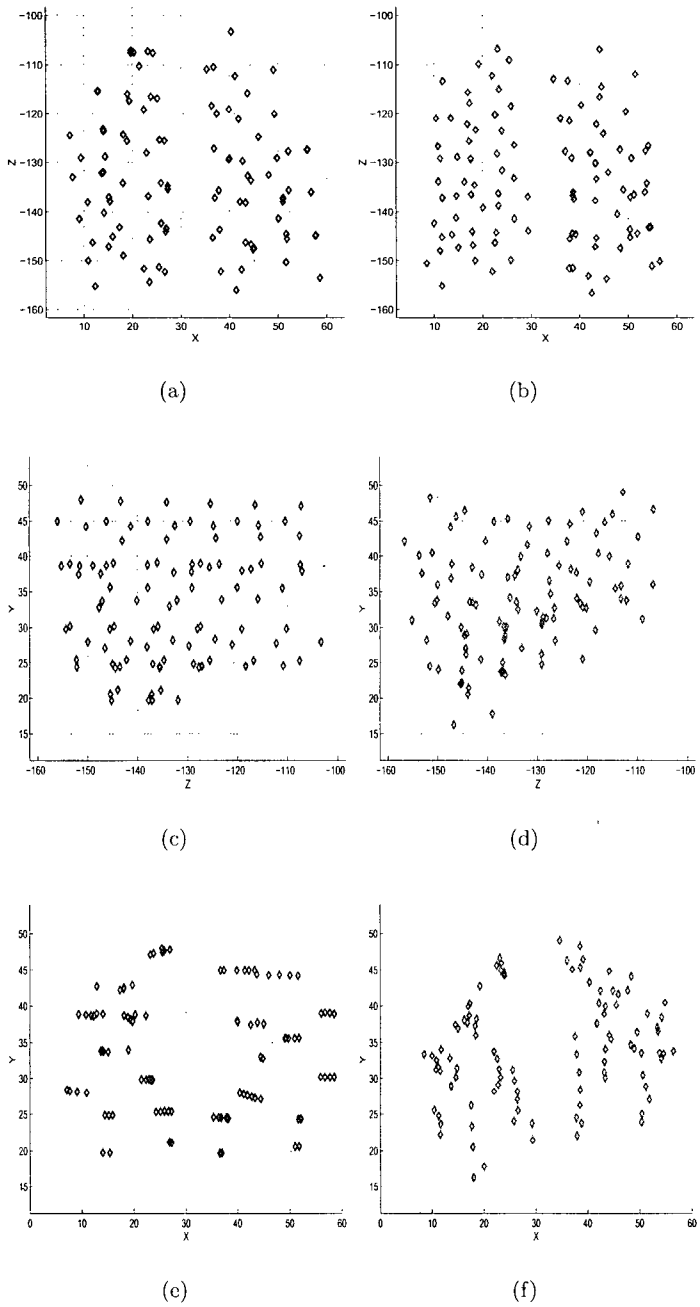

Figure B.16: A top view of (a) the RTD and (b) the CT seed distributions, (c) and (d) are a side view of the RTD and CT seed distributions, respectively, and (e) and (f) are a front view of the RTD and CT seed distributions, respectively.